2014-03-12

Facile Synthesis and Characterization of a Thermally Stable Silica-Doped Alumina with Tunable Surface Area, Porosity, and Acidity

Maryam Khosravi Mardkhe
Brigham Young University - Provo

BYU ScholarsArchive Citation
Khosravi Mardkhe, Maryam, "Facile Synthesis and Characterization of a Thermally Stable Silica-Doped Alumina with Tunable Surface Area, Porosity, and Acidity" (2014). *Theses and Dissertations*. 3968.
https://scholarsarchive.byu.edu/etd/3968

Facile Synthesis and Characterization of a Thermally Stable Silica-Doped Alumina with Tunable Surface Area, Porosity, and Acidity

Maryam Khosravi Mardkhe

A dissertation submitted to the faculty of
Brigham Young University
in partial fulfillment of the requirements for the degree of

Doctor of Philosophy

Brian F. Woodfield, Chair
Calvin H. Bartholomew
Roger G. Harrison
Adam T. Woolley
Julie Boerio-Goates

Department of Chemistry and Biochemistry

Brigham Young University

March 2014

ABSTRACT

Facile Synthesis and Characterization of a Thermally Stable Silica-Doped Alumina with Tunable Surface Area, Porosity, and Acidity

Maryam Khosravi Mardkhe
Department of Chemistry and Biochemistry, BYU
Doctor of Philosophy

Mesoporous γ-Al_2O_3 is one of the most widely used catalyst supports for commercial catalytic applications. The performance of a catalyst strongly depends on the combination of textural, chemical and physical properties of the support. Pore size is essential since each catalytic system requires a unique pore size for optimal catalyst loading, diffusion and selectivity. In addition, high surface area and large pore volume usually result in higher catalyst loading, which increases the number of catalytic reaction sites and decreases reaction time. Therefore, determination of surface area and porosity of porous supports is critical for the successful design and optimization of a catalyst support. Moreover, it is important to produce supports with good thermal stability since pore collapsing due to sintering at high temperatures often results in catalyst deactivation. In addition, the ability to control the acidity of the catalyst enables us to design desirable acid sites to optimize product selectivity, activity, and stability in different catalytic applications.

This dissertation presents a simple, one-pot, solvent-deficient method to synthesize thermally stable silica-doped alumina (SDA) without using templates. The XRD (X-ray diffraction), HTXRD (high temperature X-ray diffraction), SS NMR (solid state nuclear magnetic resonance), TEM (transmission electron microscopy), TGA (thermogravimetric analysis), and N_2 adosorption techniques are used to characterize the structures of the synthesized SDAs and understand the origin of increased thermal stability. The obtained SDAs have a surface area of 160 m^2/g, pore volume of 0.99 cm^3/g, and a bimodal pore size distribution of 23 and 52 nm after calcination at 1100°C. Compared to a commercial SDA, the surface area, pore volume, and pore diameter of synthesized SDAs are higher by 46%, 155%, and 94%, respectively. A split-plot fractional-factorial experimental design is also used to obtain a useful mathematical model for the control of textural properties of SDAs with a reduced cost and number of experiments. The proposed quantitative models can predict optimal conditions to produce SDAs with high surface areas greater than 250 m^2/g, large pore volume greater than 1 cm^3/g, and large (40-60 nm) or medium (16-19 nm) pore diameters.

In my approach, I control acid sites formation by altering preparation variables in the synthesis method such as Si/Al ratio and calcination temperatures. The total acidity concentration (Brønsted and Lewis) of the synthesized SDAs are determined using ammonia temperatured program, pyridine fourier transform infrared spectroscopy (FTIR), and MAS NMR. The total acidity concentration is increased by introducing a higher mole ratio of Si to Al. In addition, the total acidity concentration is decreased by increasing calcination temperature while maintaining high surface area, large porosity, and thermal stability of γ-alumina support.

I also present an optimized synthesis of various aluminum alkoxides (aluminum *n*-hexyloxide (AH), aluminum phenoxide (APh) and aluminum isopropoxide (AIP)) with high yields (90-95%). One mole of aluminum is reacted with excess alcohol in the presence of 0.1 mole % mercuric chloride catalyst. The synthesized aluminum alkoxides are used as starting materials to produce high surface area alumina catalyst supports. Aluminum alkoxides and nano aluminas are analyzed by ^{1}H NMR, ^{13}C NMR, ^{27}Al NMR, gCOSY (2D nuclear magnetic resonance spectroscopy), IR (infrared spectroscopy), XRD, ICP (induced coupled plasma), and elemental analysis.

Keywords: Mesoporous metal oxide, Synthesis, Solvent-deficient method, Aluminum alkoxides, Silica-doped γ-Al_2O_3, Thermal stability, Acidity, Surface area, Pore volume, Pore diameter.

ACKNOWLEDGMENTS

First of all, I would like to express my highest appreciation to my advisor Professor Brian Woodfield. I came to BYU fresh and ambitious but knowing not much about what awaited me in this totally new environment. Professor Brian Woodfield has been always there for me kindly and supportively. I appreciate his guiding and directing while giving me the freedom and the support to try new things and become an independent researcher.

I would like thank Professor Calvin Bartholomew. His guidance, support, and encouragement played a vital role in completion of this research. Thank you for the hours you have devoted to teach me how to be a better scientist and writer.

I wish to acknowledge all the professors in the Chemistry and Biochemistry Department for their valuable teaching and guidance, especially those members of my doctoral committee for their input, valuable discussions and accessibility. In particular, I would like to thank Dr. Roger Harrison, Dr. Adam Woolley, Dr. Boerio-Goates, Dr. Macedone, and Dr. Farnsworth. My special thanks to Dr. Andrus and Dr. Burt for training and helping me in NMR experimental studies throughout my research. Thanks to Dr. John Lawson for helping me design the synthetic experiments for my project. Thanks to Mr. Adam Todd for the MAS-NMR work; which had a great contribution in my research.

I would like to give special thanks to people I consider as mentors and friends along my journey to this point: Baiyu, Betsy, Stacey, Cameron, Erika, Jessie, Ying, Kamyar, and Jacob. Thank you all for the good times that we shared together.

I would like to thank my friends in Utah, for their friendship and encouragements that made my staying at BYU a wonderful experience.

I would like to thank my family for their countless love and support; my brother (Mani) for a good example of hard worker and a great supporter, my mother (Tahereh) for helping me develop my talents and gain confidence, my dear father (Hadi) for inspiring me to be innovative and a deep thinker. I cannot share my happiness with you now, but I owe you the deepest appreciations.

Finally, I wish to single out the one person who contributed more encouragement, patience, love, and confidence in me, than any other person. That special person is my husband, Ali. Thank you for always being there for me.

Table of Contents

List of Tables xii

List of Figures xiv

1 Introduction 1

1.1 Metal alkoxides . . . 3

1.1.1 Metal alkoxides chemistry . . . 3

1.1.2 Preparation of metal alkoxides . . . 3

1.1.3 Aluminum alkoxide structures . . . 6

1.1.4 Metal alkoxide sol-gel process . . . 7

1.2 Aluminum oxide (Alumina) . . . 9

1.2.1 Forms of alumina . . . 10

1.2.2 Current synthesis of alumina . . . 15

1.2.3 Current synthesis of thermally stable doped-alumina . . . 19

1.3 Overview of dissertation . . . 21

Bibliography 22

2 Characterization Techniques 39

2.1 Introduction 39

2.2 BET and Pore properties 39

  2.2.1 Gas adsorption 39

  2.2.2 Adsorption isotherms 41

  2.2.3 Surface area 44

  2.2.4 Kelvin Equation and pore size 45

2.3 Nuclear magnetic resonance 48

  2.3.1 Nuclear magnetic resonance applications 48

  2.3.2 Nuclei and magnetic field 48

  2.3.3 NMR theory 49

  2.3.4 Solution and solid samples 51

2.4 Transmission electron microscopy 53

  2.4.1 Transmission electron microscopy applications 53

  2.4.2 TEM system 54

  2.4.3 TEM contrast information 55

2.5 X-ray diffraction 57

  2.5.1 X-ray diffraction applications 57

  2.5.2 Bragg equation 60

  2.5.3 Reciprocal lattice and Ewald sphere 61

  2.5.4 Diffraction pattern 63

Bibliography **67**

3 The origin of increased thermal stability for silica-Doped alumina **70**

3.1 Introduction 70

3.2 Experimetnal 73

3.2.1 Material 73

3.2.2 Synthesis method 73

3.2.3 Characterization 74

3.3 Results 75

3.3.1 X-ray diffraction 75

3.3.2 Nitrogen adsorption 77

3.3.3 TEM images 78

3.3.4 TGA and DSC 79

3.3.5 Solid state NMR measurements 79

3.4 Discussion 82

3.4.1 Silica-alumina structure 82

3.4.2 Comparison to other silica-doped alumina 86

3.5 Conclusions 88

Bibliography **91**

4 A statistical approach to control porosity and surface area in thermally stable silica-doped alumina support **99**

4.1 Introduction 99

4.2 Experimental 102

4.2.1 Material 102

4.2.2 Synthesis method 102

4.2.3 Statistical analysis 102

4.2.4 Characterization 103

4.2.5 Synthesis results 105

4.2.6 Statistical model 105

4.2.7 Influence of factors on surface area 107

4.2.8 Influence of factors on pore diameter 108

4.2.9 Influence of factors on pore volume 110

4.3 Discussion 113

4.3.1 Confirmation of model predictions 113

4.3.2 The effect of excess alcohol 115

4.3.3 The effect of excess alcohol and calcination ramp rate 117

4.3.4 The effect of drying 117

4.4 Conclusions 118

Bibliography **119**

5 Acid site properties of thermally stable, silica-doped alumina as a function of silica alumina ratio and calcination temperature **126**

5.1 Introduction 126

5.2 Experimental 129
  5.2.1 Material 129
  5.2.2 Synthesis method 129
5.3 Characterization 131
  5.3.1 Silica-doped aluminas 131
  5.3.2 Acidity measurements 131
5.4 Results 133
  5.4.1 Silica-doped alumina physical properties 133
  5.4.2 Acid site properties 133
5.5 Discussion 135
  5.5.1 Relationship between acid site concentrations and silica content 137
  5.5.2 Relationship between acid site concentrations and calcination temperature 140
5.6 Conclusions 142

Bibliography **143**

6 Generalized preparation method and characterization of aluminum isopropoxide, aluminum phenoxide, and aluminum *n*-hexyloxide 150

6.1 Introduction 150
6.2 Experimental 153
  6.2.1 Materials 153
  6.2.2 Equipment 153

6.3 Synthesis . . . 154

  6.3.1 General procedure . . . 154

  6.3.2 Synthesis of aluminum *n*-hexyloxide (AH) . . . 155

  6.3.3 Synthesis of aluminum phenoxide (APh) . . . 156

  6.3.4 Synthesis of aluminum isopropoxide (AIP) . . . 156

  6.3.5 Synthesis of nanosized alumina . . . 157

6.4 Results and Discussion . . . 157

  6.4.1 FTIR . . . 157

  6.4.2 NMR . . . 159

  6.4.3 XRD . . . 163

  6.4.4 BET . . . 167

  6.4.5 ICP . . . 168

  6.4.6 Elemental analysis . . . 168

6.5 Conclusions . . . 169

Bibliography **171**

List of Tables

1.1 Applications of aluminas in catalysis industry adopted from [12]. 1

2.1 Available data from full range isotherm [1]. 41

3.1 BET results of 0-5-15-27% SDAs calcined at different temperatures for 2h. 78

3.2 Surface area, pore diameter, and mesopore volume for doped aluminas with different methods at different temperatures (°C). S1= [17], S2= [20], S3= [15], S4= [16], and S5= [54]. 88

3.3 BET results of 5% SDA and Siral-5 calcined at different temperatures for 24 h. 89

4.1 Experiments to make SDAs. 104

4.2 Trials to confirm the models and predictions. 114

5.1 BET results of 0-5-15-27% SDAs calcined at different temperatures for 2h. 129

5.2 The Brϕnsted and Lewis acid site concentrations reported in this work and in previous studies. S1 = [33], S2 = [9], S3 = [34], S4 = [11], and S5 = [17]. 134

6.1 Synthesis conditions to produce APh, AH, and AIP. 155

6.2 BET properties of aluminas sythesized from different Aluminum alkoxides. 167

6.3 Mercury impurity in synthesized aluminum alkoxides. 169

6.4 Elemental analysis of synthesized and commercial aluminum isopropoxide. 169

List of Figures

1.1 Aluminum coordination numbers (a) 4-coordinated aluminum, (b) 5-coordinated aluminum, (c) 6-coordinated aluminum. 7

1.2 Condensation process. 10

1.3 Decomposition sequences of alumina hydroxides. 11

1.4 The first two layers in the gamma alumina structure. Octahedral Al ions are black, tetrahedral are grey. 13

1.5 The first layer in the alpha alumina structure. Octahedral Al ions are black. 13

1.6 The first two layers (A and B) in the kappa alumina structure. Octahedral Al ions are black, tetrahedral are grey. 15

1.7 Structure of theta-alumina in which half of the Al ions occupy tetrahedral sites. Al ions are black, O ions are grey. 16

1.8 Structure of plate-like alumina precursor (bohemite) [103]. 19

2.1 Four stages of gas adsorption on the solid surface in BET analyzer. . 40

2.2 The six types of adsorption isotherms [2]. 43

2.3 Different types of hysteresis [2]. 43

2.4 Spin orientation in the presence of magnetic field [14]. 49

2.5 Precession of a spinning nucleus in a magnetic field. 50

2.6 Adsorbing RF radiation causes the nucleus to spin flip [14]. 50

2.7 Nuclear spin energy levels [14] 52

2.8 Magic angle spinning. 53

2.9 Diagram of a transmission electron microscope [17]. 55

2.10 Ray diagrams of TEM imaging for the (a) bright field, (b) dark field, (c) selected area electron diffraction modes adapted from Reimer [17], (d) bright field, (e) dark field, and (f) diffraction images of Pt/La$-$Al$_2$O$_3$ nanoparticles [18]. 58

2.11 The energy of an inelastically scattered electron is always less than that of the primary electron [17]. 59

2.12 The low-loss peaks of the Al atoms in different environments. The differences in the spectra are due to differences in bonding [13]. . . . 59

2.13 (a) Face centered cubic structure, (b) X-ray diffractions 60

2.14 X-rays scattered by atoms in an ordered lattice interfere constructively in directions given by Bragg's law [19]. 61

2.15 (a) Representation of unit cell planes as d_{hkl} vectors, (b) The reciprocal lattice [19] 62

2.16 Ewald sphere [19]. 63

2.17 Examples for the Ewald construction for the X-ray diffraction scan. . 64

2.18 The intersection of d^*_{hkl} vectors from a sample powder with Ewald sphere [19]. 65

2.19 Powder XRD of 24 nm NiO: (a) Powder XRD ring pattern, (b) Integrated slice of the ring, (c) Powder 2D pattern [20]. 66

3.1 Synthesis of silica-dopped alumina. 73

3.2 XRD patterns of different aluminas calcined at different temperatures for 2 h. (a) Pure alumina, (b) 5% SDA, (c) 15% SDA, (d) 27% SDA. Standards: 1) Gamma alumina. 2) Alpha alumina. 3) Theta alumina. 4) Mullite. 76

3.3 In situ high-temperature XRD patterns of 5% SDA 700-1200°C. . . . 77

3.4 TEM micrographs of aluminas calcined at different temperatures: (a) 5% SDA calcined at 700°C, (b) Pure alumina calcined at 700°C, (c) 5% SDA calcined at 1100°C. 80

3.5 Thermal analysis data for: (a) 5% SDA, (b) pure alumina, (c) 15% SDA d) 27% SDA. 81

3.6 The 1D ^{27}Al MAS NMR spectra for 5 and 27% SDAs and alumina calcined at 700 and 1200°C for 2 h. 83

3.7 Direct ^{29}Si MAS NMR and ^{29}Si-^{1}H CPMAS spectra for (a) 5% SDA, and (b) 27% SDA calcined at 700°C for 2 h. 84

3.8 XRD patterns of (a) Siral-5 calcined at different temperatures for 24 h, (b) 5% SDA calcined at different temperatures for 24 h. 89

4.1 XRD of SDAs calcined at 1200°C for 2 h. 106

4.2 Interaction of excess alcohol, drying method and mixing method on surface area. 109

4.3 Interaction of excess alcohol and calcination ramp on surface area. . . 110

4.4 Interaction between excess alcohol, mixing time, mixing seal and mixing method on pore diameter. 111

4.5 Average effect of drying method on pore volume. 112

4.6 Average effect of mixing method on pore volume. 113

4.7 TEM micrographs of SDA synthesized from L2 batch with no drying condition 116

5.1 XRD patterns of different aluminas calcined at different temperatures for 2 h. (a) Pure alumina, (b) 5% SDA, (c) 15% SDA, (d) 27% SDA. Standards: 1) Gamma alumina. 2) Alpha alumina. 3) Theta alumina. 4) Mullite. 130

5.2 Ammonia-TPD measurements of different SDAs calcined at different temperatures for 2 h. a) 5% SDA. b) 15% SDA. c) 27% SDA. 136

5.3 The 1D ^{27}Al MAS NMR spectra and relative compositions of 5-15-27% SDAs calcined at 700-1200C. 138

5.4 (a) IR transmittance spectra recorded after pyridine adsorption on 5-15-27% SDAs calcined at 700°C, (b) Absorption spectra after pyridine adsorption of 5, 15, 27% SDAs calcined at 700°C and 1200°C (in the range: 1432-1467 cm^{-1} (Brϕnsted sites) and 1516-1568 cm^{-1} (Lewis sites)). 139

6.1 IR spectra of (a) aluminum *n*-hexyloxide and 1-hexanol, (b) aluminum phenoxide and phenol, and (c) aluminum isopropoxide and 2-propanol. 158

6.2 (a)^{1}H NMR of aluminum *n*-hexyloxide, and (b) ^{1}H NMR of aluminum *n*-hexyloxide and 1-hexanol comparison. 160

6.3 gCOSY of aluminum *n*-hexyloxide. 161

6.4 ^{13}C NMR of aluminum n-hexyloxide. 162

6.5 ^{1}H NMR of aluminum phenoxide. 163

6.6 ^{13}C NMR of aluminum phenoxide. 164

6.7 ^{1}H NMR of freshly distilled aluminum isopropoxide. 164

6.8 ^{1}H NMR of aged aluminum isopropoxide 165

6.9 ^{27}Al NMR of aluminum phenoxide, freshly prepared aluminum isopropoxide and aluminum *n*-hexyloxide. 165

6.10 ^{27}Al NMR of aged aluminum isopropoxide. 166

6.11 (a) 4-coordinated aluminum, (b) 5-coordinated aluminum, (c) 6-coordinated aluminum. 166

6.12 X-ray diffraction patterns of (a) APh, AH, and AIP calcined at 550°C, (b) APh, AH, and AIP calcined at 1000°C. 167

Chapter 1

Introduction

The aluminum oxides (aluminas) have various applications such as ceramic membranes [1–3], paints and cosmetics [4, 5], refinery catalysis, pollution control, chemical catalysis, and catalyst supports (see Table 1.1) [6–12].

Table 1.1: Applications of aluminas in catalysis industry adopted from [12].

Application	**Alumina Role**	**Example**
Alkylation	Catalyst	Phenol
Dehydration	Catalyst	Formic acid
Dehydrogenation	Support	Hydrocarbon
Isomerization	Catalyst	1-methlcyclohexane
Isomerization	Support	Isophthalonitrile
Hydrogenation	Catalyst	Ethylene
Hydrogenation	Support	Benzene
Hydrodesulfurization	Support	Petroleum refining
Hydrodenitrogenation	Support	Petroleum refining
Cracking	Catalyst	Hydrocarbons
Cracking	Support	Naphtha
Clause catalyst	Catalyst	Sulfur
Auto exhaust	Support	Platinum

Mesoporous $\gamma-$alumina (MA) with pore diameters between 2 and 50 nm is a common catalyst support in heterogeneous reactions due to its high surface area, large porosity, high thermal stability, and narrow pore size distribution. The main advantages of mesoporous alumias are as follows:

1. Higher surface area leads to increased density of active sites in MA and higher loadings of metals, metal oxides, and metal sulfides while maintaining a high dispersion of the active phase.
2. MA contain a relatively high density of basic sites (in addition to Lewis and Brϕnsted sites) compared to conventional non-porous aluminas. Basic sites increasing the interaction between metal oxides and alumina supports, thereby enhance catalytic activity of oxide catalysts.
3. Surface area and pore properties of MA are tunable.
4. MA are thermally stable.

The pore size, surface area, thermal stability, and acid sites can be optimized by varying the preparation conditions [12–16]. Therefore, the synthesis and characterization of MA are required to determine their structures and properties, which leads to finding their appropriate applications in various industries.

This study focuses on the development of a facile solvent-deficient method to synthesize thermally stable MA catalyst supports with different pore properties and acid sites. In addition, I introduce a generalized method to synthesize different aluminum alkoxides that are used as starting materials to produce MA. In this chapter, I provide an overview of aluminum alkoxides and MA (alumina), including their structures, properties and synthesis.

1.1 Metal alkoxides

1.1.1 Metal alkoxides chemistry

The term alkoxide was first proposed by Kuhlman [17] for alkaline derivates of alcohols. Later Tishchenko [18] made a proposal to synthesize aluminum alkoxides and use them for the ester condensation of aldehydes. Synthetic and physiochemical properties of metal alkoxides were developed by Gilman [19, 20] and Bradley [21]. Bradely reported the synthetic method to prepare a variety of metal alkoxides and determine the structure of oligomeric alkoxides using X-ray structure studies. He reported that metal atoms achieve the highest coordination number with the lowest molecular complexity. The metal alkoxides demand further development since they are suitable precursors for synthesis of a variety of materials.

The physical properties of metal alkoxides ($\mathrm{M(OR)_n}$, where M: metal and R: alkyl group) vary with the electronegativity and coordination number of the metal, as well as the steric effect of the attached alkyl group [12], where the identity of the parent alcohol influences the electronic and steric properties of the alkoxide [13].

1.1.2 Preparation of metal alkoxides

Metal alkoxides are used as precursors to synthesize various nano metal oxides. The majority of metal alkoxides ($\mathrm{M(OR)_n}$) with $n \leq 3$ can be easily purified through distillation, sublimation (below 200°C), or recrystallization. As a result high purity metal oxides can be produced using metal alkoxides. Unlike metal nitrates and chlorides, metal alkoxides are easily purified; they hydrolyze to produce oxides with no anionic contamination [22, 23]. Moreover, metal alkoxides form mesoporous oxide particles with high surface area and porosity. In the following, I discuss the different methods to produce various metal alkoxides.

1.1.2.1 Reaction of metals with alcohols

This method is performed for the most active metals. This reaction of metals with alcohols is accelerated by catalysts such as I_2, Br_2, $HgCl_2$, or Hg which enhance the dissolution of metals in alcohols [22]. Aluminum alkoxides can be produced without using a catalyst, but the reaction rates are very slow [24]. Therefore, aluminum alkoxides are more efficiently produced using three equivalents of anhydrous alcohol with one equivalent of metal in the presence of one mole % $HgCl_2$ as catalyst [25] as shown in Eq. 1.1.

$$\mathrm{Al} + 3\mathrm{ROH} \xrightarrow{0.01\mathrm{HgCl_2}} \mathrm{Al(OR)_3} + \tfrac{3}{2}\mathrm{H_2} \tag{1.1}$$

This reaction has been widely used to make simple alkoxides, including aluminum isopropoxide and aluminum ethoxide. In these cases, this route has become a well-known industrial process [22, 24–27]. Tomar and Yoo [28] recently reported approaches to aluminum phenoxide and aluminum isopropoxide through this process as well.

1.1.2.2 Anodic oxidation of metals

This method is used in the synthesis of the derivates of less active metals. Such as electrochemical synthesis of Si, Ti, Zr, and Ge alkoxides by anodic dissolution in alcohols. However, the dissolution of less active metals is often incomplete and precipitation of metal or metal oxides is observed.

1.1.2.3 Reaction of metals oxides or hydroxides with alcohols

This method is important for synthesis of thallium alkoxides and metal phenolates [22]. Since water is produced in this method and reactions are reversible (see Eqs. 1.2 and 1.3), alcohols with the boiling temperature higher than 100°C are used.

$$\mathrm{MOH + ROH \rightleftharpoons MOR + H_2O} \tag{1.2}$$

$$\mathrm{MO + 2ROH \rightleftharpoons M(OR)_2 + H_2O} \tag{1.3}$$

1.1.2.4 Reaction of alcohols and MX_n

This method involves interaction of hydrogen between alcohol and the anions of metals (X) that produce a strong covalent bond with HX (see Eq. 1.4, in which X can be H, alkyl, NH_2, NR_2, SH,...). $Cr(OBu)_4$, $V(OR)_4$, $Sn(OR)_4$, and $Nb(OBu)_5$ were synthesized using this method [29]. The problem with the application of this method is the availability of metal amides and alkyls. In addition, an amide group is a strong σ-donor and π-donor, which stabilizes a higher oxidation state metal that makes it inert to alcoholysis by ROH [30].

$$\mathrm{MX_n + nROH \longrightarrow M(OR)_n + nHX(g)} \tag{1.4}$$

1.1.2.5 Metathesis reactions of metal halides with alkaline alkoxides

Ge, Ti, In, La, Ln, Bi, V, Nb, W, and Fe alkoxides have been synthesized through this route (see Eq. 1.5) [31–33]. However, this process is complicated by the formation of bimetalic complexes such as $NaM(OR)_n$.

$$\mathrm{MX_n + nNaOR \longrightarrow M(OR)_n + nNaX} \tag{1.5}$$

1.1.2.6 Reaction of alcohol interchange or transesterification

Alcohol interchange method (Eq. 1.6) is used for synthesis of all methoxides (MeOH has the minimum boiling temperature) and unstable alcohols which undergo decomposition using other methods. The transesterification method (Eq. 1.7) results in complete substitution of OR, due to the stronger coordination of the carbonyl oxygen compared to the alkoxide oxygen [29].

$$\mathrm{M(OR)_n + nR^{'}OH \longrightarrow M(OR^{'})_n + nROH} \tag{1.6}$$

$$\mathrm{M(OR)_n + nR^{''}COOR^{'} \longrightarrow M(OR^{'})_n + nR^{''}COOR} \tag{1.7}$$

Many studies have been done towards preparation of alumina (aluminum oxide) with desired properties, e.g. particle size, surface area, pore volume, and pore diameter, using different aluminum alkoxides, such as aluminum isopropoxide [23, 34–38], aluminum sec-butoxide [37, 39–41], aluminum ethoxide [37], and aluminum phenoxide [42]. The properties of alumina, particularly the surface area and pore size, depend on a number of factors, including the nature of the aluminum alkoxide starting material. Since the identity of the parent alkoxide influences the properties of the alumina, it is important to develop an efficient method to synthesize different aluminum alkoxides. In Chapter 6, the process to make different pure aluminum alkoxides and nanosized aluminum oxides is discussed.

1.1.3 Aluminum alkoxide structures

Aluminum alkoxides exist as monomers, dimers, trimers and tetramers with various coordination numbers. The oligomerization is inversely depends on the steric demand of the R group attached to the oxygen [42]. The $\mathrm{Al^{+3}}$ can form

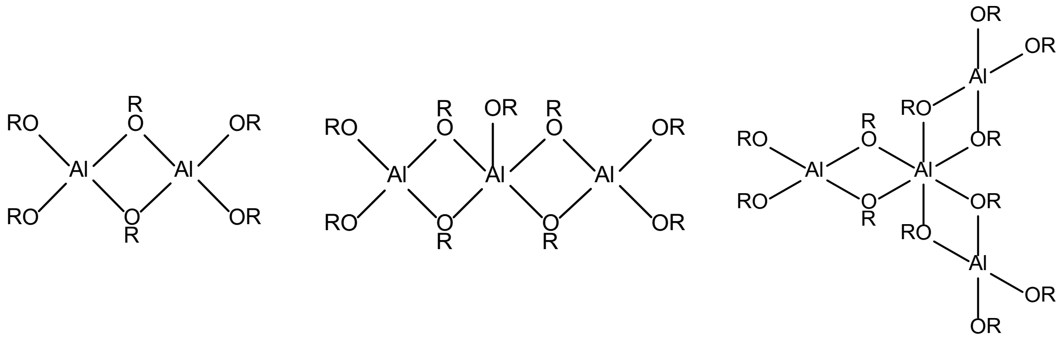

(a) (b) (c)

Figure 1.1: Aluminum coordination numbers (a) 4-coordinated aluminum, (b) 5-coordinated aluminum, (c) 6-coordinated aluminum.

four-coordinated, five-coordinated, and six-coordinated complexes. The structure of aluminum ethoxide is polymeric, containing five-coordinated aluminum [43]. Aluminum tert-butoxide is dimeric containing aluminum with a coordination number of four [43]. Aluminum isopropoxide exists as a trimer in freshly prepared samples or as a tetramer in aged samples [43, 44]. The coordination numbers of aged aluminum isopropoxide can be six and four [45]. Aluminum phenoxide has been reported to be a trimer containing aluminum with coordination numbers of four and five [46]. Different coordination numbers of aluminum are also reported in di-aluminum alkoxide, tri-aluminum alkoxide, tetra-aluminum alkoxide, and polynuclear aluminum alkoxide [42, 47–50].

1.1.4 Metal alkoxide sol-gel process

Two major developments in sol-gel processing have been done by Ebelmen [51] and Grimaux [52]. The former prepared silicon alkoxides by reaction between alcohol and silicon tetrachloride and the latter hydrolyzed tetramethoxy-silane to prepare silicic acid sols and make iron oxide from iron alkoxide. Later, Patrick [53] dried and thermally treated the homogenous silica gel up to 700°C to produce porous silica [54]. By 1930, he produced several supported catalysts using the sol gel method [55–57], which was the beginning of a development to produce variable catalyst supports using the sol-gel method. Yoldas [58, 59] investigated preparation and properties of alumina from aluminum alkoxides using the sol-gel method.

Sol gel preparation involves producing colloidal suspension (sols), which are converted to viscous gels and consequently solid materials. The sol-gel method is favored over other available methods due to the advantages below:

1. Highly porous materials and nano-crystalline materials can be prepared in this way.
2. The low temperature of the sol gel processes is generally below the crystallization temperature for oxide materials which allows the production of amorphous materials.
3. Particle size, pore size, and porosity of the sol-gel product can be adjusted by appropriate chemical modification of the precursors and control over the rate of hydrolysis and condensation. In addition, by controlling aging and drying conditions, a desirable pore size can be achieved.
4. The chemical condition is mild and no extreme pH condition is needed. In this way pH sensitive species retain their function.
5. Templates can be used in sol-gel process to create pores with controlled size and shape. They can be removed by acid treatment or heat treatment.

6. Precursors such as metal alkoxides are volatile and easily purified by distillation or sublimation which contributes to high purity product.

The alkoxide sol gel process occurs in a series of steps as follows: in the hydrolysis step, alkoxide and water produce nROH and $M(OR)_{3\text{-}n}(OH)_n$ (n=number of water, R=alkyl group, M=metal). In the condensation step, two $M(OR)_{3\text{-}n}(OH)_n$ react and produce M-O-M bonds and either water or alcohol. The condensation can occur in two possible ways: alkoxolation with alcohol elimination (Fig. 1.2a) and oxolation with elimination of a water molecule (Fig. 1.2b). In the gelation step, a network entraps the solution with high viscosity. In the aging step, cross-links associated with shrinkage of gel are formed. In this step, covalent links replace non-bonded contacts. In the drying step, water, alcohol, and other volatile components are evaporated. In the densification step, thermal treatment leads to collapse of the structure and formation of a metal oxide.

1.2 Aluminum oxide (Alumina)

As mentioned in Section 1.1, aluminum alkoxides are used to make Al_2O_3 (alumina) catalyst supports for a wide range of applications, including hydrocracking, hydrodesulfurization and Fischer-Tropsch catalysis (FT) [14, 28, 37, 60–62].

Hydrolysis of aluminum alkoxides results in a precipitate of AlO(OH) (boehmite) in neutral solution. Subsequently, thermal treatment of AlO(OH) leads to crystalline phase transitions and loss of hydroxide groups and protons. Thermal treatment of AlO(OH) results in transformation of AlO(OH) into different crystalline structures of aluminas. The sequence of phase transformations (forms of alumina) at different temperatures can be summarized in Fig. 1.3 [63]. In addition to the phase transition, the other properties such as particle size, surface area, pore size distribution,

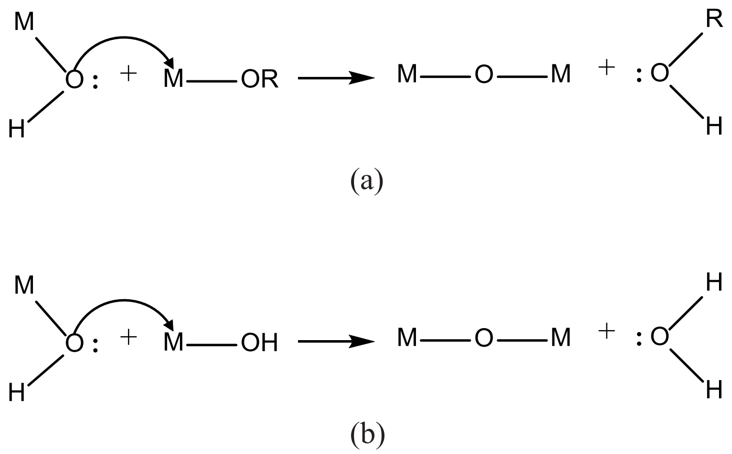

Figure 1.2: Condensation process.

and pore volume are changed. These properties could influence alumina behavior in catalyst reactions.

1.2.1 Forms of alumina

Alumina structures can be divided into two categories based on the arrangement of oxygen anions (face-centered cubic (*fcc*), and hexagonal close-pack (*hcp*)). Each category includes different polymorphs based on the distribution of cations. The γ, θ, δ and η aluminas have *fcc* structures. The κ, α and χ aluminas have *hcp* structures. The stable alpha Al_2O_3 phase ($\alpha-Al_2O_3$ or corundum) can be used as

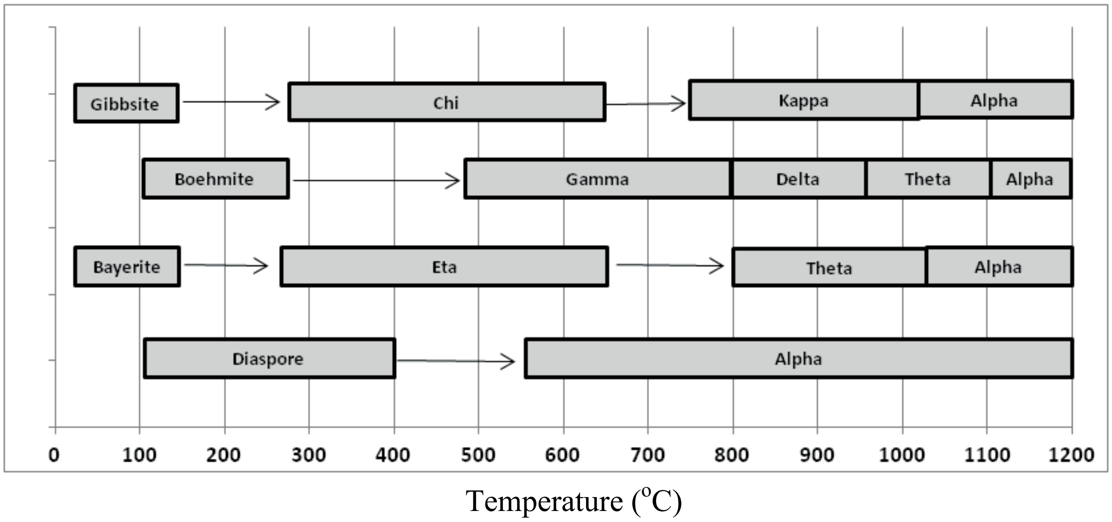

Figure 1.3: Decomposition sequences of alumina hydroxides.

a refractory material, abrasive material, and color pigment. The metastable transitional Al_2O_3 phases (chi (χ), eta (η), kappa (κ), gamma (γ), delta (δ), and theta (θ)) are porous and can be used as adsorbents, desiccants, and catalyst supports.

1.2.1.1 Gamma alumina (γ)

The $\gamma-Al_2O_3$ is poorly ordered and controversy still exists over its definitive structure. The $\gamma-Al_2O_3$ was thought to have a cubic spinel structure until the tetragonally-disordered spinel structure was reported [64,65]. Lippens et al. [64] found that distortion of spinel lattice decreases with increasing the time or temperature of heat treatment. In this case, the amount of tetragonal $\gamma-Al_2O_3$ reduces during the formation of cubic $\gamma-Al_2O_3$. The commonly accepted structure of $\gamma-Al_2O_3$ is a defect spinel structure [13] with the oxide anions arranged in a cubic close-packed lattice and the cations occupying some or all of the octahedral and tetrahedral sites in the lattice (Fig. 1.4). Based on neutron diffraction, X-ray diffraction, and electron microscopy, the atom vacancies are found in octahedral sites [66], tetrahedral [67] sites, or distributed over both spinel site positions [65, 68, 69]. Also, several computational and NMR studies have shown that atom vacancies are distributed on octahedral [70, 71] and tetrahedral [72] sites. Smith et al. [73] employed a combination of X-ray pair-distribution function (PDF) and solid state NMR to characterize $\gamma-Al_2O_3$ structure. They reported that $\gamma-Al_2O_3$ has boehmite-like stacking-fault defects that steadily disappear during calcination.

The $\gamma-Al_2O_3$ is the most widely used commercial catalyst support due to its moderately high surface area, meso- and macro-porosity, and relatively high thermal and hydrothermal stabilities. It is an effective catalyst support for both base and noble metals in many different applications (e.g., Pt, Pd catalytic converters [8], Ni catalyst in hydrogenation [74], Co(Ni)-Mo(W) sulfide catalysts for hydrotreating of petroleum feedstocks [7], and Co catalyst for Fischer-Tropsch synthesis (FTS) [6,11]). In these applications, the commercial aluminas require a unique range of surface area, pore volume and pore diameter [75–77]. Thus, ability to optimize $\gamma-Al_2O_3$ pore size and pore volume is essential in the manufacture of these materials [11, 14, 78, 79]. $\gamma-Al_2O_3$ can also be used as an active catalytic phase in applications that require Brϕnsted and/or Lewis acid sites, e.g. alkylation, isomerization, polymerization, hydrogenation and Claus reaction.

1.2.1.2 Alpha alumina (α)

The $\alpha-Al_2O_3$ is the only stable alumina phase at high temperatures, e.g. 1400°C. It has lower surface area and porosity than metastable aluminas such as $\gamma-Al_2O_3$. The $\alpha-Al_2O_3$ has a trigonal structure that is described as ABAB stacking of oxygen planes with aluminum ions in 2/3 of the octahedral interstitial positions

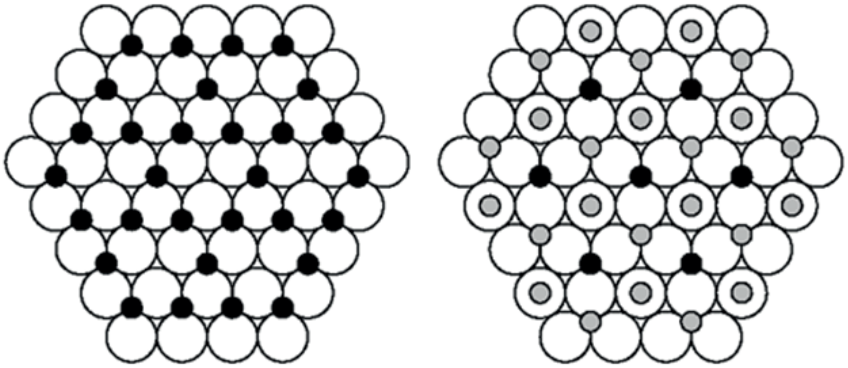

Figure 1.4: The first two layers in the gamma alumina structure. Octahedral Al ions are black, tetrahedral are grey.

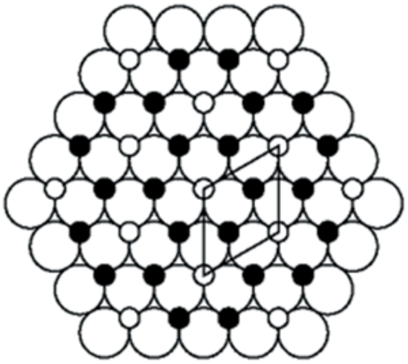

Figure 1.5: The first layer in the alpha alumina structure. Octahedral Al ions are black.

(Fig. 1.5). The oxygen ions form a slightly distorted hexagonal close-packed structure. The hexagonal parameters for $\alpha-\mathrm{Al}_2\mathrm{O}_3$ are $c = 1.297$ nm and $a = 0.475$ nm with cation to anion ratio of 2.73 [80].

1.2.1.3 Eta alumina (η)

The $\eta-Al_2O_3$ has a spinel structure. The structure of $\eta-Al_2O_3$ is similar to $\gamma-Al_2O_3$ except that no aluminum cation occupies the eightfold tetrahedral sites [81]. Based on NMR studies 35% of the aluminum is found to be in tetrahedral sites and cation vacancies were distributed over tetrahedral and octahedral positions. Lippens [64] suggested that $\eta-Al_2O_3$ is tetragonaly deformed and also the degree of tetragonal deformation is a function of the residual OH [82]. The $\eta-Al_2O_3$ has a high number of acid sites, which is used in catalytic industry for isomerization of terminal olefins [83].

1.2.1.4 Delta alumina (δ)

The $\delta-Al_2O_3$ consists of three spinel unit cells with ordered cation vacancies. However, two kinds of unit cells, tetragonal and orthorhombic, have been proposed for $\delta-Al_2O_3$ obtained from different precursors [64, 81]. Repelin and Husson [84] reported that $\delta-Al_2O_3$ contains 80 ions with 4 cation vacancies randomly distributed over octahedral sites. The $\delta-Al_2O_3$ application is mostly reported as a reinforcement in metal matrix composites [85, 86].

1.2.1.5 Chi alumina (χ)

Stumpf et al. [87] proposed that $\chi-Al_2O_3$ has a cubic unit cell, whereas Jan [88] reported a hexagonal unit cell. Hexagonal $\chi-Al_2O_3$ has a layer structure, the aluminum ions occupying octahedral sites within the hexagonal oxygen layers. The stacking of the layers is disordered and has hydroxyl groups.

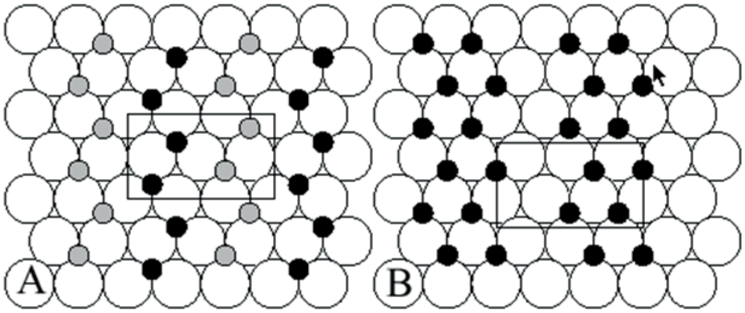

Figure 1.6: The first two layers (A and B) in the kappa alumina structure. Octahedral Al ions are black, tetrahedral are grey.

1.2.1.6 Kappa alumina (κ)

The $\kappa-Al_2O_3$ has an orthorhombic crystal structure with close-packed planes of oxygen in a ABAC-stacking sequence (Fig. 1.6). Three-quarters of aluminum ions exist in octahedral and one-quarter in tetrahedral sites [89]. The $\kappa-Al_2O_3$ is more ordered than $\chi-Al_2O_3$. The $\kappa-Al_2O_3$ is widely prepared in chemical vapor deposition (CVD) technology.

1.2.1.7 Theta alumina (θ)

The $\theta-Al_2O_3$ is a deformed spinel lattice and is considered as an intermediate between the cubic packing and hexagonal close packed structure (Fig. 1.7). The $\theta-Al_2O_3$ has the monoclinic cell and the aluminum cations are distributed equally between tetrahedral and octahedral sites [90].

1.2.2 Current synthesis of alumina

Two main categories to synthesize mesoporous alumina are primary synthesis and secondary synthesis [77]. In the primary synthesis, organic or inorganic alu-

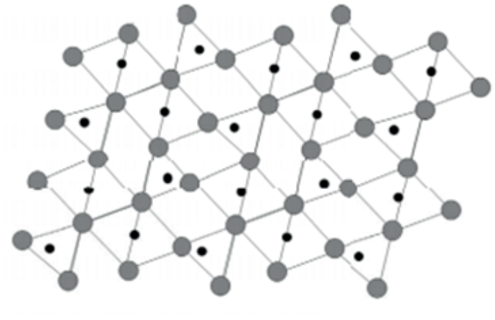

Figure 1.7: Structure of theta-alumina in which half of the Al ions occupy tetrahedral sites. Al ions are black, O ions are grey.

minum compounds are reacted with base to precipitate an aluminum hydrate or hydroxide. The secondary synthesis involves sol gel processing of an aluminum inorganic salt or organic starting materials in the presence of templates or structure-directing agents such as surfactants and polymers through scaffolding [91,92], nanocasting [93], hydrothermal treatment [94], precipitation [95], and cation-anion double hydrolysis [96, 97]. The methods using surfactant are categorized into anionic surfactant, cationic surfactant, and non-ionic surfactant methods [15].

1.2.2.1 Anionic surfactant

Stucky et. al. explained the concept of cooperative formation of inorganic-organic interfaces to synthesize metal oxides [98]. By adjusting the pH of the synthesis mixture, inorganic molecules were promoted to mesophase formation through an electrostatic interaction with organic molecules. Davis et al. [23] produced mesophase alumina by hydrolysis of aluminum alkoxide precursors in low molecular weight alcohol, using C_5 to C_{18} carboxylic acid surfactants. The amount of water used was higher than 3 which is the stoichiometry required in the following reaction (Eq. 1.8).

Alumina with high surface area (710 m^2/g), narrow pore size, low thermal stability, and a disordered pore structure was obtained.

$$Al(OR)_3 + 3H_2O \longrightarrow Al(OH)_3 + 3ROH \tag{1.8}$$

Aluminum *sec*-butoxide precursor and stearic acid surfactant were used to make alumina with pore sizes between 3.7 to 7.7 nm. On the other hand, removal of the surfactant led to the collapse of the structure because of a strong bond between cationic alumina and the surfactant group. Moreover, high concentration of surfactant led to low Al-O-Al connectivity due to coordination of anionic species with aluminum.

1.2.2.2 Cationic surfactant

The inorganic species in solution would be cationic for syntheses carried out in aqueous solution at pH below the isoelectric point of alumina or by hydrolysis of aluminum alkoxides in organic media. Acosta et al. [99] first reported on the synthesis of aluminum hydroxide-cationic surfactant mesophases using alkyltrimethylammonium bromide in aqueous solution. Alumina within the range of 2 to 10 nm was synthesized in 1-butanol and cationic surfactants, using a water to aluminum sec-butoxide molar ratio of 2 (Eq. 1.9).

$$Al(OR)_3 + 2H_2O \longrightarrow AlO(OH) + 3ROH \tag{1.9}$$

1.2.2.3 Non-ionic surfactant

Bagshaw et al. [100] used non-ionic surfactant di-block copolymers containing a hydrophilic poly ethylene oxide (PEO) and a hydrophobic hydrocarbon moiety;

and aluminum *sec*-butoxide was used as a precursor. Mesoporous alumina was synthesized with pore sizes of 2.4 to 4.7 nm and surface areas of 420 to 535 m^2/g, which is higher than other processes using charged surfactant.

However, all methods mentioned above have several limitations in commercial applications:

1. These methods require use of toxic, expensive surfactants and tempelates, and solvents.
2. These processes are multi-step methods which are laborious and time-consuming.
3. The synthesized aluminas have a low thermal stability.

Huang et al. [77,101] have previously reported $\gamma-Al_2O_3$ supports which have high surface areas (> 350 m^2/g) and pore volumes (> 1.7 cm^3/g); and in which the pore diameters can be controlled over a large range (4 to 18 nm) made by an inexpensive, solvent deficient method without the use of templates or surfactants, and the pore size range is further extended from 4 to 37 nm by changing the alcohol used during the gelation [102]. These $\gamma-Al_2O_3$ supports are plate like with large porosity based on slow hydrolysis condition (using small amount of water). Baker [103] proposed that a structure of alumina precursor (bohemite) due to slow hydrolysis leads to formation of plate like alumina (Fig. 1.8).

While $\gamma-Al_2O_3$ is stable during long term use at $500-600$°C, at higher reaction temperatures ($650-1200$°C) and especially in the presence of water vapor, the porous structure collapses due to sintering and structural transformations to other forms of alumina ($\alpha-Al_2O_3$), resulting in lower porosity of the supports, and in some cases, deactivation of the catalyst. Thus, in a number of catalytic reactions taking place at elevated temperatures and high steam concentrations, (e.g. auto

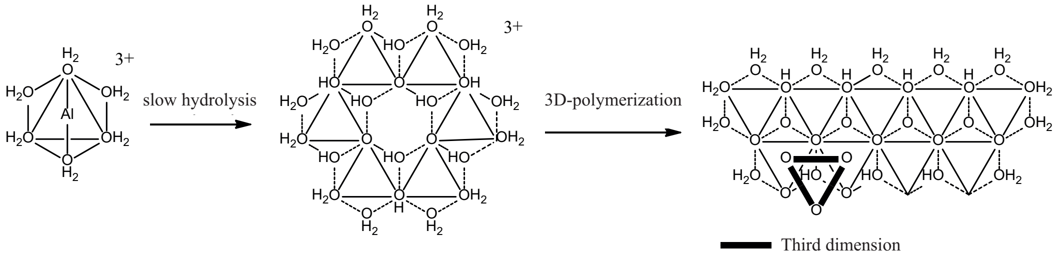

Figure 1.8: Structure of plate-like alumina precursor (bohemite) [103].

emissions control and steam reforming [104–109]) the thermal and hydrothermal stability of $\gamma-Al_2O_3$ is inadequate. Nevertheless, $\gamma-Al_2O_3$ can be stabilized against sintering and phase transformations through the incorporation of suitable dopants (i.e. alkaline earth oxides, transition, and rare-earth elements, as well as SiO_2).

1.2.3 Current synthesis of thermally stable doped-alumina

Previous studies have demonstrated that thermal and hydrothermal stabilities of alumina are substantially improved by the addition of 1 to 20 wt.% silica [107–113], titania [114, 115], zirconia [111, 116, 117], and rare earth elements such as lanthanum [8, 105, 118] and cerium [104, 119, 120]. Of particular pertinence to the present study is the use of silica at 1 to 10 wt.% as a stabilizer for $\gamma-Al_2O_3$. A number of previous papers and patents address the preparation of stable silica-doped alumina. In an early patent, a multi-step co-gel preparation method was reported to produce silica-alumina with high porosity: the alumina sample contained 7% silica, with a surface area of 150 m^2/g, and a pore volume of 0.9 cm^3/g at 1100°C (no pore diameter was reported) [121]. This method involves the reaction of an alkali metal aluminate and silicate, followed by filtration, washing, and drying. Preparation of silica-modified-alumina with 2 to 10% silica using a different co-gel method has also been reported [122]: after calcination at 648°C, the 5% silica sample was reported to have a moderately high surface area of 318 m^2/g and relatively low pore volume of 0.46 cm^3/g. This method uses acid in the sol preparation and base in the gelation step. Wan et. al. [123] reported a stabilized 5.5% silica-alumina support produced by impregnating alumina with polyorgano silane; after calcination at 1100°C and 1200°C, the surface area was 158.2 m^2/g and 93 m^2/g, respectively; however, neither pore volume and nor pore diameter data were reported. Other complex methods involving solvents and pH adjustment techniques have also been used to make stable silica-doped alumina [104, 108, 110, 124]. However, these particular supports do not maintain high surface areas and pore volumes at higher temperatures. For example, Shutilov et al. [108] used an impregnation method to make a stable silica-doped alumina but reported low values for both surface area (68 m^2/g) and pore volume (0.34 cm^3/g) and a moderately large pore diameter (15 nm) at 1100°C. Silica-doped aluminas having high surface area and pore volume at high temperatures have also been synthesized using aerogel and crygol methods, but they are costly and time consuming [107, 109, 112]. For example, Miller [107] produced a stable silica-doped alumina containing 10% silica by the multi-step aerogel method and using supercritical drying to remove the solvent. At 1200°C, it has a surface area of 150 m^2/g and pore volume of 0.65 cm^3/g, which are unusually high for this temperature; no pore diameter data were available. Horiuchi et. al. [109] used supercritical drying to synthesize silica-doped alumina with a surface area of 110 m^2/g, pore volume of 0.9 cm^3/g and pore diameter of 18.6 nm at 1200°C.

From this previous work, it is evident that the addition of silica to alumina produces alumina support materials with substantially higher porosity at high temperatures (relative to pure alumina). Such materials having thermal and hydrothermal stabilities facilitate higher catalyst loadings and increase catalyst lifetime, activity, and productivity at high operating temperatures [6]. However, most of the previous preparation methods involve complex, multi-step procedures and hence higher manufacturing costs. Therefore, it would be desirable to devise simple, low-cost methods that produce such materials that are discussed in Chapter 3 of this dissertation.

1.3 Overview of dissertation

Chapter 1 contains background information on aluminum alkoxides and aluminas, including their structures, properties and synthesis. In Chapter 2, characterization techniques are introduced to determine the structure and textural properties of the aluminas in this research. Chapter 3 introduces a facile one-pot synthesis of a nanosized thermally stable silica-doped alumina (SDA) having a large pore volume (1 cm^3/g) and large bimodal pores (22 and 52 nm). The origin of increased thermal stability for Si doped alumina is also discussed. Chapter 4 includes a statistical method to control porosity and surface area in thermally stable silica-doped alumina support (SDA). Based on statistical models, optimal conditions to produce SDA samples with large (40-60 nm) or medium (16-19 nm) pore diameters, high surface area (> 250 m^2/g and large pore volume (> 1 cm^3/g) are quantitatively predicted. Chapter 5 describes the control of acid site formation on alumina catalyst support by altering different preparation variables in the synthesis method such as Si/Al ratio and calcination temperatures while maintaining high surface are, large porosity and thermal stability of alumina support at higher temperatures. Chapter 6 describes a generalized preparation method and characterization of aluminum isopropoxide, aluminum phenoxide, and aluminum n-hexyloxide as starting materials to produce high surface area nanosized alumina catalyst supports.

Bibliography

[1] W. Jing, F. Shi, W. Xing, and N. Xu, “Gas lifting membrane filtration unitized apparatus,” *Nanjing University of Technology, Peop. Rep. China*, p. 8, 2010. 1

[2] Y. Gu, “Sol-gel preparation of γ-Al_2O_3 ceramic membranes for filtration or gas separation via colloidal boehmite particles of controlled size,” *Corning Inc., USA*, p. 12, 2010. 1

[3] B. L. Krasnyi, A. N. Kislyakov, and A. B. Krasnyi, “Mixture for making porous permeable ceramics for gas filters and membranes,” *ZAO Nauchno-Tekhnicheskii Tsentr "Bakor", Russia*, p. 5, 2009. 1

[4] F. Pfluecker and B. Hirthe, “Particulate uv protection agents based on coated metal oxide pigments for use in cosmetics,” *Merck Patent G.m.b.H., Germany; Sachtleben Chemie G.m.b.H.*, p. 132, 2008. 1

[5] N. Watanabe, K. Otsu, and H. Yoshida, “Alumina flakes, their manufacture, and their use in cosmetics, paints, inks, and plastic compositions,” *Sakai Chemical Industry Co., Ltd., Japan*, p. 16, 2005. 1

[6] A. R. de la Osa, A. De Lucas, A. Romero, J. Valverde, and P. Sanchez, “Influence of the catalytic support on the industrial fischer-tropsch synthetic diesel production,” *Catalysis Today*, vol. 176, pp. 298–302, 2011. 1, 12, 20, 70, 72, 99

[7] O. V. Klimov, M. A. Fedotov, A. V. Pashigreva, S. V. Budukva, E. N. Kirichenko, G. A. Bukhtiyarova, and A. S. Noskov, “Complexes forming from ammonium paramolybdate, orthophosphoric acid, cobalt or nickel nitrate, and carbamide in solution and their use in the preparation of diesel fuel hydrodesulfurization catalysts,” *Kinet. Catal.*, vol. 50, no. 6, pp. 867–873, 2009. 1, 12, 70, 99

[8] M. Ozawa, “Thermal stabilization of catalytic compositions for automobile exhaust treatment through rare earth modification of alumina nanoparticle support,” *J. Alloys Compd.*, vol. 408-412, pp. 1090–1095, 2006. 1, 12, 19, 70, 71, 99

[9] D. N. Belton and K. C. Taylor, “Automobile exhaust emission control by catalysts,” *Curr. Opin. Solid State Mater. Sci.*, vol. 4, no. 1, pp. 97–102, 1999. 1, 99

[10] K. C. Taylor, “Nitric oxide catalysis in automotive exhaust systems,” *Catal. Rev. - Sci. Eng.*, vol. 35, no. 4, pp. 457–81, 1993. 1, 99

[11] C. H. Bartholomew and R. J. Farrauto, *Fundumental of industrial catalytic processes*, 2nd ed. John Wiley and sons Inc., 2006. 1, 12, 70, 99

[12] R. K. Oberlander, “Aluminas for catalysts-their preparation and properties,” *Applied industrial catalysis*, vol. 3, 1983. xii, 1, 2, 3

[13] K. Wefers and C. Misra, “Oxides and hydroxides of aluminum,” *Alcoa technical paper no.19*, 1987. 2, 3, 11

[14] J. Cejka, “Organized mesoporous alumina: synthesis, structure and potential in catalysis,” *Applied catalysis A*, vol. 254, pp. 327–338, 2003. 2, 9, 12, 70, 99

[15] C. Marquez-Alvarez, N. Zilkova, J. Perez-Pariente, and J. Cejka, “Synthesis, characterization and catalytic applications of organized mesoporous aluminas.” *Catalysis Reviews*, vol. 50, pp. 222–286, 2008. 2, 16

[16] C. H. Bartholomew and R. J. Farrauto, *Fundumentals of industrial catalytic processes*, 2nd ed. John Wiley and sons Inc., 2006. xii, 2, 41, 42, 81, 82, 126, 137

[17] F. Kuhlmann, “Untersuchungen ber die aetherbildung,” *Justus Liebigs Annalen der Chemie*, vol. 33, no. 1, pp. 97–110, 1840. 3

[18] Z. Tishchenko V.E., *J. Russ. Phys. Chem. Soc*, vol. 31, pp. 694, 784, 1899. 3

[19] R. G. Jones, E. Bindschadler, D. Blume, G. Karmas, J. Martin, G. A., J. R. Thirtle, F. A. Yeoman, and H. Gilman, “Organic compounds of uranium. vi. uranium(vi) alkoxides,” *J. Am. Chem. Soc.*, vol. 78, pp. 6030–2, 1956. 3, 101

[20] R. G. Jones, E. Bindschadler, D. Blume, G. Karmas, J. Martin, G. A., J. R. Thirtle, and H. Gilman, “Organic compounds of uranium. v. derivatives of uranium(v) alkoxides,” *J. Am. Chem. Soc.*, vol. 78, pp. 6027–9, 1956. 3

[21] D. C. Bradley, “Metal alkoxides and dialkylamides,” *Advan. Inorg. Chem. Radiochem.*, vol. 15, pp. 259–322, 1972. 3

[22] N. Y. Turova, *The Chemistry of Metal Alkoxides*, 2002. 3, 4, 5, 150, 152

[23] F. Vaudry, S. Khodabandeh, and M. E. Davis, “Synthesis of pure alumina mesoporous materials,” *Chem. Mater.*, vol. 8, no. 7, pp. 1451–1464, 1996. 3, 6, 16, 99, 100, 151

[24] S. S. Karpiniec, "Revisiting the aufbau reaction with acetylene: Further insights from experiment and theory," *Organometallics*, vol. 30, pp. 1569–1576, 2011. 4

[25] S.-J. Yoo, H.-S. Yoon, H. D. Jang, M.-J. Lee, S.-I. Lee, S. T. Hong, and H. S. Park, "Dissolution kinetics of aluminum can in isopropyl alcohol for aluminum isopropoxide," *Chem. Eng. J. (Amsterdam, Neth.)*, vol. 133, no. 1-3, pp. 79–84, 2007. 4

[26] D. C. Bradley, "Metal alkoxides as precursors for electronic and ceramic materials," *Chem. Rev.*, vol. 89, no. 6, pp. 1317–22, 1989. 4

[27] D. C. Bradley, R. C. Mehrotra, I. P. Rothwell, and A. Singh, *Alkoxo and Aryloxo Derivatives of Metals*, 2001. 4, 150, 152

[28] S.-J. Yoo, J.-W. Lee, U.-Y. Hwang, H.-S. Yoon, and H.-S. Park, "Effect of aging among -alo(oh) sol preparation steps variables to control microstructure of γ-Al_2O_3 particles," *Hwahak Konghak*, vol. 35, no. 6, pp. 832–837, 1997. 4, 9

[29] D. C. Bradley, "Metal alkoxides," *Preparative Inorg. Reactions (William L. Jolly, editor. Interscience)*, vol. 2, pp. 169–86, 1965. 5, 6

[30] D. C. Bradley, M. H. Chisholm, M. W. Extine, and M. E. Stager, "Some reactions of hexakis(dimethylamido)tungsten(vi)," *Inorg. Chem.*, vol. 16, no. 7, pp. 1794–801, 1977. 5

[31] E. P. Turevskaya, N. I. Kozlova, N. Y. Turova, and V. G. Kessler, "Vanadium(v) alcoholates. the relation of vanadyl chloride to organic solvents," *Koord. Khim.*, vol. 14, no. 7, pp. 926–33, 1988. 5

[32] N. Y. Turova, E. P. Turevskaya, V. G. Kessler, N. I. Kozlova, and A. I. Belokon, “Metal 2-methoxyethoxides,” *Zh. Neorg. Khim.*, vol. 37, no. 1, pp. 50–9, 1992. 5

[33] 5

[34] M. Baca, E. de la Rochefoucauld, E. Ambroise, J.-M. Krafft, R. Hajjar, P. P. Man, X. Carrier, and J. Blanchard, “Characterization of mesoporous alumina prepared by surface alumination of sba-15,” *Microporous Mesoporous Mater.*, vol. 110, no. 2-3, pp. 232–241. 6, 151

[35] M. K. Dongare and A. P. B. Sinha, “Low-temperature preparation of γ-Al_2O_3 by an alkoxide route,” *Bull. Mater. Sci.*, vol. 11, no. 4, pp. 281–6, 1988. 6, 151, 152

[36] Z. Yu, Q. Zhao, and Q. Zhang, “Preparation of ultrafine alumina powders from aluminum isopropoxide,” *Trans. Nonferrous Met. Soc. China*, vol. 4, no. 2, pp. 21–4, 1994. 6, 151

[37] M. May, J. Navarrete, M. Asomoza, and R. Gomez, “Tailored mesoporous alumina prepared from different aluminum alkoxide precursors,” *J. Porous Mater.*, vol. 14, no. 2, pp. 159–164, 2007. 6, 9, 150, 151, 152

[38] S. Handjani, J. Blanchard, E. Marceau, P. Beaunier, and M. Che, “From mesoporous alumina to pt/al2o3 catalyst: A comparative study of the aluminas synthesis in aqueous medium, physicochemical properties and stability,” *Microporous Mesoporous Mater.*, vol. 116, no. 1-3, pp. 14–21, 2008. 6, 151

[39] K. Tadanaga, N. Yamaguchi, A. Matsuda, T. Minami, and M. Tatsumisago, “Effects of various additives during hot water treatment on the formation of

alumina thin films for superhydrophobic surfaces," *J. Adhes. Sci. Technol.*, vol. 22, no. 3-4, pp. 387–394, 2008. 6, 151

[40] S. Kureti and W. Weisweiler, "A novel sol-gel method for the synthesis of γ-Al_2O_3: development of the sol-gel transformation and characterization of the xerogel," *J. Non-Cryst. Solids*, vol. 303, no. 2, pp. 253–261, 2002. 6, 151

[41] H. Park, S. H. Yang, Y.-S. Jun, W. H. Hong, and J. K. Kang, "Facile route to synthesize large-mesoporous γ-Al_2O_3 by room temperature ionic liquids," *Chem. Mater.*, vol. 19, no. 3, pp. 535–542, 2007. 6, 151

[42] N. Tomar and R. Nagarajan, "Effect of phenyl group on the structure and formation of transitional alumina from $Al(OPh)_3$," *J. Sol-Gel Sci. Technol.*, vol. 53, no. 2, pp. 293–299, 2010. 6, 7, 150, 151, 152, 156, 157, 159

[43] R. Lichtenberger, "Modification of aluminum alkoxides with dialkylmalonates," *Monatsch Chem*, vol. 141, pp. 717–727, 2010. 7, 151

[44] A. Abraham, R. Prins, J. A. van Bokhoven, E. R. H. Van Eck, and A. P. M. Kentgens, "Multinuclear solid-state high-resolution and ^{13}C NMR - ^{27}Al NMR double-resonance magic-angle spinning NMR studies on aluminum alkoxides," *J. Phys. Chem. B*, vol. 110, no. 13, pp. 6553–6560, 2006. 7, 151, 162

[45] M. M. Sovar, D. Samelor, A. N. Gleizes, and C. Vahlas, "Aluminium tri-iso-propoxide: Shelf life, transport properties, and decomposition kinetics for the low temperature processing of aluminum oxide-based coatings," *Surf. Coat. Technol.*, vol. 201, no. 22-23, pp. 9159–9162, 2007. 7, 151, 152

[46] J. Shiner, V. J., D. Whittaker, and V. P. Vernandez, “The structures of some aluminum alkoxides,” *J. Am. Chem. Soc.*, vol. 85, no. 15, pp. 2318–22, 1963. 7, 151

[47] J. A. Meese-Marktscheffel, R. E. Cramer, and J. W. Gilje, “Magnesium-aluminum alkoxides,” *Polyhedron*, vol. 13, no. 6-7, pp. 1045–50, 1994. 7, 151

[48] H. Noth, “Di-, tii-, and tetranuclear alkoxyaluminum h ydrides,” *Angew. Chem. Int. Ed. Engl.*, vol. 36, no. 23, 1997. 7, 151

[49] Z. A. Starikova, “New polynuclear aluminium oxoalkoxides,” *Polyhedron*, vol. 23, pp. 109–114, 2004. 7, 151

[50] A. Pandey, “Synthesis and characterization of the heterometallic aggregate,” *Eur. J. Inorg. Chem.*, pp. 1291–1293, 1999. 7, 151

[51] J. J. Ebelmen, “Sur une production artificielle de silice diaphane,” *comptes Rendus*, vol. 19, 1844. 7

[52] E. Grimaux, “Preperation new method for production of colloidal silica solution, also new synthetic organic colloid.” *comptes Rendus*, vol. 98, 1884. 7

[53] W. A. Patrick, “Silica gel and process of making same,” *U.S. Patent 1,297,724*, 1919. 8

[54] ——, “Catalysts,” *British Patent 208,656*, 1923. 8

[55] ——, “Porous catalytic gels,” *U.S. Patent 1,577,186*, 1926. 8

[56] ——, “Adsorbent and catalytic oxides,” *U.S. Patent 1,520,305*, 1924. 8

[57] ——, “Aluminum oxide gel,” *U.S. Patent 1,682,241*, 1928. 8

[58] B. E. Yoldas, "Introduction and effect of structural variations in inorganic polymers and glass networks," *J. Non-Cryst. Solids*, vol. 51, no. 1, 1982. 8

[59] ——, "Investigations of porous oxides as an antireflective coating for glass surfaces," *Appl Opt*, vol. 19, no. 9, pp. 1425–9, 1980. 8

[60] Y. Wu, G. Xia, K. Wang, Q. Wang, B. Liu, X. Sun, C. Hou, M. Li, H. Nie, and D. Li, "Modified alumina support based Fischer-Tropsch synthesis catalyst and its application," *China Petroleum and Chemical Corp., Peop. Rep. China; SINOPEC Research Institute of Petroleum Processing*, p. 10. 9, 150

[61] X. Wang, "Preparation of coal tar hydrocracking catalyst containing amorphous silica-alumina," *Peop. Rep. China*, p. 11. 9

[62] A. Jean-Marie, A. Griboval-Constant, A. Y. Khodakov, and F. Diehl, "Cobalt supported on alumina and silica-doped alumina: Catalyst structure and catalytic performance in Fischer-Tropsch synthesis," *C. R. Chim.*, vol. 12, no. 6-7, pp. 660–667, 2009. 9

[63] R. K. Oberlander, "Aluminas for catalysts-their preparation and properties," *Applied industrial catalysis*, vol. 3, 1983. 9

[64] B. C. Lippens and J. H. de Boer, "Study of phase transformations during calcination of aluminum hydroxides by selected area electron diffraction," *Acta Crystallogr.*, vol. 17, no. 10, pp. 1312–21, 1964. 11, 14

[65] S. J. Wilson, "The dehydration of boehmite, γ-AlOOH, to γ-alumina, journal = J. Solid State Chem., volume = 30, number = 2, pages = 247-55, year = 1979, type = Journal Article." 11, 12

[66] Y. G. Wang, P. M. Bronsveld, J. T. M. Dehosson, B. Djuricic, D. McGarry, and S. Pickering, “Ordering of octahedral vacancies in transition aluminas,” *J. Am. Ceram. Soc.*, vol. 81, no. 6, pp. 1655–1660, 1998. 12

[67] H. Saalfeld, “The dehydration of gibbsite and the structure of a tetragonal γ-Al_2O_3,” *Clay Miner. Bull.*, vol. 3, pp. 249–56, 1958. 12

[68] J. A. Wang, X. Bokhimi, A. Morales, O. Novaro, T. Lopez, and R. Gomez, “Aluminum local environment and defects in the crystalline structure of sol-gel alumina catalyst,” *J. Phys. Chem. B*, vol. 103, no. 2, pp. 299–303, 1999. 12

[69] M. H. Lee, C.-F. Cheng, V. Heine, and J. Klinowski, “Distribution of tetrahedral and octahedral al sites in gamma alumina,” *Chem. Phys. Lett.*, vol. 265, no. 6, pp. 673–676, 1997. 12

[70] C. Wolverton and K. C. Hass, “Phase stability and structure of spinel-based transition aluminas,” *Phys. Rev. B Condens. Matter Mater. Phys.*, vol. 63, no. 2, pp. 024 102/1–024 102/16, 2001. 12

[71] G. Gutierrez, A. Taga, and B. Johansson, “Theoretical structure determination of γ-Al_2O_3,” *Phys. Rev. B Condens. Matter Mater. Phys.*, vol. 65, no. 1, pp. 012 101/1–012 101/4, 2002. 12

[72] C. S. John, N. C. M. Alma, and G. R. Hays, “Characterization of transitional alumina by solid-state magic angle spinning aluminum NMR,” *Appl. Catal.*, vol. 6, no. 3, pp. 341–6, 1983. 12

[73] S. J. Smith, S. Amin, B. F. Woodfield, J. Boerio-Goates, and B. J. Campbell, "Phase progression of gamma-Al_2O_3 nanoparticles synthesized in a solvent-deficient environment," *Inorg. Chem.*, vol. 52, no. 8, pp. 4411–4423, 2013. 12, 85, 86

[74] H. Pines and W. O. Haag, "Alumina: catalyst and support. ix. the alumina catalyzed dehydration of alcohols," *J. Am. Chem. Soc.*, vol. 83, pp. 2847–52, 1961. 12, 70, 126

[75] B.-G. J. Liu S., L. Q. and W. B. F., "Preparation of uniform nanoparticles of ultra-high purity metal oxides, mixed metal oxides, metals, and metal alloys ii," 2006. 12, 70, 135, 139, 141

[76] C. Bartholomew, B. Woodfield, B. Huang, O. Rebecca, and L. Astle, "Method for making highly porous, stable metal oxide with a controlled pore structure," *in: WO Application Brigham Young University*, p. 40, 2011. 12, 70

[77] B. Huang, C. H. Bartholomew, S. J. Smith, and B. F. Woodfield, "Facile solvent-deficient synthesis of mesoporous γ-Al_2O_3 with controlled pore structures," *Microporous Mesoporous Mater.*, vol. 165, pp. 70–78, 2013. 12, 15, 18, 70, 85, 115, 150, 157

[78] C. Morterra and G. Magnacca, "A case study: surface chemistry and surface structure of catalytic aluminas, as studied by vibrational spectroscopy of adsorbed species," *Catal. Today*, vol. 27, no. 3-4, pp. 497–532, 1996. 12, 70, 99

[79] R. K. Oberlander, "Aluminas for catalysts - their preparation and properties," *Appl. Ind. Catal.*, vol. 3, pp. 63–112, 1984. 12, 70, 99

[80] A. J. Bourdillon, S. M. El-Mashri, and A. J. Forty, “Application of tem extended electron energy loss fine structure to the study of aluminum oxide films,” *Philos. Mag. A*, vol. 49, no. 3, pp. 341–52, 1984. 13

[81] R. S. Zhou and R. L. Snyder, “Structures and transformation mechanisms of the η, γ and θ transition aluminas,” *Acta Crystallogr., Sect. B Struct. Sci.*, vol. B47, no. 5, pp. 617–30, 1991. 14

[82] K. Shirasuka, H. Yanagida, and G. Yamaguchi, “The preparation of ?-alumina and its structure,” *Yogyo Kyokai Shi*, vol. 84, no. 12, pp. 610–13, 1976. 14

[83] K. Sohlberg, S. T. Pantelides, and S. J. Pennycook, “Surface reconstruction and the difference in surface acidity between γ- and η-alumina,” *J. Am. Chem. Soc.*, vol. 123, no. 1, pp. 26–29, 2001. 14

[84] Y. Repelin and E. Husson, “Studies of structural transition in aluminas. i.γ and δ-aluminas,” *Mater. Res. Bull.*, vol. 25, no. 5, pp. 611–21, 1990. 14

[85] H. Akbulut and M. Durman, “Temperature dependent strength analysis of short fiber reinforced al-si metal matrix composites,” *Mater. Sci. Eng., A*, vol. A262, no. 1-2, pp. 214–226, 1999. 14

[86] T. W. Clyne, M. G. Bader, G. R. Cappleman, and P. A. Hubert, “The use of a δ-alumina fiber for metal-matrix composites,” *J. Mater. Sci.*, vol. 20, no. 1, pp. 85–96, 1985. 14

[87] H. C. Stumpf, A. S. Russell, J. W. Newsome, and C. M. Tucker, “Thermal transformations of aluminas and alumina hydrates,” *Ind. Eng. Chem.*, vol. 42, pp. 1398–1403, 1950. 14

[88] J. H. Boer and B. G. Linsen, “Physical and chemical aspects of adsorbents and catalysts: Dedicated to J. H. De Boer on the occasion of his retirement from the Technological University,” 1970. 14

[89] B. Ollivier, R. Retoux, P. Lacorre, D. Massiot, and G. Ferey, “Crystal structure of κ-alumina: an x-ray powder diffraction, TEM and NMR study,” *J. Mater. Chem.*, vol. 7, no. 6, pp. 1049–1056, 1997. 15

[90] S.-H. Cai, S. N. Rashkeev, S. T. Pantelides, and K. Sohlberg, “Phase transformation mechanism between γ- and θ-alumina,” *Phys. Rev. B Condens. Matter Mater. Phys.*, vol. 67, no. 22, 2003. 15

[91] Z. Zhang, R. W. Hicks, T. R. Pauly, and T. J. Pinnavaia, “Mesostructured forms of γ-Al_2O_3,” *J. Am. Chem. Soc.*, vol. 124, no. 8, pp. 1592–1593, 2002. 16, 99, 100

[92] H. Y. Zhu, X. P. Gao, D. Y. Song, Y. Q. Bai, S. P. Ringer, Z. Gao, Y. X. Xi, W. Martens, J. D. Riches, and R. L. Frost, “Growth of boehmite nanofibers by assembling nanoparticles with surfactant micelles,” *J. Phys. Chem. B*, vol. 108, no. 14, pp. 4245–4247, 2004. 16

[93] W.-C. Li, A.-H. Lu, W. Schmidt, and F. Schueth, “High surface area, mesoporous, glassy alumina with a controllable pore size by nanocasting from carbon aerogels,” *Chem. - Eur. J.*, vol. 11, no. 5, pp. 1658–1664, 2005. 16

[94] H. C. Lee, H. J. Kim, C. H. Rhee, K. H. Lee, J. S. Lee, and S. H. Chung, “Synthesis of nanostructured γ-Al_2O_3 with a cationic surfactant and controlled amounts of water,” *Microporous Mesoporous Mater.*, vol. 79, no. 1-3, pp. 61–68, 2005. 16

[95] R. Zhao, F. Guo, Y. Hu, and H. Zhao, “Self-assembly synthesis of organized mesoporous alumina by precipitation method in aqueous solution,” *Microporous Mesoporous Mater.*, vol. 93, no. 1-3, pp. 212–216, 2006. 16

[96] P. Bai, P. Wu, Z. Yan, and X. S. Zhao, “A reverse cation-anion double hydrolysis approach to the synthesis of mesoporous γ-Al_2O_3 with a bimodal pore size distribution,” *Microporous Mesoporous Mater.*, vol. 118, no. 1-3, pp. 288–295, 2009. 16

[97] C. Lesaint, G. Kleppa, D. Arla, W. R. Glomm, and G. Oeye, “Synthesis and characterization of mesoporous alumina materials with large pore size prepared by a double hydrolysis route,” *Microporous Mesoporous Mater.*, vol. 119, no. 1-3, pp. 245–251, 2009. 16

[98] Q. Huo, D. I. Margolese, U. Ciesla, D. G. Demuth, P. Feng, T. E. Gier, P. Sieger, A. Firouzi, B. F. Chmelka, and et al., “Organization of organic molecules with inorganic molecular species into nanocomposite biphase arrays,” *Chem. Mater.*, vol. 6, no. 8, pp. 1176–91, 1994. 16

[99] S. Acosta, A. Ayral, C. Guizard, and L. Cot, “Synthesis of alumina gels in amphiphilic media,” *J. Sol-Gel Sci. Technol.*, vol. 8, no. 1/2/3, pp. 195–199, 1997. 17

[100] S. A. Bagshaw and T. J. Pinnavaia, “Mesoporous alumina molecular sieves,” *Angew. Chem., Int. Ed. Engl.*, vol. 35, no. 10, pp. 1102–1105, 1996. 17, 99, 100

[101] B. Huang, C. H. Bartholomew, S. J. Smith, and B. F. Woodfield, “Facile solvent-deficient synthesis of mesoporous γ-Al_2O_3 with controlled pore struc-

tures," *Microporous Mesoporous Mater.*, vol. 165, pp. 70–78, 2013. 18, 100, 151

[102] B. Huang, C. H. Bartholomew, and B. F. Woodfield, "Facile structure-controlled synthesis of mesoporous γ-Al_2O_3: Effects of alcohols in precursor formation and calcination," *Microporous Mesoporous Mater.*, vol. 177, pp. 37–46, 2013. 18, 100, 115, 117, 151

[103] B. R. Baker and R. M. Pearson, "Water content of pseudoboehmite. new model for its structure," *J. Catal.*, vol. 33, no. 2, pp. 265–78, 1974. xiv, 18, 19, 115

[104] J. W. Curley, M. J. Dreelan, and O. E. Finlayson, "High temperature stability of alumina fiber," *Catal. Today*, vol. 10, no. 3, pp. 401–4, 1991. 19, 20, 71, 82, 99, 128

[105] T. Fukui and M. Hori, "Thermal stability of aluminas by hydrothermal treatment of an alkoxide-derived gel," *J. Mater. Sci.*, vol. 30, no. 7, pp. 1794–800, 1995. 19, 71

[106] T. Horiuchi, T. Osaki, T. Sugiyama, H. Masuda, M. Horio, K. Suzuki, T. Mori, and T. Sago, "High surface area alumina aerogel at elevated temperatures," *J. Chem. Soc., Faraday Trans.*, vol. 90, no. 17, pp. 2573–8, 1994. 19, 71, 84, 99

[107] J. B. Miller and E. I. Ko, "A homogeneously dispersed silica dopant for control of the textural and structural evolution of an alumina aerogel," *Catal. Today*, vol. 43, no. 1-2, pp. 51–67, 1998. xii, 19, 20, 71, 72, 82, 88, 99

[108] A. A. Shutilov, G. A. Zenkovets, S. V. Tsybulya, and V. Y. Gavrilov, "Effect of silica on the stability of the nanostructure and texture of fine-particle alumina," *Kinet. Catal.*, vol. 53, no. 1, pp. 125–136, 2012. xii, 19, 20, 71, 72, 82, 88, 128

[109] T. Horiuchi, L. Chen, T. Osaki, T. Sugiyama, K. Suzuki, and T. Mori, "A novel alumina catalyst support with high thermal stability derived from silica-modified alumina aerogel," *Catal. Lett.*, vol. 58, no. 2,3, pp. 89–92, 1999. xii, 19, 20, 71, 72, 82, 85, 87, 88, 99, 115

[110] A. W. Espie and J. C. Vickerman, "Aluminas modified with silica. part 1. an x-ray diffraction and secondary-ion mass spectrometry study of the influence of preparation and thermal treatment on structure and surface composition," *J. Chem. Soc., Faraday Trans. 1*, vol. 80, no. 7, pp. 1903–13, 1984. 19, 20, 71, 128

[111] J. Klein and W. F. Maier, "Thermal stability of sol-gel-derived porous AM−AlxZr mixed oxides," *Chem. Mater.*, vol. 11, no. 9, pp. 2584–2593, 1999. 19, 71

[112] T. Osaki, K. Nagashima, K. Watari, and K. Tajiri, "Silica-doped alumina cryogels with high thermal stability," *J. Non-Cryst. Solids*, vol. 353, no. 24-25, pp. 2436–2442, 2007. xii, 19, 20, 71, 72, 82, 88, 128

[113] J.-H. Lee, S.-C. Choi, D.-S. Bae, and K.-S. Han, "Synthesis and microstructure of silica-doped alumina composite membrane by sol-gel process," *J. Mater. Sci. Lett.*, vol. 18, no. 17, pp. 1367–1369, 1999. 19, 71

[114] G. Lopez-Granada, J. D. O. Barceinas-Sanchez, R. Lopez, and R. Gomez, "High temperature stability of anatase in titania-alumina semiconductors with enhanced photodegradation of 2, 4-dichlorophenoxyacetic acid," *J. Hazard. Mater.*, p. Ahead of Print, 2013. 19, 71

[115] X. Jiang, B. P. Bastakoti, W. Weng, T. Higuchi, H. Oveisi, N. Suzuki, W.-J. Chen, Y.-T. Huang, and Y. Yamauchi, “Preparation of ordered mesoporous alumina-doped titania films with high thermal stability and their application to high-speed passive-matrix electrochromic displays,” *Chem. - Eur. J.*, vol. 19, no. 33, pp. 10 958–10 964, 2013. 19, 71

[116] T. Horiuchi, Y. Teshima, T. Osaki, T. Sugiyama, K. Suzuki, and T. Mori, “Improvement of thermal stability of alumina by addition of zirconia,” *Catal. Lett.*, vol. 62, no. 2-4, pp. 107–111, 1999. 19, 71

[117] R. H. R. Castro, S. V. Ushakov, L. Gengembre, D. Gouvea, and A. Navrotsky, “Surface energy and thermodynamic stability of gamma-alumina: Effect of dopants and water,” *Chem. Mater.*, vol. 18, no. 7, pp. 1867–1872, 2006. 19, 71

[118] Z. Cai, J. Li, K. Liew, and J. Hu, “Effect of La_2O_3-dopping on the Al_2O_3 supported cobalt catalyst for fischer-tropsch synthesis,” *J. Mol. Catal. A: Chem.*, vol. 330, no. 1-2, pp. 10–17, 2010. 19, 71

[119] M. Schoeneborn, A. Paeger, and R. Gloeckler, “Ceria zirconia alumina composition with enhanced thermal stability,” *Sasol Germany GmbH, Germany.*, p. 14, 2013. 19, 71

[120] K. Schermanz, A. Sagar, M. Schoeneborn, R. Gloeckler, K. Dallmann, F. Alber, and S. Rolfs, “Ceria zirconia alumina composition with enhanced thermal stability,” *(Treibacher Industrie AG, Austria; Sasol Germany GmbH).*, p. 34, 2013. 19, 71

[121] R. J. Nozemack and J. F. Porinchak, “Alumina-silica cogel,” *W. R. Grace and Co., Newyork, N.Y.*, 1988. 19, 71, 82

[122] H. K. C. Timken, “Homogeneous modified-alumina Fischer-Tropsch catalyst supports,” p. 8, 2005. 19, 71, 82

[123] C. Z. Wan and J. C. Dettling, “Stabilized alumina catalyst support coatings,” *Engelhard Corp., USA*, p. 23, 1986. 20, 71, 82

[124] T. Fukui and M. Hori, “Control of micropore size distribution in alumina by the hydrothermal treatment of an alkoxide derived-alcogel,” *J. Mater. Sci.*, vol. 31, no. 12, pp. 3245–3248, 1996. 20, 71

Chapter 2

Characterization Techniques

2.1 Introduction

The factors determining the properties of nanoparticles are the arrangement of atoms, particle size, surface area of agglomerates and particles; and morphology (size and shape) of primary crystallite. Therefore, determination of nanoparticle structures and morphologies are critical to the design, preparation, and applications of such materials.

In this dissertation, X-ray diffraction (XRD), magic-angle spinning nuclear magnetic resonance (MAS NMR), and transmission electron microscopy (TEM) are used to study atomic arrangement, particle size, and agglomerate morphology of nanosized silica-doped alumina. Their surface area, pore volume, and pore size distribution are determined by nitrogen gas adsorption techniques. A basic outline of these techniques and the information they provide is given in the following sections.

2.2 BET and Pore properties

2.2.1 Gas adsorption

Adsorption is a useful tool to characterize porous materials, allowing the determination of surface area, pore size distribution and porosity. When the gas or vapor phase (adsorbate) is in contact with a solid surface, it can physically be adsorbed

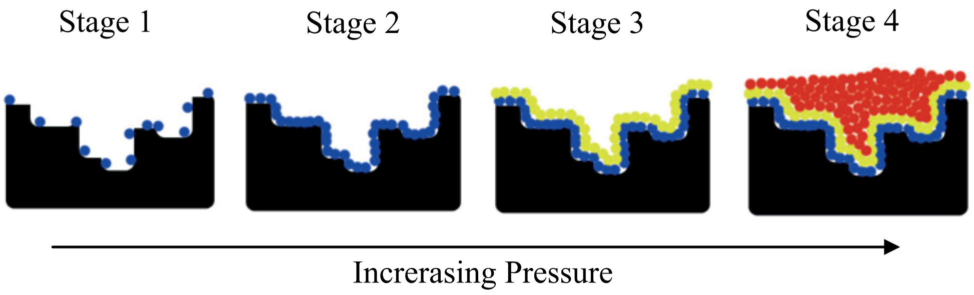

Figure 2.1: Four stages of gas adsorption on the solid surface in BET analyzer.

to the surface via weak Van der Waals interactions. There are some characteristics of physical adsorption:

1. Physical adsorption is fully reversible, allowing the adsorbate to fully adsorb and desorb.
2. Adsorption equilibrium is reached quickly since no activation energy is required.
3. Physical adsorption involves multiple layers of adsorbate, thus allowing pore volume and pore diameter measurments.

Figure 2.1 shows the four stages of gas adsorption on the solid surface in a BET analyzer to measure surface area, pore volume, and pore size distribution. At stage (1), the solid surface begins to adsorb the adsorbate (gas) at low pressure. At stage (2), monolayer formation starts as the gas pressure increases. At stage (3), the solid surface begins to form multi-layer coverage as the pressure increases. At stage (4), gas pressure further increases, which results in complete coverage of the sample and filling of all the pores. From the data in stages 3 and 4, the calculations are used to determine the surface area and porosity, respectively. The calculation methods are discussed later in this section.

Table 2.1: Available data from full range isotherm [1].

Region	Pressure range	Information
Henry's Law region	$P/P_o<0.01$	Surface area calculated using Henry's Law
Monolayer region	$0.05<P/P_o<0.3$	Surface area calculated from linear form of BET eq.
Multilayer region	$0.3<P/P_o<1$	Pore volume determined at $P/P_o=1$ Pore structure obtained from shape of hysteresis curve Pore volume and pore size distribution determined using Kelvin eq.

2.2.2 Adsorption isotherms

Adsorption is usually described through isotherms, which is the amount of adsorbate on the adsorbent as a function of its pressure at constant temperature (typically liquid N_2, 77 K). Adsorption isotherms provide valuable information about the adsorbent's surface structure, surface area, and pore size in the case of porous materials (see Table 2.1).

An adsorption isotherm is obtained through a point by point procedure. A sufficient amount of adsorbate N_2 is introduced to the sample and the system is allowed to reach equilibrium. The pressure is measured at each level, producing a series of points to form an adsorption isotherm. Before the measurement, each sample is degassed at $150-200°C$ under nitrogen flow to remove water. Adsorption isotherms are classified by Brunauer, Deming, and Teller [2,3] (see Fig. 2.2) into six types:

Type I: Obtained when adsorption is restricted to a monolayer. Pores are typically microporus with the exposed surface residing almost exclusively inside the micropores, which once filled with adsorbate, leave little or no external surface for further adsorption.

Type II: Frequently encountered and represent multilayer physical adsorption. Most frequently found when adsorption occurs on nonporous powders or powders with diameters exceeding micropores.

Type III: Shows no rapid initial uptake of gas and occurs when the forces of adsorption in the first monolayer are relatively small. Adsorption proceeds when the adsorbate interaction with an adsorbed layer is greater than the interaction with the adsorbent surface.

Type IV: Occur on porous adsorbents with pores in the range of 1.5-100 nm. At higher pressures the slope shows increased uptake of adsorbate when pores become filled. A hysteresis loop arises from capillary condensation in mesopores.

Type V: Observed where there is small adsorbate-absorbent interaction potentials (similar to type III) and are also associated with pores in the 1.5-100 nm range.

Type VI: Associated with layer by layer adsorption on a highly uniform surface, which is rare.

The characteristics of hysteresis loops in isotherms (shown in type IV in Fig. 2.2) can give information on pore shape and pore arrangement [1]. There are four types of hysteresis loops (H1, H2, H3, and H4) as shown in Fig. 2.3. The H1 hysteresis is the result of adsorbents with a narrow pore size distribution of uniform pores. The H2 hysteresis is given by the closely packed spherical particles with uniform size or from a complex, interconnected pore network. The H3 hysteresis is observed from the aggregates of plate-like particles or adsorbents with slit-like pores.

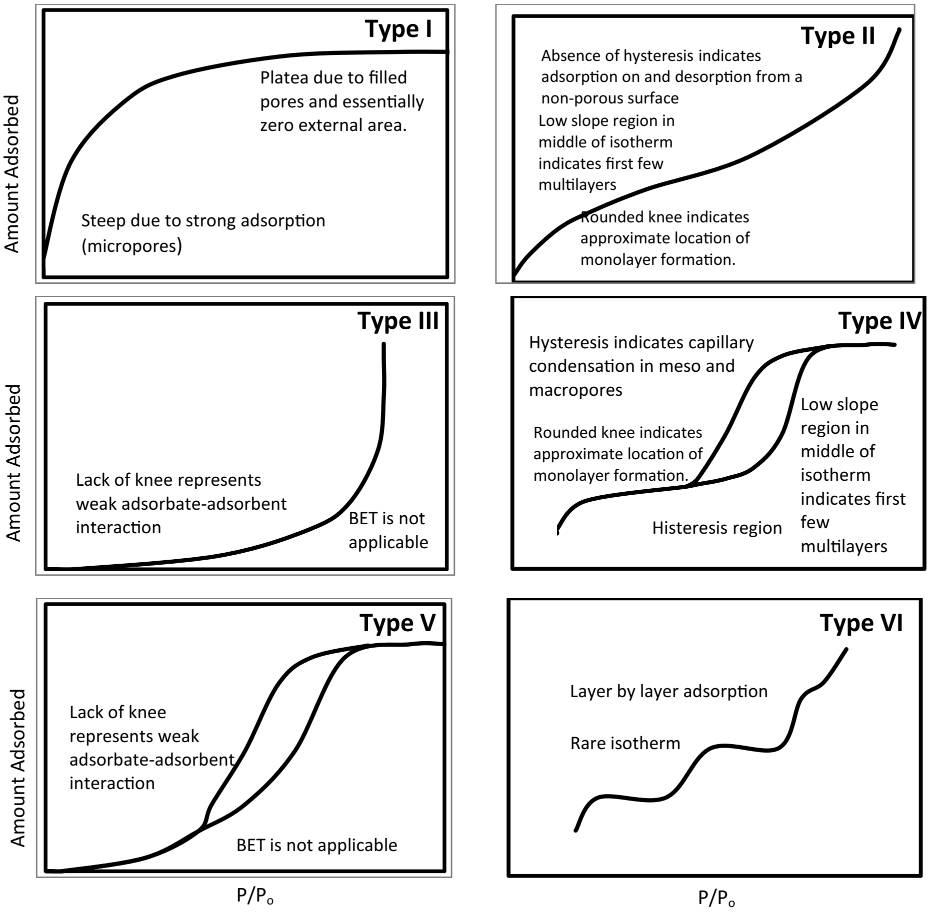

Figure 2.2: The six types of adsorption isotherms [2].

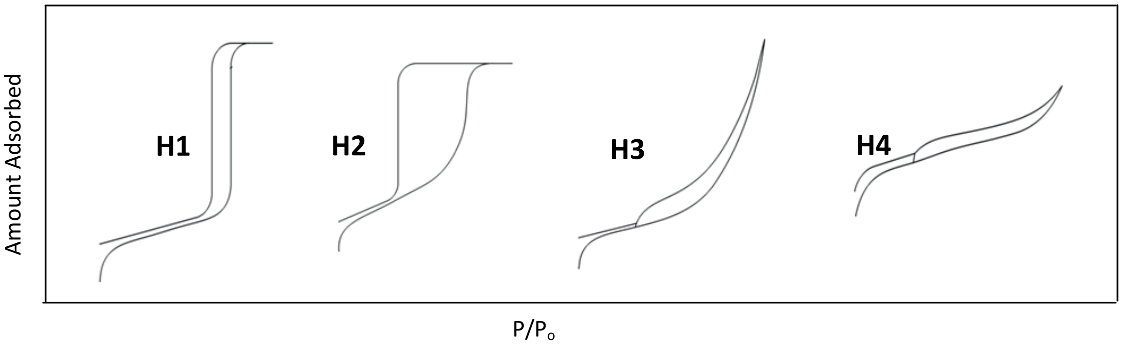

Figure 2.3: Different types of hysteresis [2].

The H4 hysteresis results from adsorbents with slit-like pores in the micropore range. In this dissertation, the produced silica-doped aluminas are type IV isotherms with an H3 hysteresis loop.

2.2.3 Surface area

Numerous studies have been done to develop mathematical expressions from postulated adsorption mechanisms to fit the various experimental isotherm curves. The isotherm equations which are most frequently used are Langmuir [4] and Brunauer, Emmett and Teller (BET) [5]. The Langmuir adsorption isotherm is based on the characteristic assumptions that only monomolecular adsorption takes place, surface is uniform, and there are no interactions among adsorbed molecules. Therefore, this equation is not applicable for mesoporous materials with type IV isotherm involving multilayer adsorption and capillary condensation. The theory of Brunauer, Emmett, and Teller is an extension of the Langmuir treatment to allow multilayer adsorption on nonporous solid surfaces with the following hypotheses: (1) Gas molecules are physically adsorbed on a solid in layers infinitely. (2) There is no interaction between each adsorption layer. (3) The Langmuir theory can be applied to each layer. Therefore, in order to determine the monolayer coverage and the surface area of an adsorbent, the BET theory is often used to model physical adsorption. Based on these assumptions, the BET equation can be derived as:

$$\frac{n}{n_m} = \frac{CX}{((1-X)(1-X+CX))} \tag{2.1}$$

n: mole of gas adsorbed at the equilibrium pressure P.

n_m: mole of gas required to provide a complete monolayer.

X: relative pressure (P/P_0), where P is the measured pressure and P_0 is the saturation pressure.

in which, $C = C_0 \exp[\frac{(\triangle H_{a1} - \triangle H_c)}{RT}]$, where $\triangle H_{a1}$ is heat of adsorption on the first layer, $\triangle H_c$ is heat of condensation of gas, and C_0 is a combination of pre-exponentials for condensation to and evaporation from the first and second layers, respectively [6]. To calculate the surface area Eq. 2.1 can be written as:

$$\frac{P}{n(P_0 - P)} = \frac{1}{(n_m C)} \frac{P}{P_0} \tag{2.2}$$

The BET equation as shown in Eq. 2.2 requires a linear plot of $\frac{P}{n(P_0-P)}$ against $\frac{P}{P_0}$ where the slope and intercept can be used to obtain n_m and C. As a result, the total surface area S can be derived as:

$$S = n_m L \sigma \tag{2.3}$$

L: Avogadro number (6.023×10^{23})

σ: Adsorbate cross sectional area (0.162 nm for nitrogen)

Specific surface area (S^*) is then determined based on Eq. 2.4, where W is the sample weight.

$$S^* = \frac{S}{W} \tag{2.4}$$

2.2.4 Kelvin Equation and pore size

While BET theory provides a method to calculate the surface area, other approaches have been developed in order to determine the pore volume and pore radius of porous materials. IUPAC has classified pore sizes in three categories: macroporous

(>50 nm), mesoporous (2-50 nm), and microporous (<2 nm) [7–9]. Mesoporous, microporous, and nonporous materials have different adsorption. The main reason for this difference is pore condensation. Pore condensation is a phenomenon in which the gas adsorbed in the pores forms a bulk liquid phase at a pressure less than the saturated vapor pressure of the liquid at that temperature. One of the most common approaches for addressing pore condensation in mesoporous materials is the Kelvin equation (Eq. 2.5). The Kelvin equation was used by Barret, Jonier, and Halenda (BJH method) to calculate the pore width from the pore filling pressure [10].

$$RT \ln \frac{P}{P_0} = -\frac{2\nu(V_L)}{r_m} \tag{2.5}$$

In Eq. 2.5, ν is the surface tension of the liquid phase, V_L is the molar volume of the liquid adsorbate, R is the gas constant, and r_m is the radius of curvature of the meniscus of the pore liquid.

The Kelvin equation is applied to the points on the hysteresis loop of the isotherm, gives the corresponding values of r_m. The r_m is the mean radius of curvature of the meniscus of the capillary condensate. The capillary condensation occurs within a pore, thus, the pore walls are lined with an adsorbed film of thickness t. Consequently, the r_m is considered as an inner core rather than a pore [9, 11], due to the multilayer adsorption. To convert r_m to a measurement of the pore volume, the t and the model of pore structure should be considered. It is assumed that the pores are rigid and have the same shape (cylindrical or slit-like). For the cylinder, the pore radius r_p is the sum of r_m and t. For a slit, the pore width dp is the sum of r_m and $2t$. Therefore in the calculation of pore volume, the pore model meniscus curvature can be either hemispherical for cylinder or hemicylindrical for slit. Total pore volume is derived from the amount of vapor adsorbed at the relative temperature close to unity (assuming pores are filled with liquid adsorbate).

$$V_{liquid} = \frac{P_a V_{ads} V_m}{RT} \tag{2.6}$$

P_a = ambient pressure

V_{ads} = volume of gas desorbed

V_m = molar volume of liquid adsorbate, N_2= 34.7 $(\frac{\mathrm{cm}^3}{\mathrm{mol}})$

T = ambient temperature

V_{liquid} = volume of liquid N_2 in pores

The average pore size can be estimated from the pore volume. Assuming cylindrical pore geometry, the average pore radius r_p can be expressed as Eq. 2.7, where S is the surface area. Other pore geometries may need other appropriate models to measure the pore radius.

$$r_p = \frac{2V_{liquid}}{S} \tag{2.7}$$

The BJH model is not valid to calculate the pore volumes and pore size distributions of a cylindrical and slit pore geometries for mesoporous materials with a relatively large, irregular slit-shaped structure. The silica-doped aluminas introduced in this research have the large, irregular slit-shaped mesopores. Therefore, the pore volumes and pore size distributions were calculated using the improved SPG (slit pore geometry) model [12].

2.3 Nuclear magnetic resonance

2.3.1 Nuclear magnetic resonance applications

Nuclear magnetic resonance spectroscopy is a powerful analytical technique used to characterize organic molecules by identifying carbon-hydrogen frameworks within molecules. ^{1}H NMR is used to determine the type and number of H atoms in a molecule; ^{13}C NMR is used to determine the type of carbon atoms in the molecule. Solid state ^{29}Si and ^{27}Al NMR is also used to determine coordination numbers, bond type, and acidity type for heterogeneous catalysts and other similar materials.

2.3.2 Nuclei and magnetic field

The magnetic properties of atomic nuclei can be described by the spin quantum number I and magnetic moment μ [13, 14]. The spin quantum number of a nucleus is $\frac{1}{2}$ if the proton is assumed to be a spherical object. μ can be expressed in units of the Bohr magneton, and e and m are the charge and mass of a proton, respectively. The nuclear factor is represented as g. Equation 2.8 shows that a nucleus with a spin quantum number of zero has no magnetic moment.

$$\mu = g\frac{eh}{2mc}I \tag{2.8}$$

The rules for determining the net spin of a nucleus are as follows:

1. If the mass number (A) of a nucleus is odd, the nuclear spin (I) will be a half-integer (^{1}H, ^{13}C, and ^{15}N).
2. If the mass (A) and the charge (Z) numbers are both even, the nucleus will have spin quantum number of zero (^{12}C, ^{16}O, and ^{32}S).

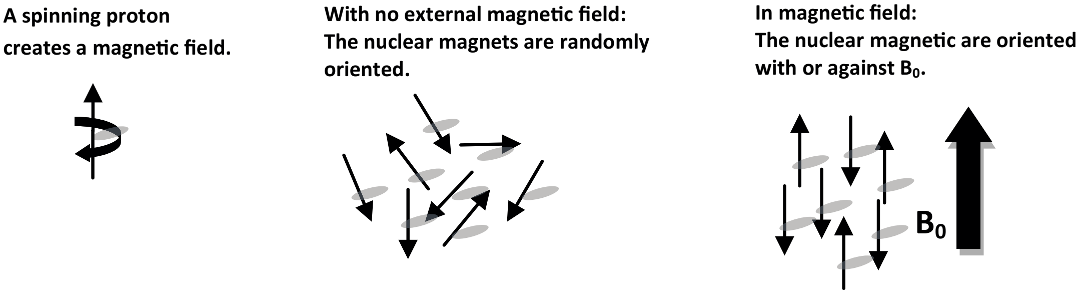

Figure 2.4: Spin orientation in the presence of magnetic field [14].

3. If the mass number (A) is even and the charge number (Z) is odd, the nuclear spin has an integral value (^{14}N).

The $\frac{\mu}{Ih}$ ratio or magnetogyric ratio (ν) describes the magnetic properties of a particular nucleus. Therefore Eq. 2.8 can be written as $\mu = h\nu$. In an applied magnetic field (B_0) a nucleus with a spin quantum number of $\frac{1}{2}$ can align itself either with ($I = +\frac{1}{2}$) or against ($I = -\frac{1}{2}$) the applied field (Fig. 2.4).

The applied magnetic field B_0 will produce an angular acceleration, causing the nucleus to process in the direction of the magnetic field (Newton's law) as shown in Fig. 2.5. Processional frequency ω_0 of aligned nuclei is shown in Eq. 2.9 which is called the Lamor frequency. This frequency is in the radiofrequency range.

$$\omega_0 = \nu B_0 \tag{2.9}$$

2.3.3 NMR theory

The number of possible alignments of a magnetically active nucleus, when placed into a magnetic field is $2I+1$. This energy splitting is called Zeeman splitting. The transition between Zeeman levels is the basis of NMR analysis. In order to

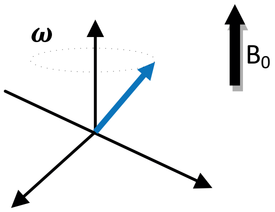

Figure 2.5: Precession of a spinning nucleus in a magnetic field.

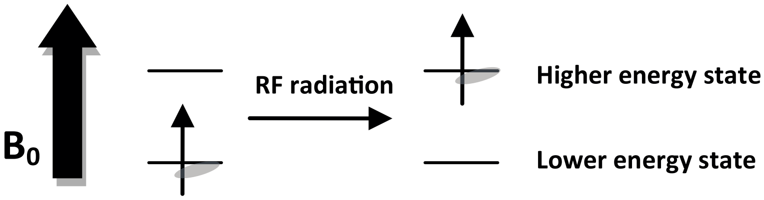

Figure 2.6: Adsorbing RF radiation causes the nucleus to spin flip [14].

make these transitions, a series of radio frequencies (RF) are applied to the nuclei in a magnetic field. The magnetic component of the RF acts perpendicular to B_0, which is causing the nuclear alignments. When the applied RF is similar to ω_0, a transition between nuclear spin states occurs. The applied RF changes the strength and direction of the magnetic field, causing the magnetic moments to flip to a higher energy state (see Fig. 2.6) and precess around the new field and align against the magnetic field. When applied RF is relaxed, the excited nuclear spin state decays to a more stable ground state configuration (aligned with the magnetic field) and re-emits RF radiation at the excitation frequency [15]. The decaying current can be Fourier transformed into the frequency domain to reveal the resonance frequencies of the nuclei.

Samples with large numbers of nuclei are subject to a secondary magnetic field generated by its own surrounding electrons and also a diamagnetic moment produced from nearby atoms and molecules. Thus, the secondary magnetic field shields the nucleus from applied magnetic field and changes the energy level and resonance frequency of the nucleus. This shifting is called a chemical shift which reveals the chemical environment around the nucleus. The less shielded the nucleus becomes, the more the applied magnetic field (B_0) is felt (e.g. protons near electronegative atoms are more deshielded, so they absorb downfield). In addition, nuclear magnetic moments in the sample can interact with each other. Dipole-dipole coupling decreases when intermolecular distance (r) increases. Nuclei with a spin larger than $\frac{1}{2}$ are called quadrupole spins. These are sensitive to the electric field generated by their surroundings. The coupling of the nuclear electric quadrupole moment with gradient electric field is called the quadrupole interaction. This interaction affects the nuclear spin energy levels in addition to the other magnetic interactions shown in Fig. 2.7.

J coupling constant is also observed from the spin-spin interaction of two neighboring nuclei. This causes splitting in the peak. The number and relative intensities of the multiplet components depend on the various orientations of the interacting nuclear spin. Generally, the line frequency splits into a multiplet of $2nI+1$ components, where n is the number of magnetically equivalent spin I nuclei.

2.3.4 Solution and solid samples

When NMR analysis is used for a liquid solution, first, local vibrations in the magnetic field become short-lived since neighboring dipoles orient easily. The reorientation process reduces the field band broadening and lines become narrow (0.01 Hz for a proton). Second, the transmission of magnetic information from nucleus to nucleus occurs by slight polarization of the spin motions of the molecule itself and results in adding another dimension to NMR spectroscopy (HSQC, COSY). When NMR is used in the solid state, the orientations of the nuclei are fixed. Thus,

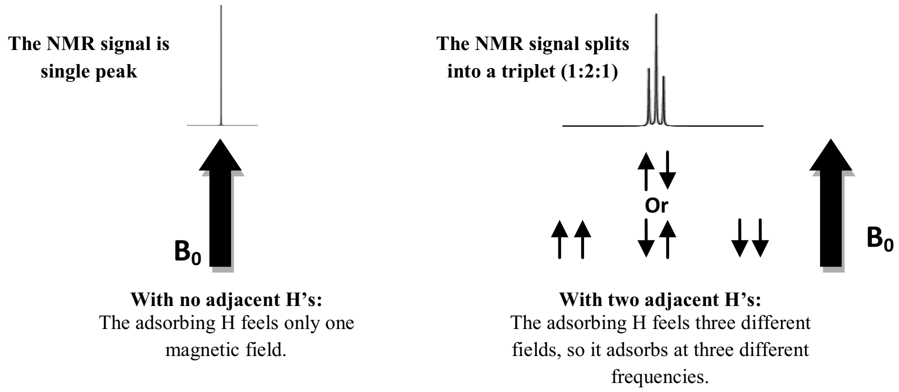

Figure 2.7: Nuclear spin energy levels [14]

nuclei will resonate over a wide frequency range and generate line broadening (400 ppm for ^{13}C). The magic angle technique is used to average various solid state interactions and is therefore considered a line narrowing technique for NMR spectra.

The chemical shift of the nucleus depends on a molecule orientation in the applied magnetic field [14] (nuclei aligned with the magnetic field experience a greater magnetic field effect than nuclei situated at right angles to the applied magnetic field). In a solid sample, the molecule's will align themselves in all angles. Thus, the chemical shifts of the nuclei are spread over a wide range. The width of this spread is called chemical shift anisotropy (CSA). The chemical shift of a nuclide in a solid sample is the chemical shift of the nucleus when the system is parallel to the magnetic field minus the chemical shift when it is at a right angle to the magnetic field. The anisotropic part of chemical shift is: $\frac{1}{3}[CSA][3\cos\theta - 1]$, where θ is the angle of the molecule with the applied field. When θ=54.7^o and sample spinning is larger than CSA (Fig. 2.8), the anisotropic contribution to the chemical shift is zero,

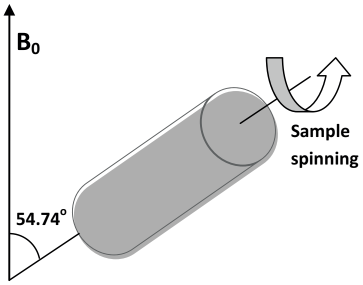

Figure 2.8: Magic angle spinning.

which reduces the spectra to narrow lines. However, when high spinning rates are not possible, a pulse sequence will help removing anisotropic. For example, anisotropy cannot be removed by fast spinning for nuclei with $I > \frac{1}{2}$ and $+\frac{1}{2}$ to $-\frac{1}{2}$ transitions that are affected by quadrupolar effects, such as aluminum. Spinning quadrupolar nuclei produces spinning side-bands that radiate out from the isotropic chemical shift line. The magnetic angle method can narrow the side bands and ^{27}Al chemical shifts can be observed based on aluminum coordination numbers.

The concentration of each Al in different environments can also be calculated from the peak areas. Therefore, magic-angle spinning is a great tool to overcome poorly resolved solid sample spectra, get information on the number of unique nuclear environments (e.g, concentration), and reveal the number and type of nearest neighbors [16].

2.4 Transmission electron microscopy

2.4.1 Transmission electron microscopy applications

Electron microscopy uses a focused beam of high energy electrons that have characteristic wavelength of less than 1 Å based on de Broglie wavelength [17]. Thus, it allows detailed micro-structural examination through high-resolution and high-magnification imaging. It reveals the size and morphology of particles, chemical composition of materials and also enables the investigation of crystal structures. Crystal structure can be identified by measuring the d-spacing of the crystal planes. In this thesis TEM imaging is used to determine the size and morphology of catalyst support nanoparticles.

2.4.2 TEM system

A transmission electron microscope consists of different parts as below (diagramed in Fig. 2.9 [13]):

1. The electron gun generates an intense beam of high energy electrons. The source of electrons is a tungsten filament or lanthanum hexaboride.
2. The electron column is filled with a set of electromagnetic lenses and a set of apertures that can be moved in and out of the beam path. Apertures consist of a strip of molybdenum containing a sequence of different sized holes that allow modulation of the beam to different degrees of precision. Electromagnetic lenses can shape the electron beam which travels in a spiral trajectory.
3. The detector is usually the x-ray energy dispersive spectroscopy (EDS or EDX) system that is located near the sample.
4. The sample is loaded in the specimen. The sample must be very thin (1-100 nm) to transmit a detectable portion of the electron beam.
5. The image is projected onto the screen in the viewing chamber. The screen in the chamber is only used for producing a temporary image. To collect a permanent image, a CCD camera is inserted into the path of the beam. This allows the image to be collected in a digital form.

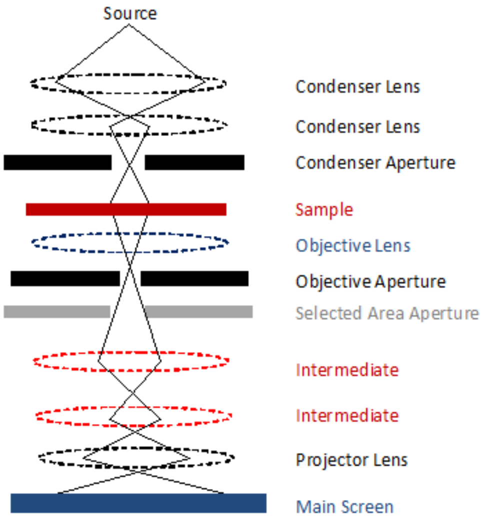

Figure 2.9: Diagram of a transmission electron microscope [17].

Typical operating conditions of a TEM instrument are 100-200 keV electrons, 10^{-6} mbar vacuum, 0.5 nm resolution and a magnification of 3×10^5 to 10^6. By applying voltage, the electrons are emitted from the emitter (W or LaB_6) and accelerated into the vacuum. Condenser lenses control illumination of the specimen (they align the beam and control the current, density, size and focal point of the beam). Objective lenses focus the beam (passed through the specimen). Projector lenses magnify the image onto a final imaging screen. Finally, images can be collected using direct exposure or a digital CCD camera coupled to a fluorescent screen.

2.4.3 TEM contrast information

Changes in the lens strength or deactivation lenses allow for many operating modes in the TEM instrument to observe different imaging. Some examples are listed below:

Bright field image: In bright field mode, the scattered/diffracted electrons are blocked with an objective aperture (Fig. 2.10a). A primary electron beam of high energy and intensity passes through a condenser to produce parallel rays that hit the sample. The attenuation of the beam depends on the density and the thickness of the sample. The transmitted electrons form a two-dimensional projection of the sample mass, which is subsequently magnified by the electron optics to produce a bright field image. Regions with no sample will appear bright and regions with higher atomic number (thicker) will appear dark. This method is used mostly to characterize nanoparticles.

Dark field image: In dark field mode, the electron beam is blocked, then the scattered and diffracted electrons pass through the objective lens. Regions with no sample will appear dark whereas regions with higher atomic number will appear bright (strongly scatter/diffract electrons) as shown in Fig. 2.10b. Dark field is limited since it may cause damage to the sample due to high intensity illumination. This method is used to examine polymers and bimolecules.

Selected area electron diffraction (SAD): Diffraction patterns can be obtained by placing the aperture in the back of the focal plane of the lens and a desired Bragg reflection can be selected (Fig. 2.10c). The holes in the aperture allow a small fraction of the beam to pass through the sample. For thin crystalline samples, this produces an image that consists of a pattern of dots in the case of a single crystal, or a series of rings in the case of a polycrystalline and amorphous material (similar to XRD pattern). This pattern provides the investigator with information about the crystal structure and lattice parameter. However, X-ray diffraction experiments are still more convenient and optimized for obtaining accurate crystallographic parameters.

Electron energy loss spectroscopy (EELS): EELS allow for the selection of particular energies which can be associated with the way the electron has interacted with the sample. For example, different elements in a sample result in different electron energies in the beam due to inelastic scattering and energy lost, which is measured by an electron spectrometer (Fig. 2.11). The change in energy is not random but is directly related the inelastic collision of beams with specific electron of orbital shell. The data can be used to provide information on chemical composition and chemical bonds (Fig. 2.12), based upon the atomic transitions during electron-electron interaction. EELS is efficient for atoms with low atomic numbers.

2.5 X-ray diffraction

2.5.1 X-ray diffraction applications

Powder X-ray diffraction (XRD) can be used for qualitative and quantitative analysis. It is one of the oldest and most frequently applied techniques in catalyst and catalyst support characterization. It is used to identify crystalline phases by means of lattice structural parameters (such as d spacing), and to obtain particle size and shape. Powder XRD method is fast, non-destructive and can be done in-situ.

Crystal structures have planes made by repetitive arrangements of atoms (Fig. 2.13a), which are capable of diffracting X-rays (Fig. 2.13b). X-rays are electromagnetic radiation with wavelengths between 0.01 Å and 100 Å. Because the distance between atoms and atomic planes in a crystal is $\sim$1-100 Å, crystals diffract X-rays. The angles of diffraction differ for the various planes within the crystal. Thus, every compound or element has its own somewhat unique diffraction pattern. Comparing the patterns allows differentiation of various structures.

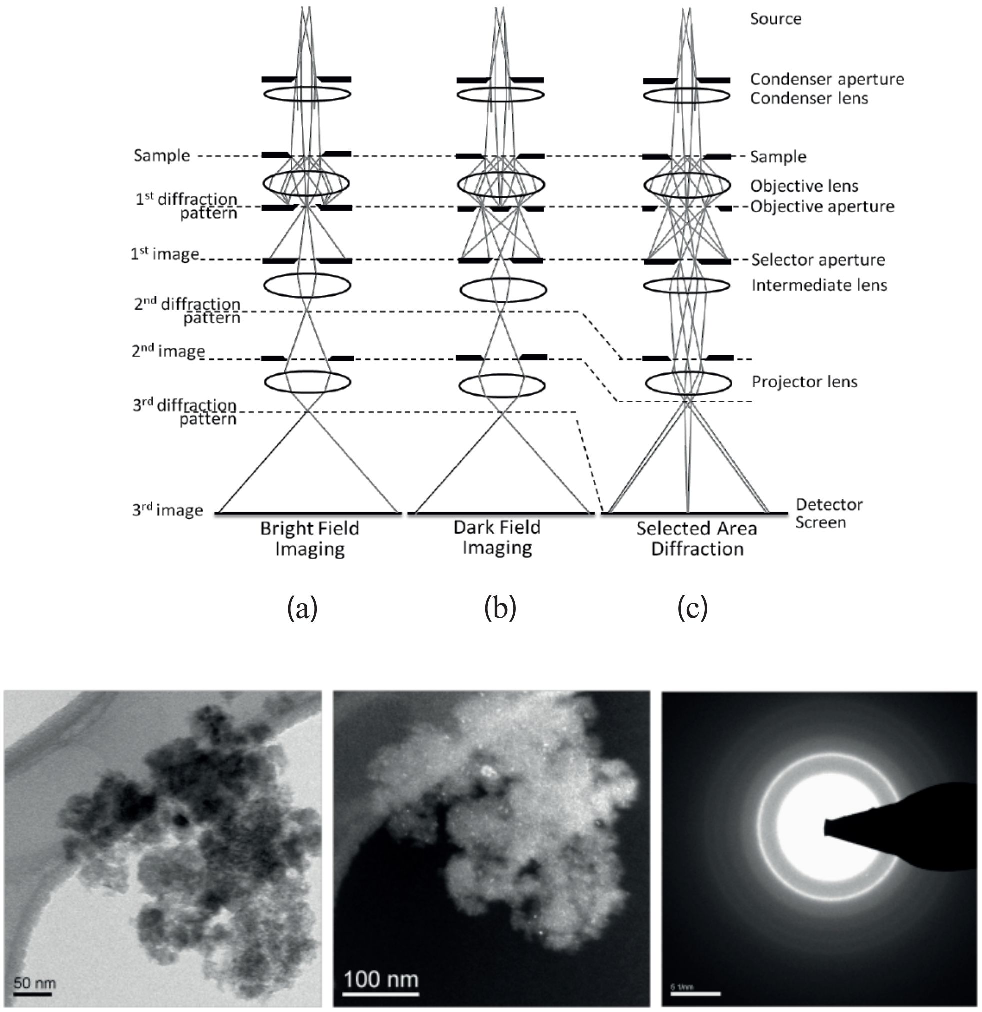

(a) (b) (c)

(d) (e) (f)

Figure 2.10: Ray diagrams of TEM imaging for the (a) bright field, (b) dark field, (c) selected area electron diffraction modes adapted from Reimer [17], (d) bright field, (e) dark field, and (f) diffraction images of Pt/La$-$Al$_2$O$_3$ nanoparticles [18].

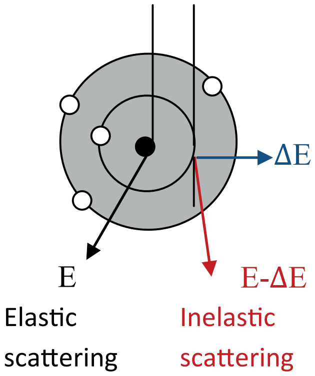

Figure 2.11: The energy of an inelastically scattered electron is always less than that of the primary electron [17].

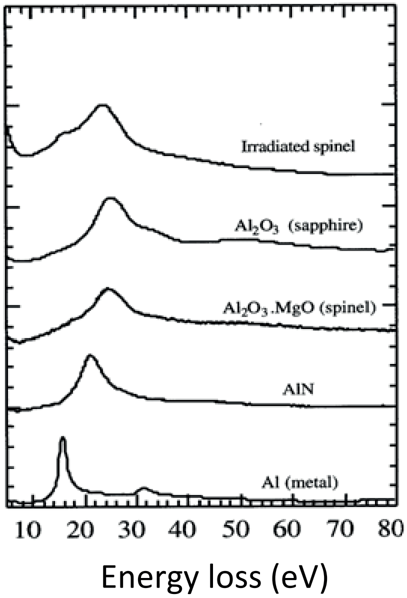

Figure 2.12: The low-loss peaks of the Al atoms in different environments. The differences in the spectra are due to differences in bonding [13].

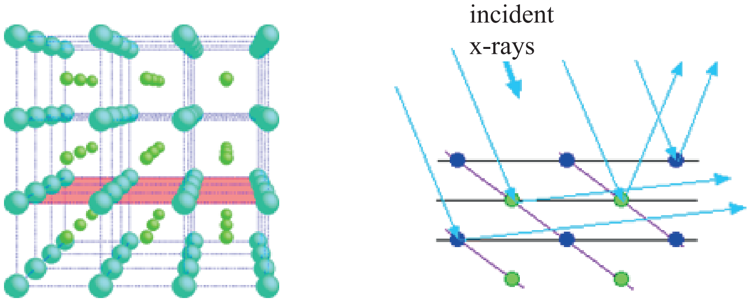

(a) (b)

Figure 2.13: (a) Face centered cubic structure, (b) X-ray diffractions

2.5.2 Bragg equation

The Bragg equation describes the scattering phenomenon on a crystal lattice. Consider an incident beam that is reflected by planes. The path difference between neighboring planes causes a phase difference between the diffracted beams, so the reflected radiation shows constructive and destructive interference. The Bragg equation (Eq. 2.10) predicts that constructive interference only occurs if the ratio between the phase difference and wavelength is an integer value of n (Fig. 2.14).

$$n\lambda = 2dsin\theta \tag{2.10}$$

d: lattice spacing, the shortest distance between two neighboring net planes.

n: 1, 2, 3, . . .

λ: in elastic scattering, the incident and reflected beam have same wavelength.

θ: the angle between the incident or the reflected beam and the net plane. If one measures the angles, 2θ , under which constructively interfering X-rays

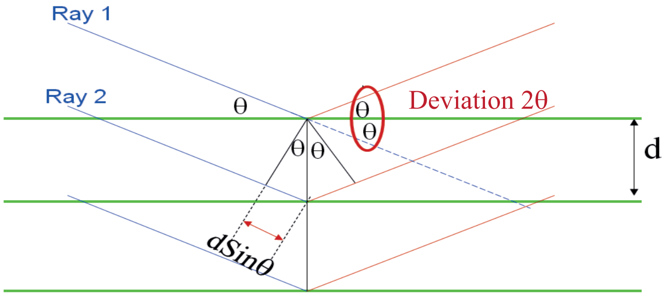

Figure 2.14: X-rays scattered by atoms in an ordered lattice interfere constructively in directions given by Bragg's law [19].

leave the crystal, the Bragg relation (Eq. 2.10) gives the corresponding lattice spacings that are characteristic for a particular compound.

2.5.3 Reciprocal lattice and Ewald sphere

The Bragg equation permits a visual understanding of experimental diffraction effects and the prediction of diffraction geometries. However, the most useful method to explain diffraction phenomena was developed by Ewald [19] and has a rather formidable name "reciprocal lattice".

The orientation relative to the lattice is defined by Miller indices with the values hkl. The d_{hkl} is defined as the perpendicular distance from a unit cell to the first plane in the family (hkl). Figure 2.15a shows unit cell planes as d_{hkl} vectors. It is clear that density of points representing planes, increases to infinity as the origin is approached. The full three dimensional vector representations of the planes in a unit cell will be a sheaf of vectors projecting out of the sphere in all directions. Figure 2.15a shows that the vectors are approaching the origin according to the reciprocals

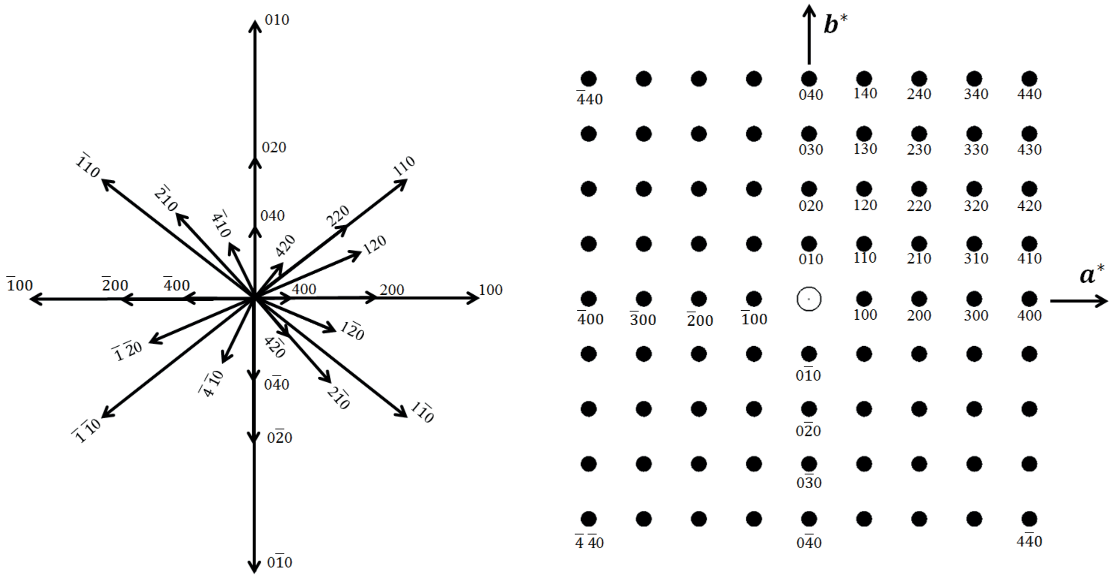

(a) (b)

Figure 2.15: (a) Representation of unit cell planes as d_{hkl} vectors, (b) The reciprocal lattice [19]

of d_{hkl}. Ewald proposed plotting the reciprocal of d vectors (Eq. 2.11) instead of d (Fig. 2.15b).

$$(d_{hkl})^* = \frac{1}{d_{hkl}} \tag{2.11}$$

It is evident that the reciprocal lattice is a useful construction for demonstrating the lattice planes. The points in this space repeat at periodic intervals is called reciprocal lattice. a^*, b^*, c^*, d^* are also reciprocal vectors.

Figure 2.16 shows an imaginary sphere (Eward Sphere) with a radius of $\frac{1}{\lambda}$ around a real crystal. The Eward sphere has all of the components that are needed to visualize the diffraction process geometrically, instead of mathematically using the Bragg equation.

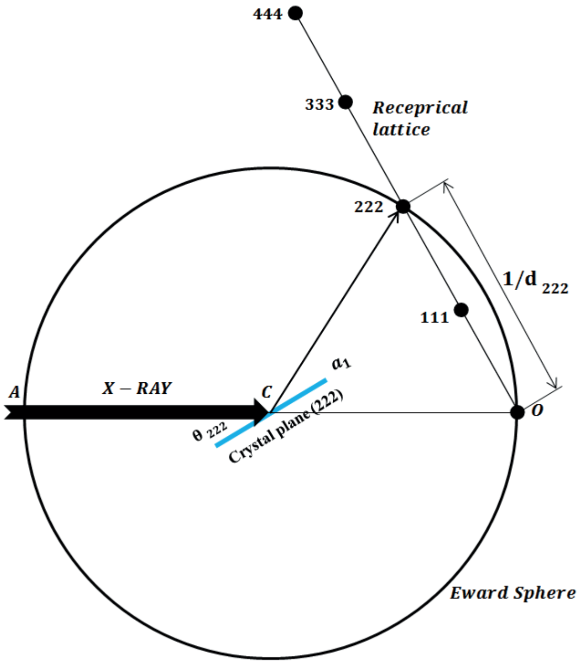

Figure 2.16: Ewald sphere [19].

It is clear that a rotation of the crystal will also rotate the reciprocal lattice because the reciprocal lattice is defined in term of the real-space lattice (Fig. 2.17a-c). When the crystal is rotated and reciprocal d vectors touch the Eward sphere, the condition for diffraction is met and constructive interference occurs. The diffracted beam emerges in the direction connecting the center of the sphere to the reciprocal lattice point in contact with the sphere. A detector placed tangent to the sphere at that point in real space will record an intensity of this specific diffracted beam.

2.5.4 Diffraction pattern

Two points should be considered to understand the diffraction pattern: (1) The d^*_{hkl} vector is associated with each point in reciprocal lattice with its origin on

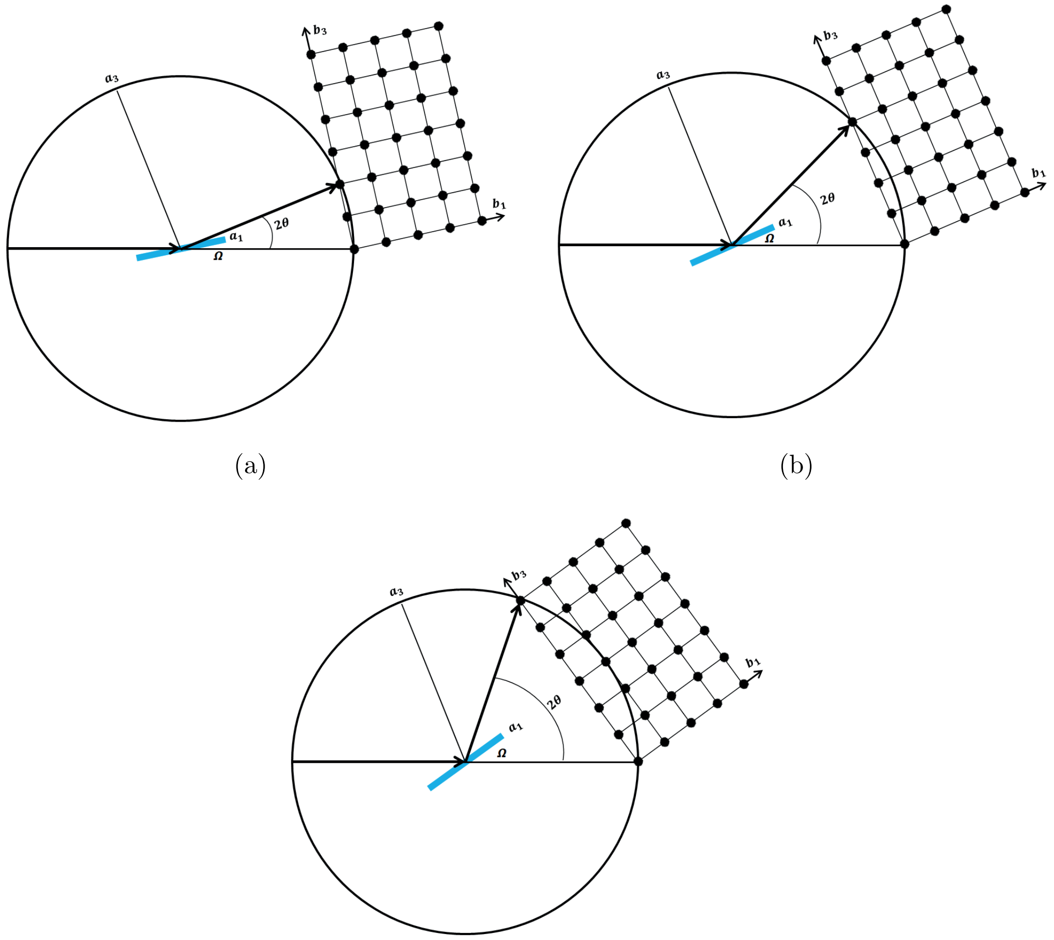

(a) (b)

(c)

Figure 2.17: Examples for the Ewald construction for the X-ray diffraction scan.

the Ewald sphere, and (2) each crystallite located in the Ewald sphere has reciprocal lattice with an orientation determined by the orientation of the crystal. Figure 2.18 shows that a concentric cone is formed when d^*_{hkl} vectors touch the Ewald sphere in all direction. Therefore, each point in the reciprocal lattice produces a cone of diffraction as the Bragg angle; the cones produce circles as shown in Fig. 2.19a and

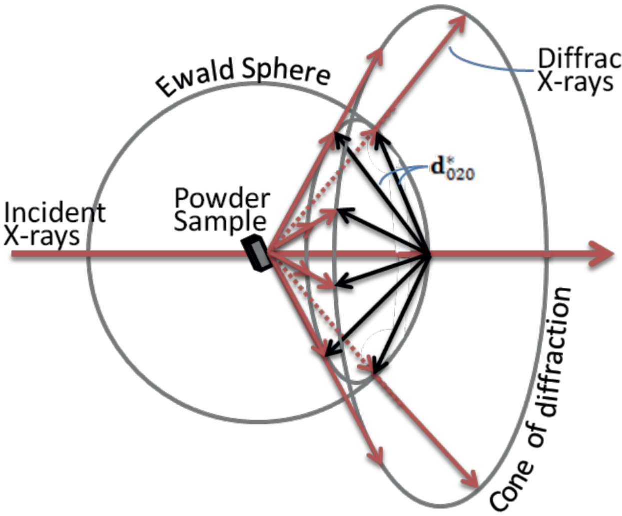

Figure 2.18: The intersection of d^*_{hkl} vectors from a sample powder with Ewald sphere [19].

b; Each circle in the pattern corresponds to diffraction from planes, and their d_{hkl} is calculated from the Bragg equation (Eq. 2.10) where wavelength is always known for experiment.

Diffractograms (Fig. 2.19c) are measured as a function of the angle 2θ. When the sample is a crystalline powder, the diffraction pattern is formed by a small fraction of the particles only. Rotation of the sample during measurement enhances the number of particles that contribute to diffraction.

The width (or rather the shape) of diffraction peaks carries information on the dimensions of the reflecting planes. Diffraction lines from perfect crystals are very narrow, for crystallite sizes below 100 nm, however, line broadening occurs due to incomplete destructive interference in scattering directions where the X-rays are out of phase. The Scherrer formula relates crystal size to line width (Eq. 2.12) to calculate particle size [21]. The λ is the X-ray wavelength, β is the peak width, θ is

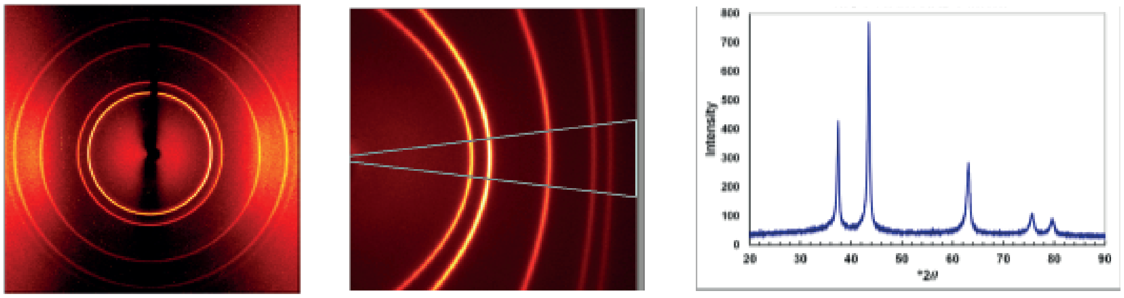

(a) (b) (c)

Figure 2.19: Powder XRD of 24 nm NiO: (a) Powder XRD ring pattern, (b) Integrated slice of the ring, (c) Powder 2D pattern [20].

the angle between the beam and the normal to the reflecting plane, K is a constant (often taken as one), and d is average crystallite diameter.

$$d = \frac{K\lambda}{\beta \cos\theta} \tag{2.12}$$

Bibliography

[1] C. H. Bartholomew and R. J. Farrauto, *Fundamentals of industrial catalytic processes*, 2nd ed. Wiley-AICHE, 2006. xii, 2, 41, 42, 81, 82, 126, 137

[2] F. Rouquerol, J. Rouquerol, and K. Sing, *Adsorption by Powders and Porous Solids: Principles, Methodology and Applications*, 1999. xiv, 41, 43

[3] J. Rouquerol, D. Avnir, C. W. Fairbridge, D. H. Everett, J. H. Haynes, N. Pernicone, J. D. F. Ramsay, K. S. W. Sing, and K. K. Unger, "Recommendations for the characterization of porous solids," *Pure Appl. Chem.*, vol. 66, no. 8, pp. 1739–58, 1994. 41

[4] I. Langmuir, "Constitution and fundamental properties of solids and liquids. ii. liquids," *J. Am. Chem. Soc.*, vol. 39, pp. 1848–1906, 1917. 44

[5] S. Brunauer, P. H. Emmett, and E. Teller, "Adsorption of gases in multimolecular layers," *J. Am. Chem. Soc.*, vol. 60, pp. 309–19, 1938. 44

[6] F. Salvador, C. Sanchez-Jimenez, M. J. Sanchez-Montero, and A. Salvador, "A review of the application of the BET equation to experimental data. the c parameter," *Stud. Surf. Sci. Catal.*, vol. 144, no. Characterization of Porous Solids VI, pp. 379–386, 2002. 45

[7] K. S. W. Sing, "Adsorption methods for the characterization of porous materials," *Adv. Colloid Interface Sci.*, vol. 76-77, pp. 3–11, 1998. 46

[8] M. M. Dubinin, “Porous structure and adsorption properties of active carbons,” *Chem. Phys. Carbon*, vol. 2, pp. 51–120, 1966. 46

[9] S. J. Gregg and K. S. W. Sing, *Adsorption, Surface Area and Porosity. 2nd Ed*, 1982. 46

[10] E. P. Barrett, L. G. Joyner, and P. P. Halenda, “The determination of pore volume and area distributions in porous substances: Computations from nitrogen isotherms,” *J. Am. Chem. Soc.*, vol. 73, pp. 373–80, 1951. 46

[11] S. J. Gregg, “Adsorption of gases - tool for the study of the texture of solids,” *Stud. Surf. Sci. Catal.*, vol. 10, no. Adsorpt. Gas-Solid Liq.-Solid Interface, pp. 153–64, 1982. 46

[12] B. Huang, C. H. Bartholomew, and B. F. Woodfield, “Improved calculations of pore size distribution for relatively large, irregular slit-shaped mesopore structure,” *Microporous and mesoporous materials*, 2013. 47

[13] D. B. Williams and C. B. Carter, *Transmission electron microscopy: a text book for material science*, 2nd ed. New york: Springer, 2009. xv, 48, 54, 59

[14] M. J. Duer. Malden, MA,: Blackwell Science, 2002, p. 563. xiv, xv, 48, 49, 50, 52

[15] W. W. Paudler, *Nuclear magnetic resonance: General concepts and applications.* NY: John Wiley and Sons, 1987. 50

[16] B. Imelik and J. C. Vadrine, *Catalyst characterization: physical techniques for solid materials.* Plenum press, 1994. 53

[17] L. Reimer and H. Kohl, *Transmission electron microscopy: Physics of image formation and microanalysis*, 5th ed. New York: Springer science, 2008, vol. 36. xv, 53, 55, 58, 59

[18] B. Huang, "Facile synthesis and improved pore structure characterization of mesoporous γ-Al_2O_3 catalyst supports with tunable pore size," Thesis, 2013. xv, 58

[19] R. Jenkins and R. L. Snyder, *Introduction to X-ray powder diffraction.* New york: John Wiley and sons, INC., 1996. xv, 61, 62, 63, 65

[20] S. T. Smith, "The synthesis and structural characterization of metal oxide nanoparticles having catalytic applications," Thesis, 2012. xv, 66

[21] A. L. Patterson, "The Scherrer formula for X-ray particle-size determination," *Physical Review*, vol. 56, pp. 978–982, 1939. 65, 74, 78, 153, 163, 166

Chapter 3

The origin of increased thermal stability for silica-Doped alumina

3.1 Introduction

Gamma Alumina ($\gamma-\mathrm{Al_2O_3}$) is the most widely used commercial catalyst support because of its moderately high surface area, meso- and macro-porosity and relatively high thermal and hydrothermal stabilities. It is an effective catalyst support for both base and noble metals in many different applications (e.g., Pt, Pd catalytic converters [1], Ni catalyst in hydrogenation [2], Co(Ni)-Mo(W) sulfide catalysts for hydrotreating of petroleum feedstocks [3], and Co catalyst for Fischer-Tropsch synthesis (FTS) [4,5]). Since each of these applications typically requires a unique range of surface area, pore volume and pore diameter, commercial aluminas are supplied with a wide range of surface areas and porosities [6–8]. Thus, ability to optimize pore size, pore volume and surface area$\gamma-\mathrm{Al_2O_3}$ is essential in the manufacture of these materials [4,9–11].

While $\gamma-\mathrm{Al_2O_3}$ is stable during long term use at $500-600$°C, at higher reaction temperatures ($650-1200$°C) and especially in the presence of water vapor, the porous structure collapses due to sintering and structural transformations to other forms of alumina ($\alpha-\mathrm{Al_2O_3}$), resulting in lower porosity of the supports, and in some cases, deactivation of the catalyst. Thus, in a number of catalytic reactions taking place at elevated temperatures and high steam concentrations, (e.g., auto emissions control and steam reforming [12–17]) the thermal and hydrothermal stability of $\gamma{-}Al_2O_3$ is inadequate. Nevertheless, $\gamma{-}Al_2O_3$ can be stabilized against sintering and phase transformations through the incorporation of suitable dopants (i.e., alkaline earth oxides, transition, and rare-earth elements, as well as SiO_2).Previous studies have demonstrated that thermal and hydrothermal stabilities of alumina are substantially improved by the addition of 1 to 20 wt.% silica [15–21], titania [22,23], zirconia [19,24,25], and rare earth elements such as lanthanum [1,13,26], and cerium [12, 27, 28].

Of particular pertinence to the present study is the use of silica at 1 to 10 wt.% as a stabilizer for $\gamma{-}Al_2O_3$. A number of previous papers and patents address the preparation of stable silica-doped alumina. In an early patent, a multi-step co-gel preparation method was reported to produce silica-alumina with high porosity: the alumina sample contained 7% silica, with a surface area of 150 m^2/g, and a pore volume of 0.9 cm^3/g at 1100°C (no pore diameter was reported) [29]. This method involves the reaction of an alkali metal aluminate and silicate, followed by filtration, washing, and drying. Preparation of silica-modified-alumina with 2 to 10% silica using a different co-gel method has also been reported [30]: after calcination at 648°C, the 5% silica sample was reported to have a moderately high surface area of 318 m^2/g and relatively low pore volume of 0.46 cm^3/g. This method uses acid in the sol preparation and base in the gelation step. Wan [31] reported a stabilized 5.5% silica-alumina support produced by impregnating alumina with polyorgano silane; after calcination at 1100°C and 1200°C, the surface area was 158.2 m^2/g and 93 m^2/g, respectively; however, neither pore volume and nor pore diameter data were reported. Other complex methods involving solvents and pH adjustment techniques have also been used to make stable silica-doped alumina [12, 16, 18, 32]. However, these particular supports do not maintain high surface areas and pore volumes at higher temperatures. For example, Shutilov et al. [16] used an impregnation method to make a stable silica-doped alumina but reported low values for both surface area (68 m^2/g) and pore volume (0.34 cm^3/g) and a moderately large pore diameter (15 nm) at 1100°C. Silica-doped aluminas having high surface area and pore volume at high temperatures have also been synthesized using aerogel and crygol methods, but they are costly and time consuming [15,17,20]. For example, Miller [15] produced a stable silica-doped alumina containing 10% silica by the multi-step aerogel method and using supercritical drying to remove the solvent. At 1200°C, it has a surface area of 150 m^2/g and pore volume of 0.65 cm^3/g, which are unusually high for this temperature; no pore diameter data were available. Horiuchi et al. [17] used supercritical drying to synthesize silica-doped alumina with a surface area of 110 m^2/g, pore volume of 0.9 cm^3/g and pore diameter of 18.6 nm at 1200°C.

From this previous work, it is evident that the addition of silica to alumina produces alumina support materials with substantially higher porosity at high temperatures (relative to pure alumina). Such materials having thermal and hydrothermal stabilities facilitate higher catalyst loadings and increase catalyst lifetime, activity, and productivity at high operating temperatures [5]. However, most of the previous preparation methods involve complex, multi-step procedures and hence higher manufacturing costs. Therefore, it would be desirable to devise simple, low-cost methods that produce such materials.

In this chapter, I report a simple, one-pot, solvent-deficient preparation method for silica-doped $\gamma-Al_2O_3$ supports with high surface area, large pore volume, uniquely large pores having a bimodal distribution, and high thermal stability. The results indicate that in 5% SDA, Si ions are incorporated into vacant tetrahedral sites of the alumina spinel and stabilize the structure to high temperatures.

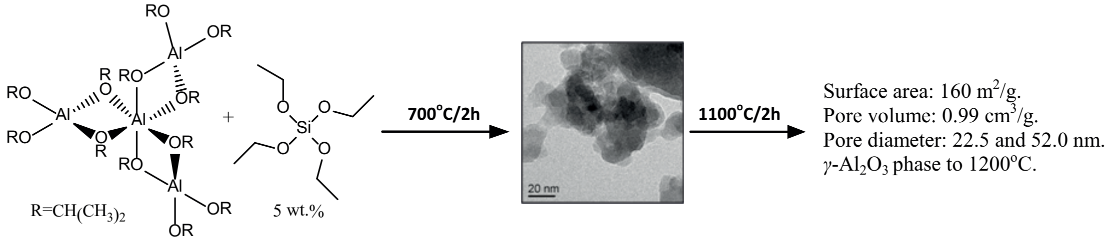

Surface area: 160 m^2/g.
Pore volume: 0.99 cm^3/g.
Pore diameter: 22.5 and 52.0 nm.
γ-Al_2O_3 phase to 1200°C.

Figure 3.1: Synthesis of silica-dopped alumina.

3.2 Experimetnal

3.2.1 Material

Aluminum isopropoxide ($C_9H_{21}O_3Al$) (granular, 98+%) and tetraethyl orthosilicate ($SiC_8H_{20}O_4$) (liquid, 99.9%) (TEOS) were purchased from Alfa-Aeser. Commercial 5% silica-doped alumina (Siral-5) was purchased from Sasol for comparison.

3.2.2 Synthesis method

Silica-doped aluminas (100 g batches) (SDAs) were prepared via a patented method [33] (see Fig. 3.1) that involves mixing aluminum isopropoxide (AIP) and water at a 5:1 mole ratio of water to AIP, then 5 wt.% silica from tetraethyl orthosilicate (TEOS) and water at a 2:1 water to TEOS mole ratio. This precursor was mixed for 30 minutes with a Bosch Universal Mixer (model: MUM6N10UC) followed by a thermal treatment at 700, 900, 1100, 1200°C for 2 h each with 5 h ramps. Samples with 0, 15 and 27 wt.% of silica were prepared for comparison.

3.2.3 Characterization

The alumina phase was identified by powder X-ray diffraction (XRD) using a PANalytical X'Pert Pro diffractometer with a Cu Kα X-ray source ($\lambda = 1.5418$ Å) operated at 45 kV and 40 mA. Scans were performed between 10° and 90° 2θ with a step size of 0.0167° at a rate of $0.013°\text{s}^{-1}$. The Scherrer formula was used to estimate crystallite size [34]. In situ high-temperature XRD (HTXRD) experimentsfTEM were performed using this same instrument equipped with an Anton Paar HTK 1200N stage. Scans were collected using the same parameters just described as the samples were heated in purified air from 400 to 1200°C.

Nitrogen adsorption measurements were carried out using a Micromerictics Tristar 3020 for the determination of surface properties at -196°C. Surface area was calculated using the Brunauner-Emmett-Teller (BET) model in the P/P_0 range from 0.05 to 0.20. Pore volumes were determined at a single point of P/P_0 equal to 0.990. Pore size distributions were calculated using an improved slit pore geometry (SPG) model for large pore sizes [35]. Samples were degassed at 200°C under N_2 flow overnight before every measurement.

Microscopic images of samples were obtained with an FEI Philips Tecani F30 transmission electron microscope (TEM) at a voltage of 200 kV. TEM samples were prepared by placing a drop of silica-doped alumina (1% dispersed in ethanol) on a carbon film with a copper mesh grid (Ted-Pella Inc.).

Thermo-gravimetric (TG) and differential-temperature (DT) analyses were performed using a NETZSCH STA 409PC instrument (NETZSCH, Germany) in the temperature range of 25-1400°C under 20 mL/min He gas flow with a heating rate of 3°/min. A sample weight of 30 mg was used in a platinum pan.

Solid state MAS NMR spectra were obtained on a Bruker Avance I 400 (9.6 T) instrument using a 7 mm (^{29}Si) or a 4 mm (^{27}Al) broadband MAS probe. All spectra were obtained at room temperature, and a spinning speed of 12.5 kHz for ^{27}Al or 4 kHz for ^{29}Si. The 1D ^{29}Si MAS NMR spectra used a single pulse direct polarization (DP) Block decay with a 240 s recycle delay to assure complete relaxation, while the ^{1}H-^{29}Si cross polarization (CP) MAS NMR spectra was obtained using a 5 ms contact time and a 10 s recycle delay. The ^{27}Al MAS spectra were also obtained using a DP Bloch decay, and a $\pi/6$ pulse length. The ^{27}Al chemical shift was referenced to the external secondary standard 1 M $Al(H_2O)_6^+$ $\delta = 0.0$ ppm, and the ^{29}Si chemical shift was referenced to the secondary standard Q_8M_8 $\delta = +12.6$ ppm with respect to neat TMS ($\delta = 0$ ppm). Spectral simulations and deconvolutions were performed using DMFIT [36,37]. The Czejeck distribution [38] of the ^{27}Al electrical field gradient (EFG) tensor was used in the analysis of the ^{27}Al NMR, and gives rise to the asymmetric line shapes. In some instances it was necessary to include multiple distributions for a given Al environment to reproduce the experimental line shape.

3.3 Results

3.3.1 X-ray diffraction

Figure 3.2 shows XRD patterns for pure alumina and three silica-doped alumina samples after calcination at 700, 900, 1100 and 1200°C. Only characteristic broad peaks for γ-Al_2O_3 at 45.7° and 66.6° are observed at 700-900°C for all samples; the broad lines indicate that samples are largely amorphous and consist of small crystallites of small diameter. For the pure alumina sample only α-Al_2O_3 is observed at 1200°C (Fig. 3.2a). In contrast, mostly the γ-Al_2O_3 phase is observed for 5, 15, 27% silica samples, respectively (Fig. 3.2b,c,d).

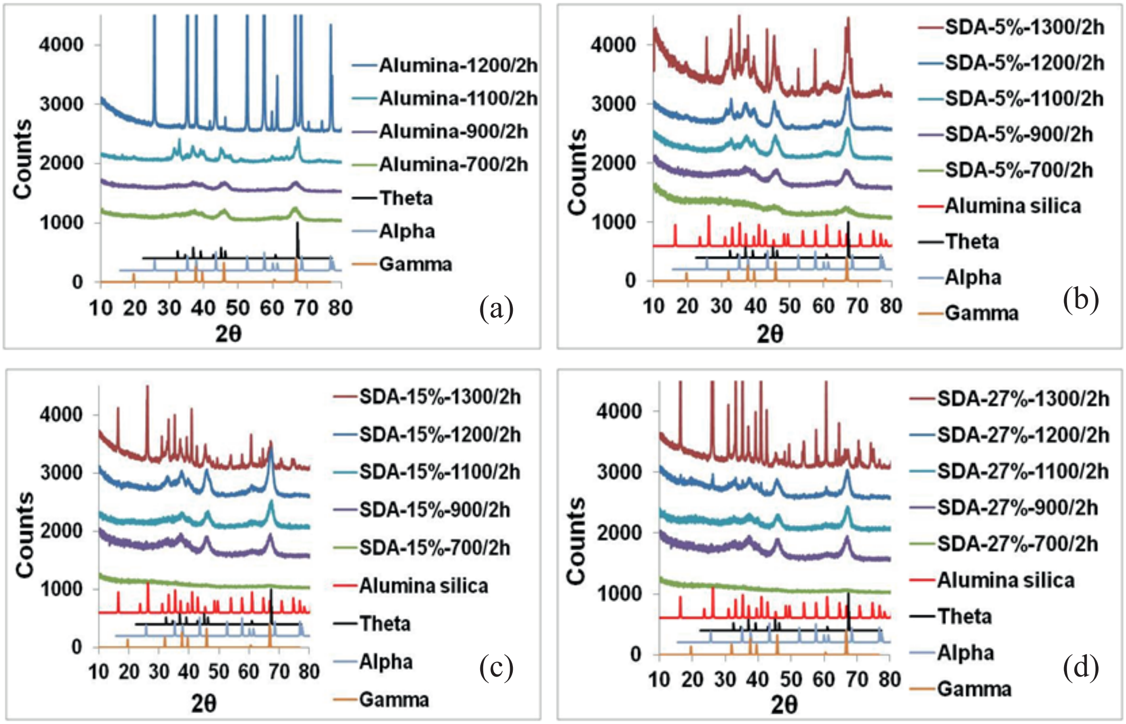

SDA: Silica-doped alumina

Figure 3.2: XRD patterns of different aluminas calcined at different temperatures for 2 h. (a) Pure alumina, (b) 5% SDA, (c) 15% SDA, (d) 27% SDA. Standards: 1) Gamma alumina. 2) Alpha alumina. 3) Theta alumina. 4) Mullite.

Figure 3.2b shows XRD patterns of 5% silica-doped alumina (5% SDA), calcined from 700 to 1300°C for 2 h. Characteristic peaks of γ-Al_2O_3, along with traces of θ-Al_2O_3 are observed for 5% SDA after calcination at 1200°C, suggesting that the phase is largely stable and the transition to the α phase has not yet occurred at this temperature. The peaks attributed to α-Al_2O_3 are not observed until 1300°C. A comparison of these results with other published SDA materials is given below.

Figure 3.3 shows in situ high-temperature XRD patterns for 5% SDA in flowing purified air. It is evident that the γ-Al_2O_3 phase in 5% SDA is stable to 1200°C

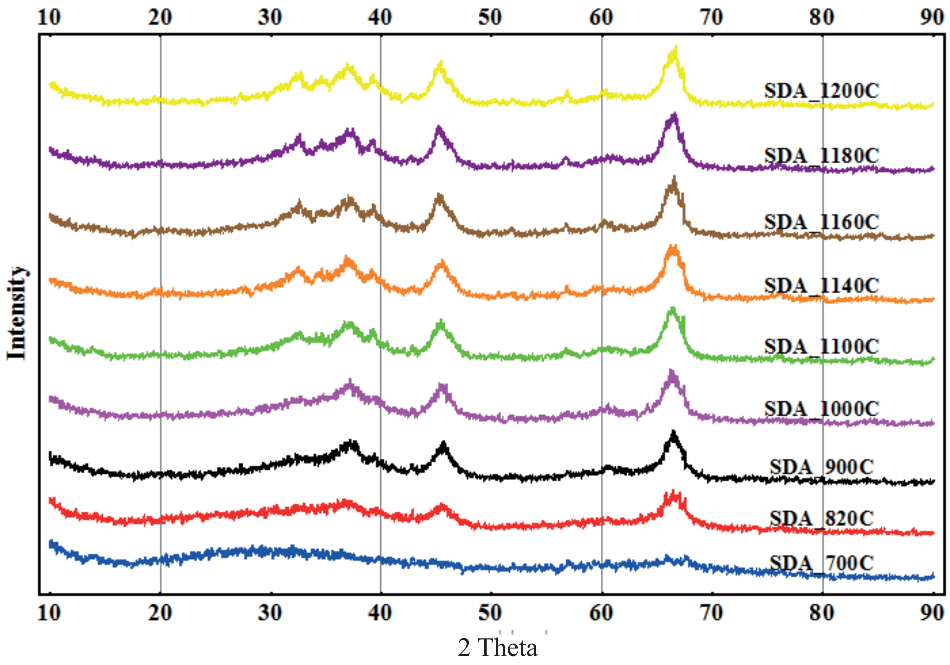

SDA: silica-doped alumina

Figure 3.3: In situ high-temperature XRD patterns of 5% SDA 700-1200°C.

without transforming to either θ-Al_2O_3 or α-Al_2O_3, since no θ-Al_2O_3 or α-Al_2O_3 peaks are detected at 1200°C . The in situ results are largely consistent with those for the ex situ furnace-calcined samples (Fig. 3.2a).

3.3.2 Nitrogen adsorption

Table 3.1 shows surface areas, pore volumes, and pore diameters for pure alumina and three silica-doped alumina samples, calcined at 700, 900, 1100 and 1200°C. The surface area and pore volume of the pure alumina sharply decreases with increasing calcination temperatures from 1100 to 1200°C; however, the addition of silica maintained the surface area and pore volume of the aluminas. In addition,

Table 3.1: BET results of 0-5-15-27% SDAs calcined at different temperatures for 2h.

Silica%	CalcinationT (°C /2 h)	BET surface area $(m^2/g)^a$	Mesopore volume $(cm^3/g)^a$	Pore diameter $(nm)^b$	Standard deviation (nm)
0%	700	291	1.56	19.8	1.1
	900	208	1.12	25.5	1.2
	1100	119	0.77	26.7	1.6
	1200	15	0.05	0.00	-
5%	700	378	1.83	14.7 and 35.0	1.8
	900	300	1.60	19.8 and 51.8	1.8
	1100	160	0.99	22.5 and 52.0	1.8
	1200	111	0.59	29.4	1.6
15%	700	222	1.40	43.1	1.8
	900	180	1.10	39.2	1.8
	1100	146	0.96	33.6	1.6
	1200	100	0.66	31.1	1.6
27%	700	195	1.0	51.6	1.5
	900	143	0.89	51.3	1.4
	1100	100	0.57	45.4	1.8
	1200	65	0.33	48.6	1.9

a)Determined by N_2 adsorption at 77 K

b)Determined by improved slit pore geometry (SPG) model for large pore sizes using the desorption branch

5% silica-doped alumina (SDA) shows a bimodal pore size distribution and larger pore diameter compared to other aluminas. The 5% SDA has a surface area of 160 m^2/g, a pore volume of 0.99 cm^3/g, and a bimodal pore distribution of 22.5 and 52 nm at 1100°C. The surface area, pore volume, and pore diameter were 111 m^2/g, 0.59 cm^3/g, and 29 nm, respectively for the same sample at 1200°C.

3.3.3 TEM images

TEM images (Fig. 3.4a) show that primary particles of 5% SDA are slab-like, and have a length of 20 nm, a width of 15 nm, and a thickness of 5 nm. The thickness of the slabs was calculated based on XRD using the Scherrer formula [34](Fig. 3.2a) and is consistent with the TEM images. A random three dimensional stacking of these primary particles is also observed. However, the pure alumina (Fig. 3.4b) has similar slab-like primary particles but less order in the stacking, which is consistent with the nitrogen adsorption results since the former possesses a larger pore volume than the latter. Consequently, at higher temperatures (i.e. 1100°C, Fig. 3.4c), the size of the 5% SDA primary particle remains relatively small; no significant grain growth is observed due to sintering from the γ to α phase transition which is consistent with the XRD results.

3.3.4 TGA and DSC

Figure 3.5a shows the TG (thermogravimetric analysis) and DSC (differential scanning calorimetry) curves of the 5% SDA sample. From the data it is clear that the weight of 5% SDA decreases by increasing the temperature to 1400°C. This weight loss is associated with the endothermic effect around 100°C due to the evaporation of alcohol and physically adsorbed water. There are also three exothermic effects: first, between 800 and 1000°C due to crystallization of the γ-Al_2O_3 phase; second between 1000 and 1300°C due to θ-Al_2O_3 or silica-alumina phase formation and collapsing of the 3D stack structure of γ-Al_2O_3 (as shown in Fig. 3.4c); and third after 1300°C due to the θ/γ phases to α-Al_2O_3 phase transition. In contrast, the γ-Al_2O_3 to α-Al_2O_3 phase transition starts at 1200°C for pure alumina (Fig. 3.5b). These results confirm that the addition of 5 wt.% of silica delays the γ-Al_2O_3 to α-Al_2O_3 phase transition by 100°C, consistent with the XRD results.

3.3.5 Solid state NMR measurements

Solid state ^{27}Al MAS NMR spectra and corresponding deconvolutions are shown in Fig. 3.6. Three different major Al environments are observed: an octahedral Al (VI) environment at $\delta \sim +15$ ppm, a five-coordinated Al (V) site at $\delta \sim +40$

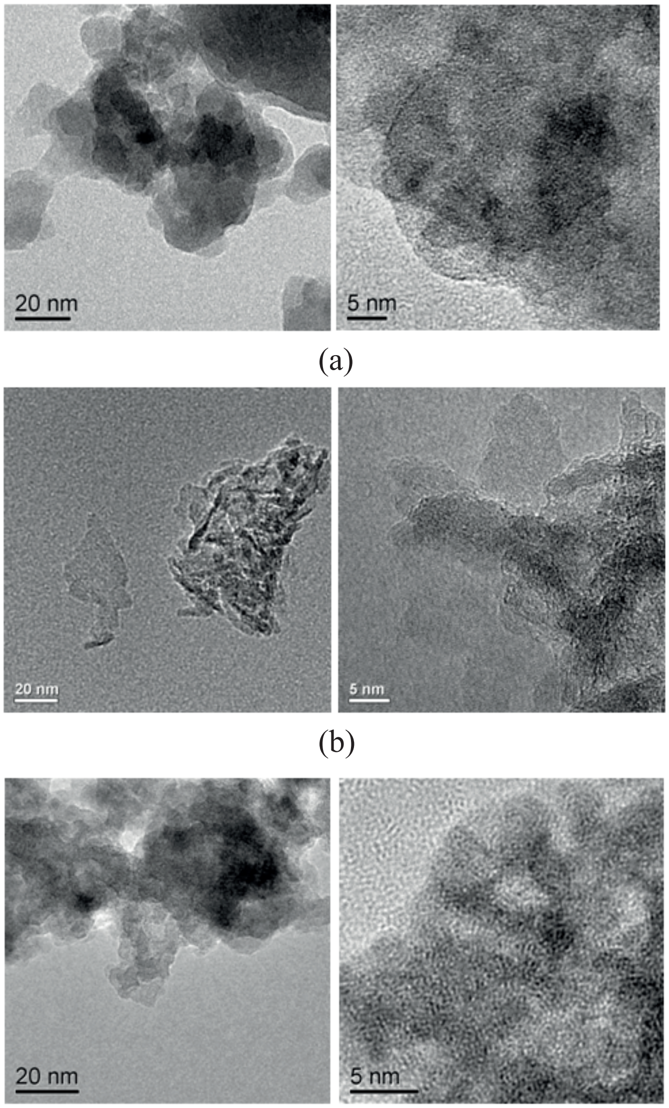

(a)

(b)

(c)

Figure 3.4: TEM micrographs of aluminas calcined at different temperatures: (a) 5% SDA calcined at 700°C, (b) Pure alumina calcined at 700°C, (c) 5% SDA calcined at 1100°C.

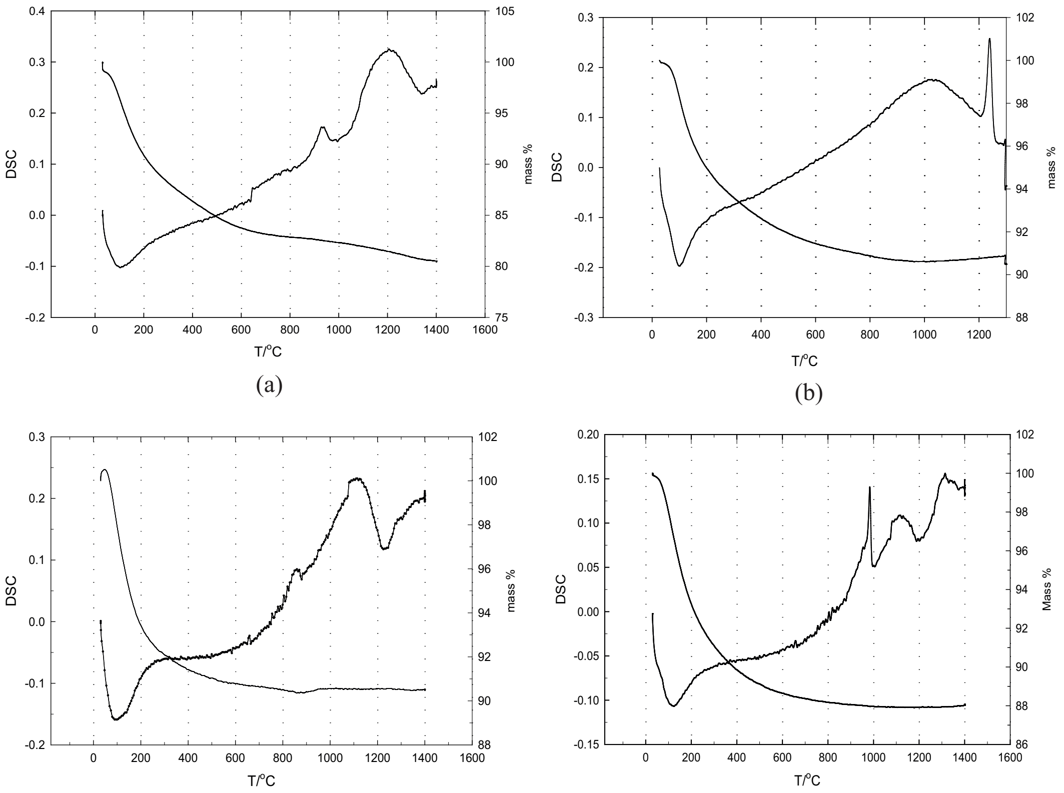

(a) (b) (c) (d)

Figure 3.5: Thermal analysis data for: (a) 5% SDA, (b) pure alumina, (c) 15% SDA d) 27% SDA.

ppm and a tetrahedral site at +75 ppm [39–41]. Pure alumina calcined at 700°C has 18% of the Al in the octahedral Al (IV) environment; after adding 5% silica, the percent of tetrahedral Al remains the same (18%, 700°C), while there is an increase in the Al (V) environment. The ^{29}Si MAS NMR and ^{29}Si-^{1}H CPMAS NMR spectra for 5% SDA is shown in Fig. 3.7a. There is a broad overlapping resonance between (-) 81 and (-) 89 ppm. This broad resonance cross-polarizes (CP) with protons, and represents a phase in this material containing proton species (hydroxyl groups). (-) 81 ppm is assigned to Si(4Al), and (-) 89 ppm for Si(3Al) structures [41–43]. The lack of the SiO_4 species ($\delta \sim$ -110 ppm) shows that Si incorporates into Al rich coordination environments. This indicates that no separate Si domain exists in the structure. 5% SDA (Fig. 3.7a) is shifted to a less negative δ in comparison to 27% silica (Fig. 3.7b), most likely due to increased Al in the Si coordination sphere. For 27% SDA (Fig. 3.7b) more peaks are observed due to different Si and Al coordination structures (e. g. Si(3Al), Si(2Al), Si(1Al), etc.) [43].

3.4 Discussion

3.4.1 Silica-alumina structure

It is reported that alumina is a defect spinel structure, in which vacancies are distributed in both octahedral and tetrahedral sites [44]. Silica content has been theoretically calculated to be 13%, if Si and Al fill all of the tetrahedral and octahedral sites [17, 45]. The results of this study show that ideal porosity and thermal stability of alumina are achieved by adding 5% silica.

It was shown from ^{27}Al MAS NMR data for 5% SDA (Fig. 3.6) that aluminum ions in tetrahedral sites are not displaced from tetrahedral to octahedral sites by addition of silicon ions, contrary to the conclusion of Horiuchi et al. [17]; instead, Si enters the tetrahedral vacancies in the defect spinel structure of alumina and forms a Si-Al spinel phase since Al (IV) content is the same (18%) in both pure alumina and 5% SDA.

The results of this study confirm those reported from earlier papers [12, 15–17, 20, 29–31, 46], that addition of a small amount of silica significantly enhances the thermal stability of the γ-Al_2O_3 lattice structure up to very high temperatures (1200°C) without formation of α-Al_2O_3. I suggest that Si doping may stabilize the oxygen lattice and therewith retard the γ-Al_2O_3 to α-Al_2O_3 phase transition (Fig.

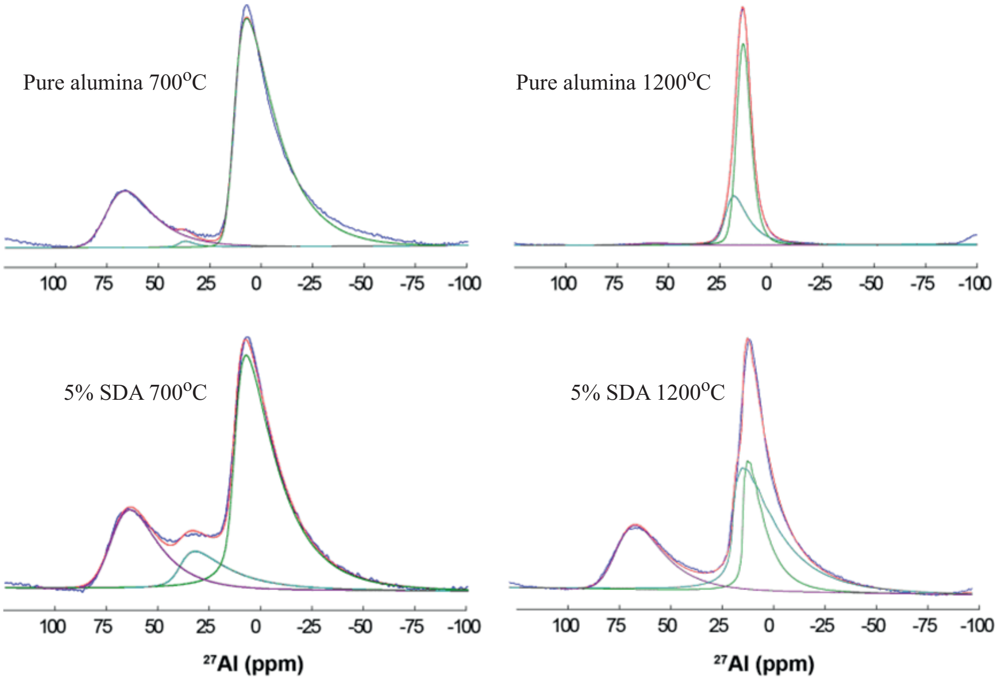

Sample ID	Calcination T °C / 2h	Al (IV)%	Al (V)%	Al (VI)%
Pure alumina	700	18	2	80
	1200	1	0	99
5% SDA	700	18	19	63
	1200	22	2	76
27% SDA	700	14	29	57
	1200	24	1	75

SDA: Silica-doped alumina

Figure 3.6: The 1D ^{27}Al MAS NMR spectra for 5 and 27% SDAs and alumina calcined at 700 and 1200°C for 2 h.

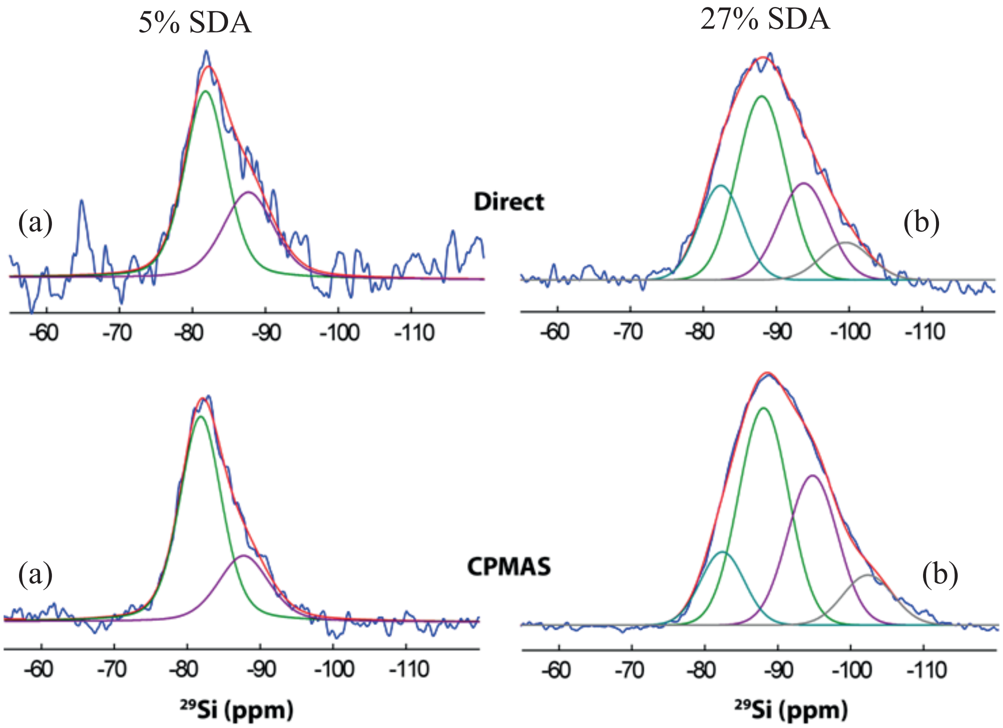

Figure 3.7: Direct ^{29}Si MAS NMR and ^{29}Si-^{1}H CPMAS spectra for (a) 5% SDA, and (b) 27% SDA calcined at 700°C for 2 h.

3.2b). A similar conclusion has also been reported by Smith et al. [47] for the addition of lanthanum.

Thus, for the transformation of γ-Al_2O_3 to α-Al_2O_3, more energy is needed for oxygen atoms to undergo rotations to restructure the oxygen lattice from *fcc* (γ-Al_2O_3) to *hcp* (α-Al_2O_3) and to suppress atomic diffusion of Al and O to the surface. It is known that the grain growth (α formation) and decrease in surface area are due to ionic diffusion [45]. Diffusion occurs in expanding neck regions and includes dislocations and lattice defects where alpha nucleation occurs [14]. Alpha formation or grain growth formations proceed at contacting points where defects and stresses exist [17,48]. The NMR data in Fig. 3.6 confirm that pure alumina is in the hexagonal alpha phase at 1200°C since 4-coordinated and 5-coordinated Al essentially disappear, and the distribution (line width) of the Al (IV) is significantly reduced suggesting the formation of α-Al_2O_3, since only 6-coordinated Al exist in α-Al_2O_3 phase [49]. However, for 5% SDA calcined at 1200°C, 4- and 6-coordinated Al are still present, confirming that the addition of silica to alumina stabilizes spinel γ-Al_2O_3 phase to 1200°C, consistent with XRD and TGA results.

Evidence that the γ to α transformations are minimized in the 5% SDA structure compared to that of pure alumina which is also shown in the TEM image (Fig. 3.4b) for this sample. The 5% SDA samples have larger slab like primary particles, more stacking and fewer neck regions than pure alumina. This results in lower bulk density and less contacting points between the alumina crystallites. In this study, the preparation involving a H_2O/Al ratio of 5:1 involves relatively slow hydrolysis, formation of larger plates, and 3D stacking morphology, all of which result in greater porosity [8]. This observation is consistent with the nitrogen adsorption results, since 5% SDA has a larger pore volume than pure alumina (Table 3.1).

In addition to stabilizing the lattice structure of γ-Al_2O_3, Si addition may also affect the ordering and stability of crystal agglomerates. From the NMR data (Fig. 3.6), the increased Al (V) concentration for 5% SiO_2/Al_2O_3 treated at 700°C relative to the undoped sample (0% Al (V)) can be attributed to the formation of an interfacial silica-alumina phase in between primary crystallites in an agglomerate. The ^{29}Si MAS NMR results also support this idea. Figure 3.7a shows that the silica-alumina network originates in a structure consisting of Al-O-Si linkages and no separate SiO_2 phase is detected (no peak at $\delta \sim$ -110 ppm) suggesting that Si incorporates into alumina structure and forming silica-alumina phase in γ-Al_2O_3

structure. Indeed, in amorphous silica-alumina, Al (V) has been assigned to the interface between the alumina phase and a silica-alumina phase [50]. This concept is consistent with an earlier observation that addition of silica increases disordering of alumina primary particles [51]. Moreover, it is also reported that bridging Al atoms that stabilize stacking fault defects in γ-Al_2O_3 structure are Al (V) [49] Another view is that the interfacial silica-alumina phase disrupts the γ-Al_2O_3 structure to form a new Si-Al spinel phase, consistent with data showing that alumina containing less than 28% silica forms a Al-Si spinel structure [52]. However, commercial 5% silica doped alumina (Siral-5) has two separated phases of SiO_2 and Al_2O_3 [53].

The postulate of a separate silica-alumina phase at the interface of primary crystallites would suggest the possibility of different pore size regimes, which is consistent with BET data of this study showing a bimodal pore size distribution. The smaller pores in the 5% SDA structure are in the same range as for the pure alumina and are thus characteristic of those in the basic alumina structure in both doped and pure samples. On the other hand, larger pores in 5% SDA (i.e., 35-52 nm) can be assigned to the interfacial silica-alumina phase which apparently collapses at 1200°C (note the absence of large pores in Table 3.1).

3.4.2 Comparison to other silica-doped alumina

Table 3.2 shows the specific surface area, pore volume and pore diameter of lanthanum- and silica-doped aluminas synthesized by different methods and of commercial doped aluminas calcined at 700, 1100 and 1200°C. After treatment of 5% SDA prepared by the method of this study at either 1100 or 1200°C for 2 h, only the γ phase is observed; this was the case in only one previous study using cryogel methods to prepare a 10% silica/alumina. By contrast commercial and noncommercial lanthanum- and silica-doped aluminas synthesized by other methods contain both γ and α or θ after treatment at 1100 and/or 1200°C for 2 h. The surface and pore properties of the 5% SDA after treatment at 11001100°C for 2 h are remarkable in comparison to the other silica-doped aluminas. The surface area of 160 m^2/g is the largest, the pore volume of 0.99 cm^3/g is the second largest, and the pore diameters of 22.5 and 52 nm are by far the largest. The bimodal pore size distribution is also unique.

The 5% SiO_2/Al_2O_3 prepared by Horiuchi et al. [17] using supercritical drying, is uniquely stable among those prepared in previous studies. These workers reported a highly thermally stable silica-doped alumina support that remains in the θ phase after treatment at 1100°C for 1 hour with the largest pore volume of 1.3 cm^3/g compared to 0.99 cm^3/g for the 5% SDA reported here, however the pore diameter of 10 nm for their support is much smaller than the pore diameters of 5% SDA of 22.5 nm and 52.0 nm.

Table 3.3 shows the surface area and pore properties following very severe treatments at different temperatures for 24 h for 5% SDA and Siral-5 (5% silica-doped alumina from Sasol), the best commercial silica-doped support. The SDA reported here shows improvements of 46% in surface area, 155% in pore volume, and 94% in pore diameter over Siral-5 after 24 h at 1100°C. In addition, XRD data (Fig. 3.8a) shows that α-Al_2O_3 peaks are observed for Siral-5 calcined at 1100°C for 24 h. In contrast, 5% SDA XRD shows peaks attributed to γ and traces of θ-Al_2O_3 at same temperatures (Fig. 3.8b). Thus the thermally stable 5% SDA is superior to other supports in terms of maintaining a high surface area and a large porosity at higher temperatures.

Table 3.2: Surface area, pore diameter, and mesopore volume for doped aluminas with different methods at different temperatures (°C). S1= [17], S2= [20], S3= [15], S4= [16], and S5= [54].

Sample ID	**BET surface area (m^2/g)**			**Mesopore volume (cm^3/g)**			**PoreDiameter (nm)**			**Alumina phase**	
	700	**1100**	**1200**	**700**	**1100**	**1200**	**700**	**1100**	**1200**	**1100**	**1200**
5% Si/Al$_2$O$_3$ (SDA)^{g,a}	338	160	111	1.83	0.99	0.59	14.7 and 35.0	22.5 and 52.0	29.4	Gamma	Gamma
5% Si/Al$_2$O$_3$ (Siral-5)^{f,a}	288	128	73	0.61	0.4	0.23	7.7	11.2	11.4	Gamma & Alpha	Gamma & Alpha
5% Si/Al$_2$O$_3$^{S1,b}	-	120	110	-	1.28	0.9	-	10.8	18.6	Theta	Theta
10%Si/Al$_2$O$_3$^{S2,c}	-	100	47	-	0.2	0.1	-	3.5	3.5	Gamma	Gamma
10%Si/Al$_2$O$_3$^{S3,a}	-	-	150	-	-	0.65	-	-	-	-	Alpha & Gamma
5% Si/Al$_2$O$_3$^{S4,d}	187	68	-	0.57	0.35	-	7.4	15.0	-	Alpha & Theta	-
3%La/Al$_2$O$_3$ (BLDA)^{h}	280	139	-	0.32	0.22	-	3.7	2.7	-	Gamma	-
3% La/Al$_2$O$_3$^{S5,e}	199	-	-	0.50	-	-	7.8	-	-	-	-
3% La/Al$_2$O$_3$ (Puralox-SCFa)^{f}	174	140	-	0.50	0.5	-	11.4	16	-	-	

Calcined for: a) 2h, b) 1h, c) 5h, d) 4h, e) 6h.
f) commercially availalbe; results from this study (Puralox-SCFa: 3% lanthanum doped alumina, and Siral5: 5% silica doped alumina from Sasol).
g) SDA: Synthesized silica-doped alumina.
h) LDA: Synthesized lanthanum-doped alumina.

3.5 Conclusions

In summary, I have produced a thermally stable silica-doped alumina with a high surface area, a large pore volume, and a large bimodal pore distribution via a facile, one-pot, solvent deficient method. In this study, different wt.% of Si (0, 5, 15, 27) doped aluminas were synthesized and thermally treated at different temperatures (700, 800, 1100, 1200°C). Results show that 5 wt.% silica-doped alumina possesses a

Table 3.3: BET results of 5% SDA and Siral-5 calcined at different temperatures for 24 h.

Sample ID	BET surface area (m^2/g)[a]				Mesopore volume(cm^3/g)[a]				Pore Diameter (nm)[b]			
	700°C	**900°C**	**1100°C**	**1200°C**	**700°C**	**900°C**	**1100°C**	**1200°C**	**700°C**	**900°C**	**1100°C**	**1200°C**
5% SDA[c]	349	270	131	61	1.06	1.11	0.84	0.24	16.5	18.7	23.7 and 51.3	20.0
Siral-5-Sasol[d]	262	203	90	28	0.61	0.56	0.33	0.13	8.8	10.5	12.4	18.6

a) Determined by N_2 adsorption at 77 K.
b) Determined by an improved slit pore geometry (SPG) model for large pore sizes using the desorption branch.
c) SDA: Synthesized silica-doped alumina; Gamma and traces of theta alumina peaks are observed at 1100 and 1200^oC for 24 h.
d) Siral-5: Commercially available 5% silica-doped alumina; Alpha alumina peaks are observed at 1100 and 1200^oC for 24 h.

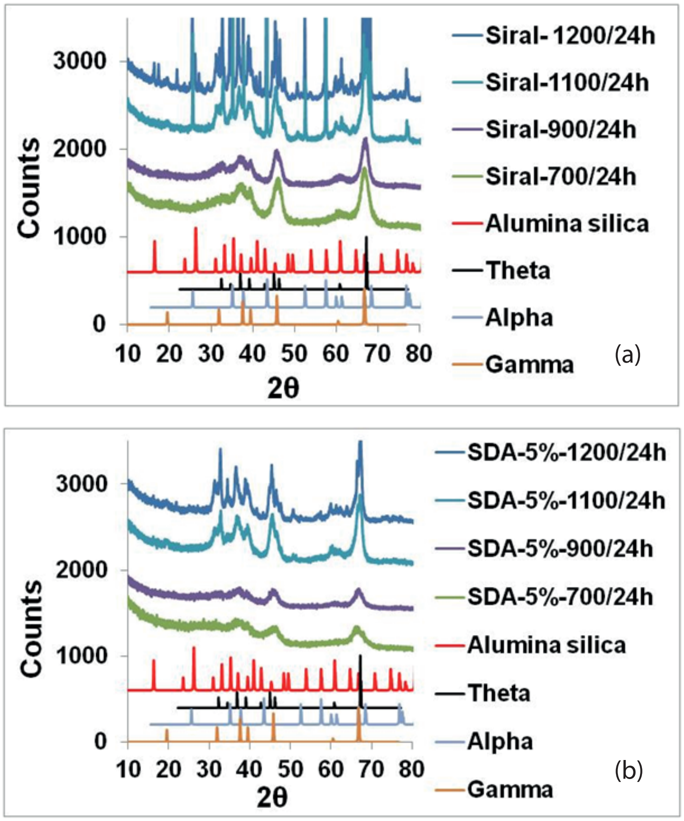

SDA: Silica-doped alumina
Siral: Sasol 5% silica-doped alumina

Figure 3.8: XRD patterns of (a) Siral-5 calcined at different temperatures for 24 h, (b) 5% SDA calcined at different temperatures for 24 h.

high surface area of 160 m^2/g, large pore volume of 0.99 cm^3/g, and a large bimodal pore size distribution of 23 and 52 nm after thermal treatment at 1100°C. It remains in the gamma phase to 1200°C.

The results of this study also provide insight into the mechanism of the stabilization of silica-doped alumina, as follows:

1. Silica stabilizes the oxygen lattice of γ-Al_2O_3 and retards the α-Al_2O_3 formation by formation of an interfacial silica-alumina phase in between primary crystallites in the agglomerate, which affects the ordering and stability of the γ-Al_2O_3 crystal agglomerates.

2. The 5 wt.% silica content is enough to enter tetrahedral vacancies in the γ-Al_2O_3 structure which forms an interfacial silica-alumina phase which disrupts the γ-Al_2O_3 structure, improves stability, and forms a second large pore size distribution in the structure.

In terms of applications, silica-doped aluminas prepared via this facile, one-pot method, have favorable pore properties and excellent thermal stability. Therefore, it is the ideal catalyst support for high temperature applications, including automobile emission control, hydrotreating of petroleum feedstocks (hydrodesulphurization), and Fischer-Tropsch synthesis.

Bibliography

[1] M. Ozawa, “Thermal stabilization of catalytic compositions for automobile exhaust treatment through rare earth modification of alumina nanoparticle support,” *J. Alloys Compd.*, vol. 408-412, pp. 1090–1095, 2006. 1, 12, 19, 70, 71, 99

[2] H. Pines and W. O. Haag, “Alumina: catalyst and support. ix. the alumina catalyzed dehydration of alcohols,” *J. Am. Chem. Soc.*, vol. 83, pp. 2847–52, 1961. 12, 70, 126

[3] O. V. Klimov, M. A. Fedotov, A. V. Pashigreva, S. V. Budukva, E. N. Kirichenko, G. A. Bukhtiyarova, and A. S. Noskov, “Complexes forming from ammonium paramolybdate, orthophosphoric acid, cobalt or nickel nitrate, and carbamide in solution and their use in the preparation of diesel fuel hydrodesulfurization catalysts,” *Kinet. Catal.*, vol. 50, no. 6, pp. 867–873, 2009. 1, 12, 70, 99

[4] C. H. Bartholomew and R. J. Farrauto, *Fundumental of industrial catalytic processes*, 2nd ed. John Wiley and sons Inc., 2006. 1, 12, 70, 99

[5] A. R. de la Osa, A. De Lucas, A. Romero, J. Valverde, and P. Sanchez, “Influence of the catalytic support on the industrial fischer-tropsch synthetic diesel production,” *Catalysis Today*, vol. 176, pp. 298–302, 2011. 1, 12, 20, 70, 72, 99

[6] S. Q. Liu, J. Boerio-Goates, and B. F. Woodfield, "Preparation of uniform nanoparticles of ultra-high purity metal oxides, mixed metal oxides, metals, and metal alloys ii," 2006. 12, 70, 135, 139, 141

[7] C. Bartholomew, B. Woodfield, B. Huang, R. Olsen, and A. L., "Method for making highly porous, stable metal oxide with a controlled pore structure," *in: WO Application Brigham Young University*, p. 40, 2011. 12, 70

[8] B. Huang, C. H. Bartholomew, S. J. Smith, and B. F. Woodfield, "Facile solvent-deficient synthesis of mesoporous γ-Al_2O_3 with controlled pore structures," *Microporous Mesoporous Mater.*, vol. 165, pp. 70–78. 12, 15, 18, 70, 85, 115, 150, 157

[9] J. Cejka, "Organized mesoporous alumina: synthesis, structure and potential in catalysis," *Applied catalysis A*, vol. 254, pp. 327–338, 2003. 2, 9, 12, 70, 99

[10] C. Morterra and G. Magnacca, "A case study: surface chemistry and surface structure of catalytic aluminas, as studied by vibrational spectroscopy of adsorbed species," *Catal. Today*, vol. 27, no. 3-4, pp. 497–532, 1996. 12, 70, 99

[11] R. K. Oberlander, "Aluminas for catalysts - their preparation and properties," *Appl. Ind. Catal.*, vol. 3, pp. 63–112, 1984. 12, 70, 99

[12] J. W. Curley, M. J. Dreelan, and O. E. Finlayson, "High temperature stability of alumina fiber," *Catal. Today*, vol. 10, no. 3, pp. 401–4, 1991. 19, 20, 71, 82, 99, 128

[13] T. Fukui and M. Hori, "Thermal stability of aluminas by hydrothermal treatment of an alkoxide-derived gel," *J. Mater. Sci.*, vol. 30, no. 7, pp. 1794–800, 1995. 19, 71

[14] T. Horiuchi, T. Osaki, T. Sugiyama, H. Masuda, M. Horio, K. Suzuki, T. Mori, and T. Sago, "High surface area alumina aerogel at elevated temperatures," *J. Chem. Soc., Faraday Trans.*, vol. 90, no. 17, pp. 2573–8, 1994. 19, 71, 84, 99

[15] J. B. Miller and E. I. Ko, "A homogeneously dispersed silica dopant for control of the textural and structural evolution of an alumina aerogel," *Catal. Today*, vol. 43, no. 1-2, pp. 51–67, 1998. xii, 19, 20, 71, 72, 82, 88, 99

[16] A. A. Shutilov, G. A. Zenkovets, S. V. Tsybulya, and V. Y. Gavrilov, "Effect of silica on the stability of the nanostructure and texture of fine-particle alumina," *Kinet. Catal.*, vol. 53, no. 1, pp. 125–136, 2012. xii, 19, 20, 71, 72, 82, 88, 128

[17] T. Horiuchi, L. Chen, T. Osaki, T. Sugiyama, K. Suzuki, and T. Mori, "A novel alumina catalyst support with high thermal stability derived from silica-modified alumina aerogel," *Catal. Lett.*, vol. 58, no. 2,3, pp. 89–92, 1999. xii, 19, 20, 71, 72, 82, 85, 87, 88, 99, 115

[18] A. W. Espie and J. C. Vickerman, "Aluminas modified with silica. part 1. an x-ray diffraction and secondary-ion mass spectrometry study of the influence of preparation and thermal treatment on structure and surface composition," *J. Chem. Soc., Faraday Trans. 1*, vol. 80, no. 7, pp. 1903–13, 1984. 19, 20, 71, 128

[19] J. Klein and W. F. Maier, "Thermal stability of sol-gel-derived porous am-alxzr mixed oxides," *Chem. Mater.*, vol. 11, no. 9, pp. 2584–2593, 1999. 19, 71

[20] T. Osaki, K. Nagashima, K. Watari, and K. Tajiri, "Silica-doped alumina cryogels with high thermal stability," *J. Non-Cryst. Solids*, vol. 353, no. 24-25, pp. 2436–2442, 2007. xii, 19, 20, 71, 72, 82, 88, 128

[21] J.-H. Lee, S.-C. Choi, D.-S. Bae, and K.-S. Han, "Synthesis and microstructure of silica-doped alumina composite membrane by sol-gel process," *J. Mater. Sci. Lett.*, vol. 18, no. 17, pp. 1367–1369, 1999. 19, 71

[22] G. Lopez-Granada, J. D. O. Barceinas-Sanchez, R. Lopez, and R. Gomez, "High temperature stability of anatase in titania-alumina semiconductors with enhanced photodegradation of 2, 4-dichlorophenoxyacetic acid," *J. Hazard. Mater.*, p. Ahead of Print, 2013. 19, 71

[23] X. Jiang, B. P. Bastakoti, W. Weng, T. Higuchi, H. Oveisi, N. Suzuki, W.-J. Chen, Y.-T. Huang, and Y. Yamauchi, "Preparation of ordered mesoporous alumina-doped titania films with high thermal stability and their application to high-speed passive-matrix electrochromic displays," *Chem. - Eur. J.*, vol. 19, no. 33, pp. 10 958–10 964, 2013. 19, 71

[24] T. Horiuchi, Y. Teshima, T. Osaki, T. Sugiyama, K. Suzuki, and T. Mori, "Improvement of thermal stability of alumina by addition of zirconia," *Catal. Lett.*, vol. 62, no. 2-4, pp. 107–111, 1999. 19, 71

[25] R. H. R. Castro, S. V. Ushakov, L. Gengembre, D. Gouvea, and A. Navrotsky, "Surface energy and thermodynamic stability of gamma-alumina: Effect of dopants and water," *Chem. Mater.*, vol. 18, no. 7, pp. 1867–1872, 2006. 19, 71

[26] Z. Cai, J. Li, K. Liew, and J. Hu, "Effect of La_2O_3-dopping on the Al_2O_3 supported cobalt catalyst for Fischer-Tropsch synthesis," *J. Mol. Catal. A: Chem.*, vol. 330, no. 1-2, pp. 10–17, 2010. 19, 71

[27] M. Schoeneborn, A. Paeger, and R. Gloeckler, “Ceria zirconia alumina composition with enhanced thermal stability,” *Sasol Germany GmbH, Germany*, p. 14, 2013. 19, 71

[28] K. Schermanz, A. Sagar, M. Schoeneborn, R. Gloeckler, K. Dallmann, F. Alber, and S. Rolfs, “Ceria zirconia alumina composition with enhanced thermal stability,” *Treibacher Industrie AG, Austria; Sasol Germany GmbH*, p. 34, 2013. 19, 71

[29] R. J. Nozemack and J. F. Porinchak, “Alumina-silica cogel,” *W. R. Grace and Co., Newyork, N.Y., U.S. Patent 4780446*, 1988. 19, 71, 82

[30] H. K. C. Timken, “Homogeneous modified-alumina Fischer-Tropsch catalyst supports,” *Chevron U.S.A. Inc., USA*, p. 8, 2005. 19, 71, 82

[31] C. Z. Wan and J. C. Dettling, “Stabilized alumina catalyst support coatings,” *Engelhard Corp., USA*, p. 23, 1986. 20, 71, 82

[32] T. Fukui and M. Hori, “Control of micropore size distribution in alumina by the hydrothermal treatment of an alkoxide derived-alcogel,” *J. Mater. Sci.*, vol. 31, no. 12, pp. 3245–3248, 1996. 20, 71

[33] M. K. Mardkhe, B. F. Woodfield, and C. H. Bartholomew, “A method of producing thermally stable and high surface area Al_2O_3 catalyst supports,” *Brigham Young University, U.S. Patent 61-851-506*, 2013. 73

[34] A. L. Patterson, “The scherrer formula for x-ray particle size determination,” *Physical review*, vol. 56, no. 10, pp. 978–982, 1939. 65, 74, 78, 153, 163, 166

[35] B. Huang, C. H. Bartholomew, and B. F. Woodfield, “Improved calculations of pore size distribution for relatively large, irregular slit-shaped mesopore structure,” *Microporous and mesoporous materials*, 2013. 74

[36] B. Bureau, G. Silly, J. Buzar, C. Legein, and D. Massiot, “From crystalline to glassy gallium fluoride materials an NMR study of 69Ga and 71Ga quadrupolar nuclei,” *Solid State NMR*, vol. 14, pp. 191–202, 1999. 75

[37] D. Massiot, F. Fayon, M. Capron, I. King, S. Le Calv, B. Alonso, J. O. Durand, B. Bujoli, Z. Gan, and G. Hoatson, “Modelling one and two-dimensional solid-state nmr spectra,” *Magn. Reson. Chem.*, vol. 40, pp. 70–76, 2002. 75

[38] D. R. Neuville, L. Cormier, and D. Massiot, “Al environment in tectosilicate and peraluminous glasses: A ^{27}Al MQ−MAS NMR, Raman, and XANES investigation,” *Geochimica et Cosmochimica Acta*, vol. 68, no. 24, pp. 5071–5079, 2004. 75, 133

[39] H. Yong, D. Coster, F. R. Chen, J. G. Davis, and J. J. Fripiat, “Aluminum coordination and Lewis acidity in aluminas and steamed zeolites,” *Stud. Surf. Sci. Catal.*, vol. 75, no. New Frontiers in Catalysis, Pt. B, pp. 1159–70, 1993. 81, 135

[40] W. E. E. Stone, G. M. S. El Shafei, J. Sanz, and S. A. Selim, “Association of soluble aluminum ionic species with a silica-gel surface: a solid-state NMR study,” *J. Phys. Chem.*, vol. 97, no. 39, pp. 10 127–32, 1993. 81, 135

[41] L. M. Bronstein, D. M. Chernyshov, R. Karlinsey, J. W. Zwanziger, V. G. Matveeva, E. M. Sulman, G. N. Demidenko, H.-P. Hentze, and M. Antonietti,

"Mesoporous alumina and aluminosilica with Pd and Pt nanoparticles: Structure and catalytic properties," *Chem. Mater.*, vol. 15, no. 13, pp. 2623–2631, 2003. 81

[42] C. Gerardin, S. Sundaresan, J. Benziger, and A. Navrotsky, "Structural investigation and energetics of mullite formation from sol-gel precursors," *Chem. Mater.*, vol. 6, no. 2, pp. 160–70, 1994. 81

[43] C. H. Bartholomew and R. J. Farrauto, *Fundumentals of industrial catalytic processes*, 2nd ed. John Wiley and sons Inc., 2006. xii, 2, 41, 42, 81, 82, 126, 137

[44] R. X. Fischer, H. Schneider, and M. Schmucker, "Crystal structure of Al-rich mullite," *Am. Mineral.*, vol. 79, no. 9 and 10, pp. 983–90, 1994. 82

[45] P. Burtin, J. P. Brunelle, M. Pijolat, and M. Soustelle, "Influence of surface area and additives on the thermal stability of transition alumina catalyst supports. ii. kinetic model and interpretation," *Appl. Catal.*, vol. 34, no. 1-2, pp. 239–54, 1987. 82, 84

[46] T. Mori, T. Horiuchi, T. Iga, and Y. Murase, "Large surface area of silica-coated fibrous crystals of alumina after heating at $>$ 1573 K," *J. Mater. Chem.*, vol. 2, no. 5, pp. 577–8, 1992. 82

[47] S. J. Smith, "The synthesis and structural characterization of metal oxide nanoparticles having catalytic applications," Thesis, 2012. 84

[48] T. Fukui and M. Hori, "Thermal stability of aluminas by hydrothermal treatment of an alkoxide-derived gel," *J. Mater. Sci.*, vol. 30, no. 7, pp. 1794–800, 1995. 85, 99, 128

[49] S. J. Smith, S. Amin, B. F. Woodfield, J. Boerio-Goates, and B. J. Campbell, "Phase progression of γ-Al_2O_3 nanoparticles synthesized in a solvent-deficient environment," *Inorg. Chem.*, vol. 52, no. 8, pp. 4411–4423, 2013. 12, 85, 86

[50] E. J. M. Hensen, D. G. Poduval, P. C. M. M. Magusin, A. E. Coumans, and J. A. R. van Veen, "Formation of acid sites in amorphous silica-alumina," *J. Catal.*, vol. 269, no. 1, pp. 201–218, 2010. 86

[51] L. L. L. Prado, P. A. P. Nascente, S. C. De Castro, and Y. Gushikem, "Aluminium oxide grafted on silica gel surface: Study of the thermal stability, structure and surface acidity," *J. Mater. Sci.*, vol. 35, no. 2, pp. 449–453, 2000. 86, 128

[52] A. K. Chakraborty, "Range of solid solutions of silica in spinel type phase," *Adv. Appl. Ceram.*, vol. 105, no. 6, pp. 297–303, 2006. 86

[53] W. Daniell, U. Schubert, R. Glockler, A. Meyer, K. Noweck, and H. Knozinger, "Enhanced surface acidity in mixed alumina-silicas: a low-temperature FTIR study," *Appl. Catal., A*, vol. 196, no. 2, pp. 247–260, 2000. 86, 135, 137, 140

[54] Z. Cai, J. Li, K. Liew, and J. Hu, "Effect of La_2O_3-dopping on the Al_2O_3 supported cobalt catalyst for Fischer-Tropsch synthesis," *J. Mol. Catal. A: Chem.*, vol. 330, no. 1-2, pp. 10–17, 2010. xii, 88

Chapter 4

A statistical approach to control porosity and surface area in thermally stable silica-doped alumina support

4.1 Introduction

It is known that the performance of a catalyst strongly depends on the combination of textural, chemical and physical properties of the support. Among these properties, pore properties are critical for the successful design and optimization of a catalyst. Pore size is essential since each catalytic system requires a unique pore size for optimal catalyst loading, diffusion and selectivity [1–4]. Examples of this are in (1) Pt, Rh and Pd catalysts for automobile emission control (pore size 3 to 5 nm) [5–8]. (2) Co(Ni)-Mo(W) sulfide catalysts for fuel hydrodesulfurization (pore size $>$ 20 nm) [8]. (3) Co and Fe catalysts for Fischer-Tropsch synthesis (FTS) (pore size 10 to 20 nm) [1, 9]. In addition, high surface area and large pore volume usually result in higher catalyst loading, which increases the number of catalytic reaction sites and decreases reaction time [1]. Moreover, it is important to produce supports with good thermal stability since pore collapsing due to sintering at high temperatures often results in catalyst deactivation [10–15].

It has been reported previously that the pore properties of alumina catalyst supports are significantly influenced by a number of synthesis parameters, including the choice of aluminum source, synthesis route, structure directing agent, and solvent [16–21]. For example, Du et al. [16] synthesized alumina with pore diameters from 2-20 nm using sodium aluminate. Alumina having pore diameters from 4 to 8 nm have been prepared using nonionic polyethylene oxide-based surfactants [17], CTAB (cetyltrimethylammonium bromide), carboxylic acid, and stearic acid surfactants [18–20], but poor thermal stability at high temperatures was reported. Zhang et al. [21] further enlarged the pore size range from 3.5 to 15 nm using TPAOH (tetrapropylammonium hydroxide), CTAB, and NaOH. Recently, Huang et al. [22] reported control of pore properties without using templates or surfactants. In their study, alumina having pore diameters from 4 to 18 nm were obtained by varying the water to aluminum molar ratio in the hydrolysis of aluminum alkoxides [22], and the pore size range was further extended from 4 to 37 nm by changing the alcohol used during the gelation [23]. In addition, it is well known that drying and calcination conditions are critical to the pore properties of alumina, since the former affects the formation of alumina precursors [24–26] and the latter induces the removal of surface hydroxyl groups, crystallization and sintering [25, 27, 28].

In Chapter 3, I introduced a facile solvent-deficient one-pot method to produce a high surface area and large pore volume $\gamma{-}Al_2O_3$ that is thermally stable up to 1200°C without transformation to $\alpha{-}Al_2O_3$. In this chapter, the control of pore sizes, with large (40-60 nm) or medium (16-19 nm) pore diameters of thermally stable $\gamma{-}Al_2O_3$, is achieved by controlling a number of synthesis factors, including mixing method, time, environment; calcination ramp rate; and alcohol concentration.

Since the pore properties are influenced by a large number of factors, it is important to understand the relationship between pore properties and each synthesis parameter; however, this requires significant time and cost to conduct all possible experiments to elucidate the effect of each variable. In this chapter I will show that through the use of a statistical design, the important relationships can be determined at a fraction of the experimental cost and time.

Split-plot factorial statistical designs [29, 30] are useful when a randomized run order is structurally impossible, expensive, or inconvenient. Statistical reasons have been provided by Anbari et al. [31] to prefer a split-plot arrangement over a completely randomized design in these situations. They have shown that a smaller prediction variance can be achieved in some split-plot arrangements of two-level factorial designs than can be achieved with the corresponding completely randomized designs. Therefore, split-plot designs are more efficient when one or more of the factors need larger experimental units than other factors, or it is harder to change the levels of one or more of the factors [29]. In the synthesis of silica doped aluminas, a full factorial split-plot experimental design was useful because factors in the mixing process (mixing method, time, environment; and alcohol concentration) could only be varied between batches of reagents, while factors in the drying and calcination steps could be varied between portions of a single batch.

In this chapter I used a split-plot fractional-factorial experimental design to obtain a useful mathematical model for the control of textural properties with a reduced cost and number of experiments [32,33]. Statistical analysis of the data from the experiments identified the most significant factors and interactions that affect on the pore diameter, surface area and pore volume of the resulting SDAs. The models obtained were then used to predict the ideal conditions necessary to produce high surface area, large pore volume, and differing pore sizes in the synthesis process.

4.2 Experimental

4.2.1 Material

The aluminum isopropoxide ($C_9H_{21}O_3Al$) (granular, 98+%) and the tetraethyl orthosilicate ($SiC_8H_{20}O_4$) (liquid, 99.9%) (TEOS) were purchased from Alfa-Aeser. Distilled water was used throughout the synthesis.

4.2.2 Synthesis method

Silica-doped aluminas (100 g batches) were prepared by adding aluminum isopropoxide (AIP), water in a 5:1 water to AIP mole ratio, 5 wt.% silica from TEOS, and more water in a 2:1 water to TEOS mole ratio. The mixture was then mixed and thermally treated at 700°C for 2 h with a 5 h ramp rate. To measure thermal stability, samples were calcined to 1200°C for 2 h with a 5 h ramp rate. The factors that were chosen to be varied in the split-plot factorial design were (1) a sealed mixing environment (yes or no). (2) mixing method (hand or mechanical mixing). (3) Alcohol concentration (yes (400 ml) or no (0 ml))). (4) Drying precursor temperature (25°C or 100°C), time (no or 24 h), a sealed drying environment (yes or no)]. (5) calcination ramp (1°C/min or 10°C/min). Mechanical mixing was carried out using a Bosch Universal mixer (model: MUM6N10UC). The total number of experiments was 96.

4.2.3 Statistical analysis

The specific design that I used is called a split-plot design with a full 24 factorial in the whole plots, and a $\frac{3}{4}$ fraction of a 4×2 factorial design in the subplots. The analysis of the un-replicated split-plot experiment was made in two steps. Following the procedure described by Bisgaard et al. [34], the whole plot means were analyzed in the first step to find which whole-plot factors and interactions were significant. This was done by calculating all effects and interactions in the saturated model for the 2^4 design in the whole plots, and then identifying significant effects using a half-normal plot. After eliminating the insignificant whole plot effects and interactions, the second step was performed by fitting a mixed model to the individual observations [35]. The batch was considered to be a random factor, and the model was fit using the REML method with JMP 10 software. The JMP Fit Model menu was used to test all fixed effects in the model.

4.2.4 Characterization

The prepared silica-doped alumina samples were analyzed by powder X-ray diffraction (XRD) using a PANalytical X'Pert Pro diffractrometer with a Cu Kα X-ray source (λ = 1.5418 Å) operated at 45 kV and 40 mA. Scans were performed between 10° and 90° 2θ with a step size of 0.0167° at a rate of 0.013°s^{-1}.

Nitrogen adsorption measurements were carried out using a Micromeritics Tristar 3020 for the determination of surface properties at −196°C. Surface area was calculated using the Brunauner-Emmett-Teller (BET) model in the P/P_0 range from 0.05 to 0.20. Pore volumes were determined at a single point of P/P_0 equal to 0.990. Pore size distributions were calculated using an improved slit pore geometry (SPG) model for large pore sizes [36]. Samples were degassed at 200°C under N_2 flow overnight before every measurement.

Microscopic images of sample of batch two L2 with no drying condition (Table 4.1) was obtained with an FEI Philips Tecani F30 transmission electron microscope (TEM) at a voltage of 200 kV. TEM samples were prepared by placing a drop of silica-doped alumina (1% dispersed in ethanol) on a carbon film with a copper mesh grid (Ted-Pella Inc.).

Table 4.1: Experiments to make SDAs.

Batch	Sample ID	Surface area (m^2/g)^a	Pore volume (cm^2/g)^a	Pore diameter (nm)^b	St. dev (nm)	Mixing method H:hand M:Bosch	Mixing seal Y:sealed N: not sealed	Mixing time (min) H:30 L:15	Alcohol Y:yes N:no	Drying: N:no Y:yes (Time(h)/T(°C)/ cap(on or off)	calcination ramp (°C /min)	Phase at (1200°C)^c
1	L1SDA1	261.7	1.527	35.76	1.63	H	Y	L	Y	N	1	γ
1	L1SDA2	233.2	1.431	37.78	1.64					N	10	γ
1	L1SDA5	352.9	2.124	21.4,58.4	1.9,1.3					24h/25°C /cap on	1	γ +traceθ
1	L1SDA6	272.4	1.564	44.01	1.61					24h/25°C /cap on	10	γ
1	L1SDA7	269.2	1.524	44.28	1.57					24h/25°C /cap off	1	γ
1	L1SDA8	280.5	1.647	45.47	1.48					24h/25°C /cap off	10	γ
2	L2SDA1	311.6	1.689	18.8,60.4	2.9,1.4	M	Y	H	N	N	1	γ +traceα
2	L2SDA2	341.9	1.667	18.7,50.1	1.6,1.6					N	10	γ +traceα
2	L2SDA5	367.2	1.948	15.9,49.3	1.5,1.6					24h/100°C /cap off	1	γ +traceα
2	L2SDA6	392.7	2.134	16.1,49.4	1.5,1.6					24h/100°C /cap off	10	γ +traceθ
2	L2SDA7	329.9	1.735	16.7,49.4	1.6,1.6					24h/25°C /cap on	1	γ +traceα
2	L2SDA8	319.9	1.542	19,51.3	1.8,1.9					24h/25°C /cap on	10	γ +traceθ
3	L3SDA1	402.1	1.937	16.91	1.32	H	Y	L	N	N	1	γ +traceθ
3	L3SDA2	336.2	1.799	18.23	1.25					N	10	γ +traceθ
3	L3SDA5	384.2	1.63	15.9	1.24					24h/100°C /cap off	1	γ +traceθ
3	L3SDA6	434.3	2.128	16.47	1.39					24h/100°C /cap off	10	γ +traceθ
3	L3SDA7	447.4	2.194	15.56	1.41					24h/25°C /cap on	1	γ +traceθ
3	L3SDA8	389.5	1.969	17.82	1.23					24h/25°C /cap on	10	γ +traceθ
4	L4SDA1	344.5	1.768	17.21	1.26	M	N	L	N	N	1	γ +traceα
4	L4SDA2	356.3	1.635	18.38	1.32					N	10	γ +traceα
4	L4SDA5	408.2	1.836	17.04	1.27					24h/25°C /cap on	1	γ +traceα
4	L4SDA6	385.6	1.888	17.51	1.28					24h/25°C /cap on	10	γ +traceα
4	L4SDA7	348.5	1.662	18.75	1.35					24h/25°C /cap off	1	γ +traceα
4	L4SDA8	340.5	1.719	18.75	1.31					24h/25°C /cap off	10	γ +traceθ
5	L8SDA1	335.6	1.651	21.5,53.8	2.1,1.6	M	N	L	Y	24h/25°C /cap on	1	γ +traceα
5	L8SDA2	285.1	1.56	22.4,60.2	2.5,1.2					24h/25°C /cap on	10	γ +traceα
5	L8SDA5	318.7	1.493	36.66	1.66					24h/25°C /cap off	1	γ +α
5	L8SDA6	288.5	1.578	21,54.7	2.0,1.6					24h/25°C /cap off	10	γ +α
5	L8SDA7	408.2	2.245	17.8,47.9	1.5,1.7					24h/100°C /cap off	1	γ +traceα
5	L8SDA8	382.4	2.264	18.6,49	1.8,1.6					24h/100°C /cap off	10	γ +traceα
6	L6SDA1	315.5	1.198	20.7,53.5	2.3,1.5	M	Y	L	Y	N	1	γ
6	L6SDA2	209.1	1.167	28.6,61.2	3.2,0.9					N	10	γ
6	L6SDA5	429.7	2.437	18,48.4	1.6,1.7					24h/100°C /cap off	1	γ+traceα
6	L6SDA6	309.2	1.815	22.2,58.8	2.5,1.6					24h/100°C /cap off	10	γ
6	L6SDA7	336.5	1.594	22.0,57.2	2.2,1.5					24h/25°C /cap on	1	γ+traceθ
6	L6SDA8	309.9	1.786	21.1,50.5	2.0,1.8					24h/25°C /cap on	10	γ
7	L7SDA1	235.2	1.139	27.7,61.7	3.5,1.0	M	Y	H	Y	N	1	γ
7	L7SDA2	294.4	1.64	22.6,60.6	3.4,0.9					N	10	γ +α
7	L7SDA5	388.1	2.364	20.0,57.5	1.9,1.0					24h/100°C /cap off	1	γ+traceθ
7	L7SDA6	378.4	2.284	19.4,48.8	1.6,1.8					24h/100°C /cap off	10	γ+traceθ
7	L7SDA7	242	1.275	23.5,59.5	2.4,1.4					24h/25°C /cap off	1	γ
7	L7SDA8	246.4	1.319	23.1,60	2.8,1.4					24h/25°C /cap off	10	γ
8	L15SDA1	367.6	1.681	16.65	1.27	H	N	L	N	24h/100°C /cap off	1	γ +traceα
8	L15SDA2	392.8	1.536	17.29	1.24					24h/100°C /cap off	10	γ +α
8	L15SDA5	349.8	1.48	13.73	1.31					24h/25°C /cap on	1	γ
8	L15SDA6	366.7	1.922	17.21	1.23					24h/25°C /cap on	10	γ+traceθ
8	L15SDA7	423.8	2.145	19.4	1.37					24h/25°C /cap off	1	γ +traceα
8	L15SDA8	414.5	2.145	17.55	1.26					24h/25°C /cap off	10	γ +traceα
9	L10SDA1	340.5	1.721	16.8,48.4	1.5,1.9	H	Y	H	N	N	1	γ
9	L10SDA2	356.3	1.643	15.6,45.4	1.6,1.4					N	10	γ
9	L10SDA5	314.6	1.74	16.9,48	1.5,1.9					24h/100°C /cap off	1	γ
9	L10SDA6	355.7	1.9	17.3,47.9	1.4,1.7					24h/100°C /cap off	10	γ
9	L10SDA7	431.2	2.359	16.6,47.1	1.4,1.6					24h/25°C /cap off	1	γ
9	L10SDA8	430.9	2.196	15.9,44.7	1.4,1.3					24h/25°C /cap off	10	γ

a)Determined by N_2 adsorption at 77 K
b)Determined by improved slit pore geometry (SPG) model for large pore sizes usin the desorption branch

4.2.5 Synthesis results

Table 4.1 shows the list of experiments for the un-replicated split-plot design experiments to produce the silica-doped alumina (SDA) catalyst supports. It shows that all synthesized SDAs are mostly in gamma or theta phases at 1200°C (based on XRD data) suggesting high thermal stability (Fig. 4.1.

4.2.6 Statistical model

The statistical prediction equations determined from the data analysis for surface area, pore volume, and pore diameters are shown in Eqs. 4.1, 4.2, and 4.3 given below.

$$SA_{ijklm} = \mu + A_i + M_j + w_{(ij)k} + D_l + C_m + AM_{ij} + AD_{il} + AC_{im} + DC_{lm} + AMD_{ijl} + AMC_{jml} + \epsilon_{ijklm} \quad (4.1)$$

where SA_{ijklm} is the surface area in the kth batch, prepared using the ith level of excess alcohol and the jth level of mixture method, the lth level of drying method and the mth level of calcination ramp. A_i is the fixed main effect of the excess alcohol, M_j is the fixed main effect of the mixing method, and $w_{(ij)k}$ is the random effect of the kth batch nested in the combination of excess alcohol and mixing method. C_m is the fixed main effect of drying method, D_l is the fixed main effect of the calcination ramp, ϵ_{ijklm} is the random subplot error term, and the other terms in the model are interactions among the main effects.

$$PV_{ijk} = \mu + M_i + w_{(i)j} + D_k + \epsilon_{ijk} \quad (4.2)$$

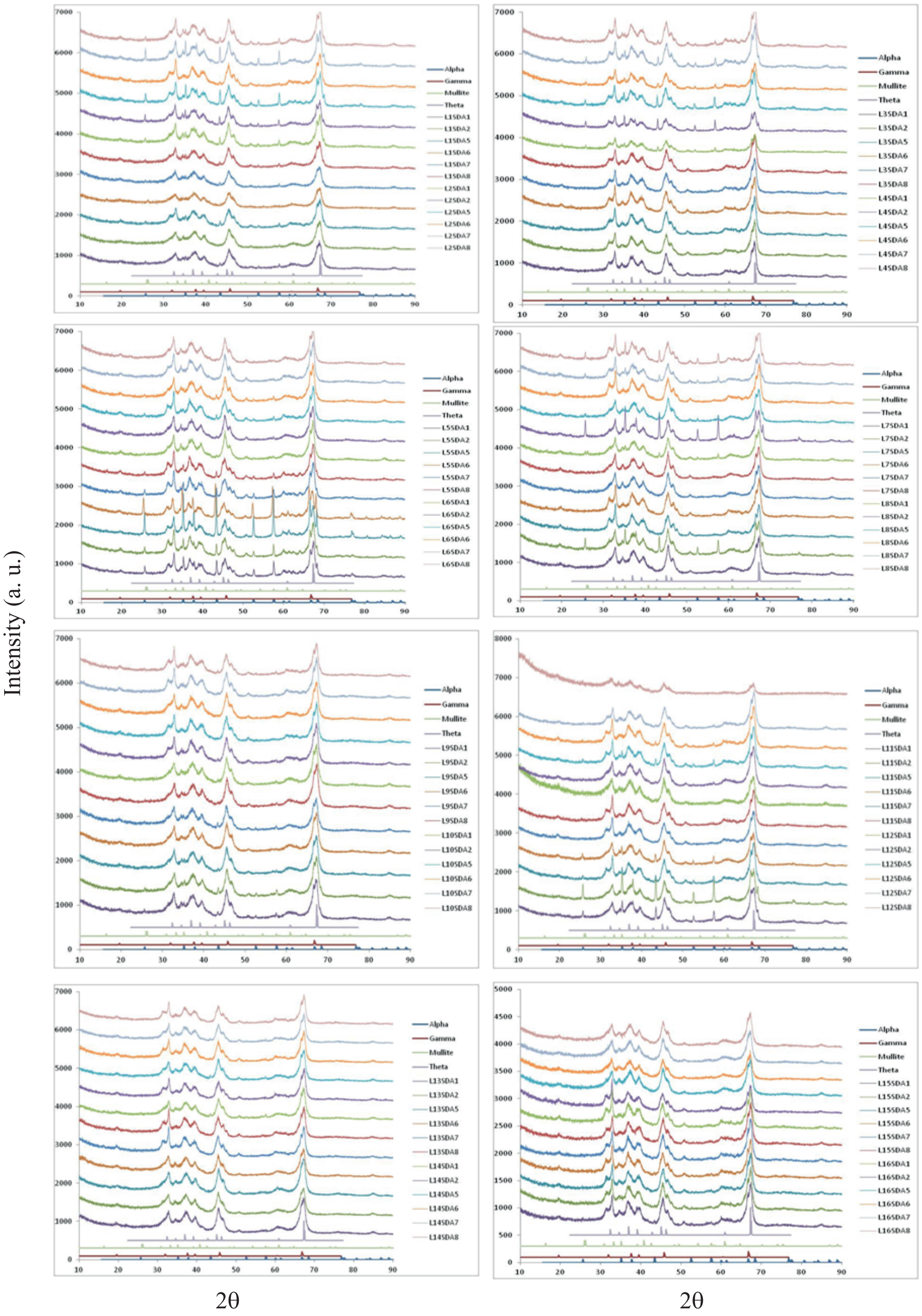

Figure 4.1: XRD of SDAs calcined at 1200°C for 2 h.

where PV_{ijk} is the pore volume in the jth batch prepared using the ith level of excess alcohol, and the kth level of drying method. M_i is the fixed main effect of mixing method, D_k is the fixed main effect of drying method, and ϵ_{ijk} is the random subplot error term.

$$PD_{ijklm} = \mu + A_i + M_j + S_k + T_l + ST_{kl} + MS_{jk} + MT_{jl} + AMST_{ijkl} + w_{ijklm} \quad (4.3)$$

where, PD_{ijklm} is the large pore diameter in the mth batch prepared using the ith level of excess alcohol, the jth level of mixing method, the kth level of mixing seal, and the lth level of mixing time. A_i is the fixed main effect of excess alcohol, M_j is the fixed main effect of mixing method, S_k is the fixed main effect of mixing seal, T_l is the fixed main effect of mixing time, w_{ijklm} is the random batch effect, and the other terms in the model are interactions among the main effects.

4.2.7 Influence of factors on surface area

Figure 4.2 shows that the excess alcohol usage has the largest effect on the surface area. On average, adding excess alcohol decreases surface area by 71.87 m^2/g. In addition, due to the significant interaction between excess alcohol, drying method, and mixing method, the change in surface area caused by adding excess alcohol depends on both the mixing method and the drying method. Also, due to the interaction between adding excess alcohol and the calcination ramp, the change in surface area caused by adding excess alcohol is slightly different depending on the calcination ramp.

It is shown in Fig. 4.2 that adding alcohol causes a decrease in surface area in most situations. However, when the batch is hand mixed and dried for 24 h at 100°C without sealing the drying environment, adding alcohol increases surface area from 368 m^2/g to 407 m^2/g. Also when the batch was mixed by machine and dried for 24 h at 100°C without sealing the drying environment, adding alcohol has very little effect on the surface area. On average the effect of adding alcohol reduces surface area when the batch was mixed by machine rather than by hand.

Figure 4.3 illustrates the dependency between the effect of excess alcohol and the calcination ramp. When the calcination ramp is 10°C/min, adding excess alcohol decreases surface area by 91.3 m^2/g. However, when the calcination ramp is reduced to 1°C/min adding excess alcohol only decreases the surface area by 52.4 m^2/g. Figure 4.2 also shows that the effect of drying method on surface area depends on both the mixing method and whether excess alcohol is added. This is again due to the significant interaction between excess alcohol, drying method and mixing method.

4.2.8 Influence of factors on pore diameter

Figure 4.4 shows that, on average, adding excess alcohol increases pore diameter by 18.6 nm. However, due to the significant interactions, the change in pore diameter caused by adding excess alcohol is much greater or less than 18.6 nm depending on the mixing method used and whether a sealed mixing environment was used. In the left panel (Fig. 4.4) where no sealed mixing environment is used and the batch is mixed by hand, adding excess alcohol increases pore diameter by about 25 nm regardless of the mixing time. On the other hand, when a sealed mixing environment is used and the batch is mixed by hand for 30 minutes, adding excess alcohol only increases the large pore diameter by about 5 nm. The change in pore diameter caused by adding excess alcohol for all 8 combinations of sealed mixing environment, mixing method and mixing time is visualized as the vertical differences in the ends of the lines in Fig. 4.4.

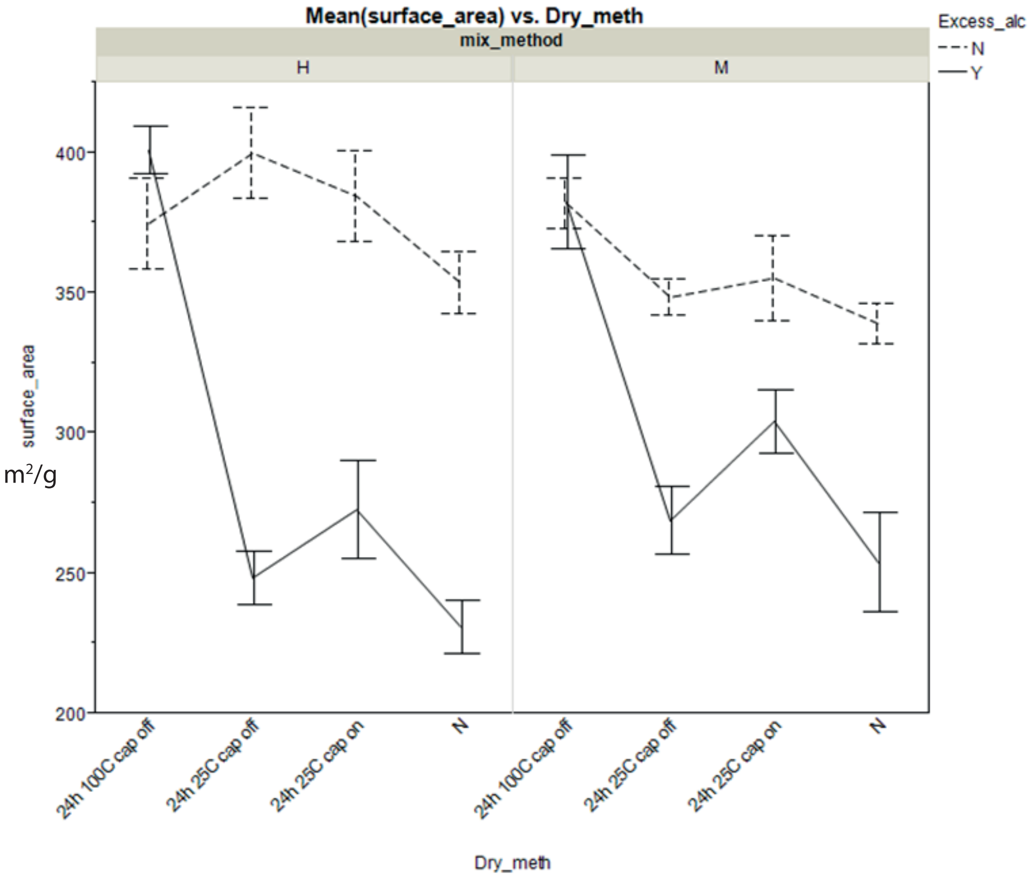

Mixing method: H(hand mix), M(machine)
Excess alcohol: N(No), Y(Yes)
Drying method: 24h 100°C cap off (24 h drying at 100°C in unsealed mixing environment)
Drying method: 24h 25°C cap on (24 h drying at 25°C in sealed mixing environment)
Drying method: N(No)

Figure 4.2: Interaction of excess alcohol, drying method and mixing method on surface area.

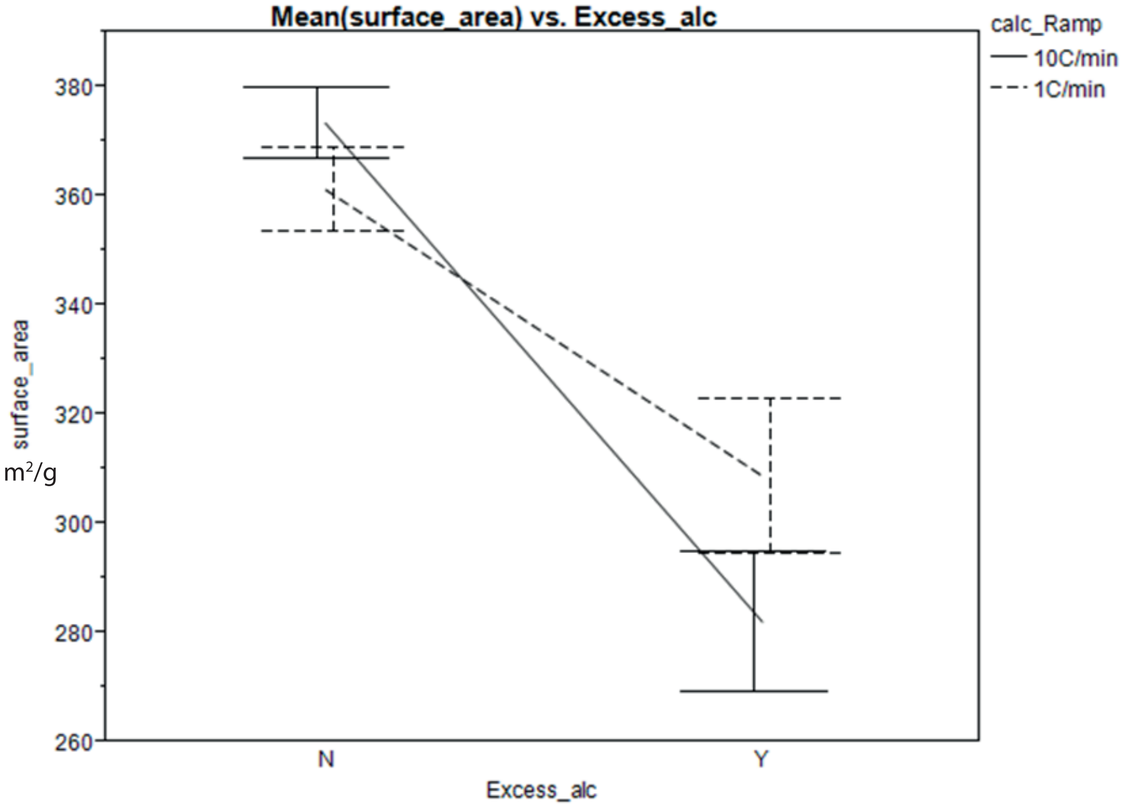

Excess alcohol: N(No), Y(Yes)
Calcinations ramp: 100°C /min or 1°C/min

Figure 4.3: Interaction of excess alcohol and calcination ramp on surface area.

4.2.9 Influence of factors on pore volume

As seen in Fig. 4.5, drying method has the most significant effect on pore volume, where drying at 100°C in an unsealed drying environment for 24 h produces the largest pore volume. No drying condition produces the smallest pore volume, and there is little difference in pore volume between the other two drying conditions

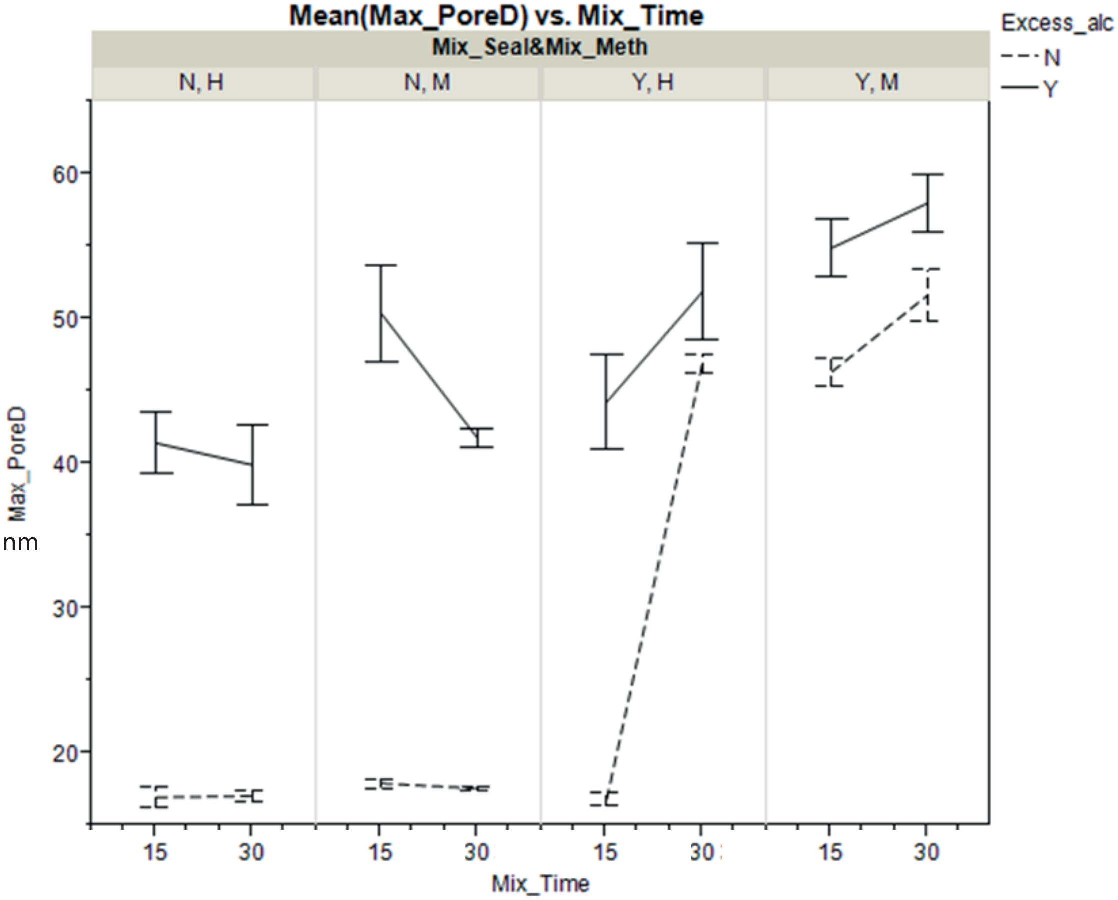

Mixing time: 15 or 30 minutes
Excess alcohol: N(No), Y(Yes)
Mixing seal: N(No), Y(Yes)
Mixing method: H(hand mix), M(machine)

Figure 4.4: Interaction between excess alcohol, mixing time, mixing seal and mixing method on pore diameter.

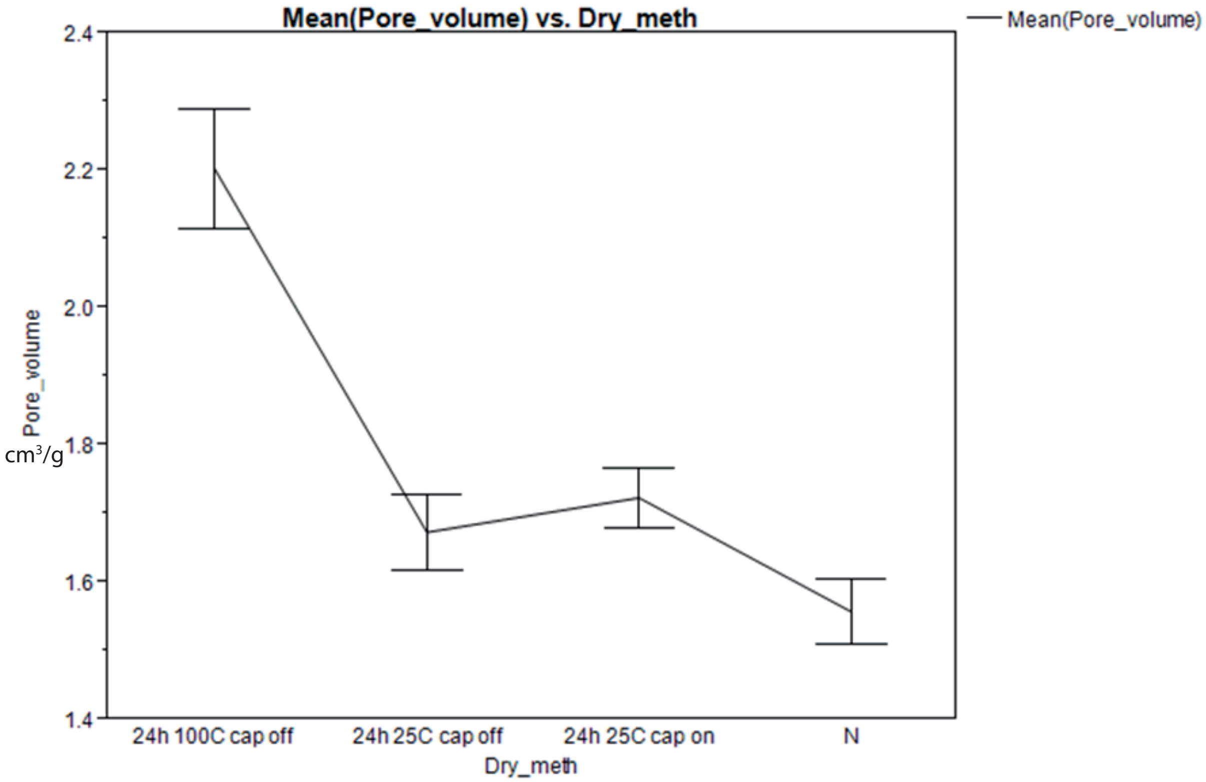

Drying method: 24h 100°C cap off (24 h drying at 100°C in unsealed mixing environment)
Drying method: 24h 25°C cap on (24 h drying at 25°C in sealed mixing environment)
Drying method: N(No)

Figure 4.5: Average effect of drying method on pore volume.

at 25°C. Switching from hand mixing to machine mixing decreases pore volume on the average by 0.157 cm^2/g (see Fig. 4.6).

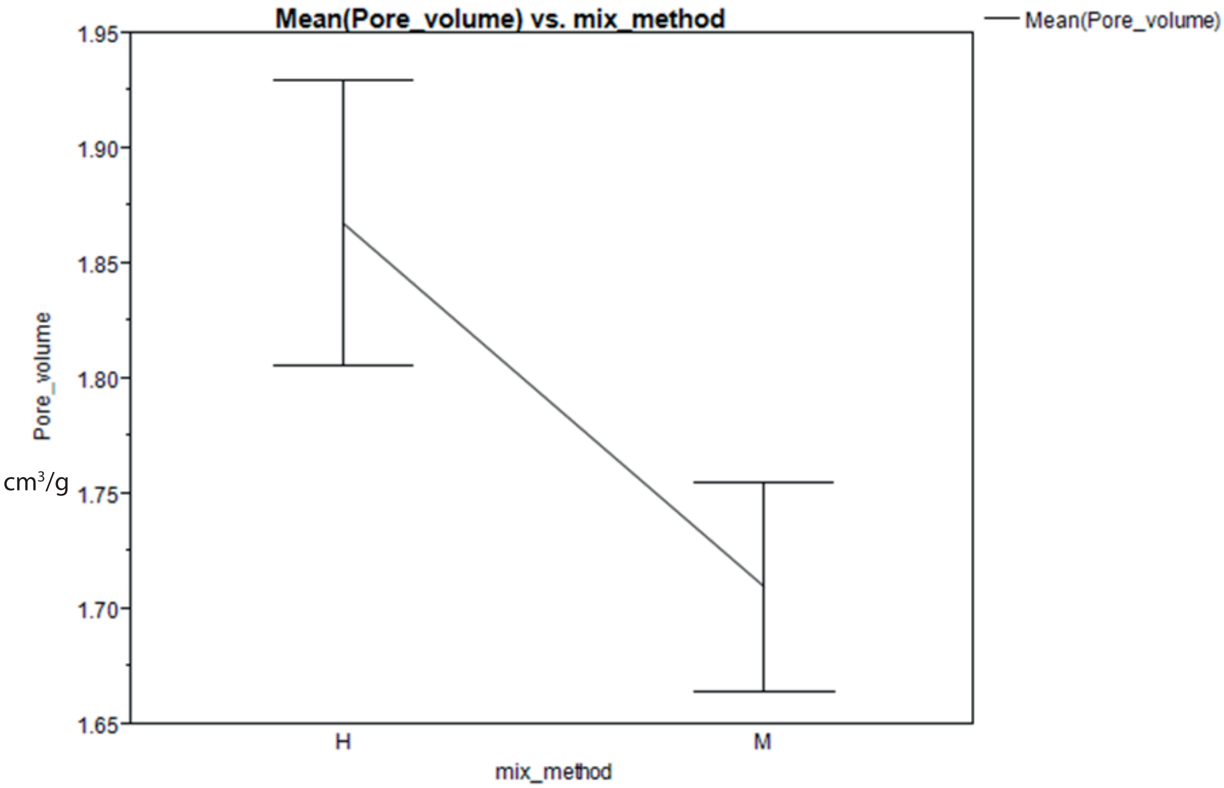

Mixing method: H(hand mix), M(machine)

Figure 4.6: Average effect of mixing method on pore volume.

4.3 Discussion

4.3.1 Confirmation of model predictions

Equations 4.1, 4.2, 4.3 and Figs. 4.2, 4.3, 4.4, 4.5, 4.6 were used to identify seven different optimal synthesis conditions that were predicted to produce SDA with large or medium pore diameters, simultaneously with a large surface area and pore volume. The seven optimal conditions were combinations of the levels or alternatives for mixing method, environment, and time; alcohol concentration, and the drying

Table 4.2: Trials to confirm the models and predictions.

Mix Method	Mix Seal	Mix Time (min.)	Excess Alcohol	Drying (T/°C)	Pred. Surface Area	Pred. Pore Volume	Pred. Pore Diameter	Actual Surface Area (m^2/g)[a]	Actual Pore Volume (cm^2/g)[a]	Actual Pore Diameter (nm)
Hand	No	30	No	100	368	1.87	17.23	282.2	1.5	18.01
Hand	Yes	15	No	100	368	1.87	16.51	414.7	2.1	18.19
Machine	No	30	No	100	388	1.71	17.88	375.4	1.9	46.7
Machine	No	15	No	100	388	1.71	18.09	381.1	1.8	20.99
Hand	Yes	30	No	100	368	1.87	47.33	340	2.5	48.7
Machine	No	30	Yes	100	350	1.71	41.96	272.8	2	45
Machine	Yes	30	Yes	100	350	1.71	58.43	371.7	2.4	47.9

a)Determined by N_2 adsorption at 77 K
b)Determined by improved slit pore geometry (SPG) model for large pore sizes usin the desorption branch

method. Table 4.2 shows these seven optimal conditions along with the predicted surface area, pore volume and large pore diameter at each condition. Confirmation experiments were run where a single batch of SDA was synthesized at each of the conditions listed in Table 4.2. The surface area, pore volume and large pore diameter for each of these batches was measured and are shown in the last three columns of Table 4.2. The results of six confirmation experiments agree with the model and graphical predictions except for experiment 3 (Experiment 3 is not reliable since 30 minutes long mixing time in unsealed mixing environment makes particles dried and spill out of the mixer bowl). The six experiments in agreement with the model predictions show that statistical analysis has indeed identified the important synthesis factors that control the surface area, pore volume, and large pore diameter of SDA. In addition it has been demonstrated that batches of SDA can be produced with high surface areas, large pore volumes, and large (40-60 nm) or medium (16-19 nm) pore diameters.

4.3.2 The effect of excess alcohol

The results from the statistical analysis show that using alcohol in the mixing step has a negative effect on surface area and a positive influence on the pore diameter of SDAs (Figs. 4.2 and 4.4), which is supported by the chemistry involved in the synthesis. Baker [37] suggested that the formation of an alumina precursor can be viewed as a polymerization of $Al(H_2O)_6^{+3}$ octahedrals. When the hydrolysis rate is slow, this polymerization occurs in three dimensions rather than one dimension under fast hydrolysis conditions. This is confirmed by the TEM images of the SDAs. As shown in Fig. 4.7, the primary particles of SDAs are slab like under slow hydrolysis condition, consistent with Baker's and Huang's results [37, 38]. Since there are a significant number of hydroxyl groups on the surfaces of the alumina precursor, excess alcohol is adsorbed on the surface planes of the bohemite crystallite (alumina precursor) via hydrogen bonding. This reduces the surface energy of the alumina precursor and inhibits the polymerization of the primary crystallites [39–41]. In addition, excess alcohol enhances the mobility of the alumina precursor and avoids pile stacking of the alumina plates. When the alcohol evaporates, an open 3D-stacking structure (or "house of cards") consisting of the alumina plates is formed and large pore diameters are observed, consistent with the results of previous studies [18, 23, 42–45]. In addition, when excess alcohol is used in combination with sealing the Bosch mixer and increasing the mixing, the pore diameter increases further, since sealing limits alcohol evaporation and helps maintain an alcohol rich environment and increased mixing enables the completion of the hydrolysis reaction and hydrogen bonding formation. Note that larger pore diameters are often observed with lower surface area [14, 15, 23, 38, 46].

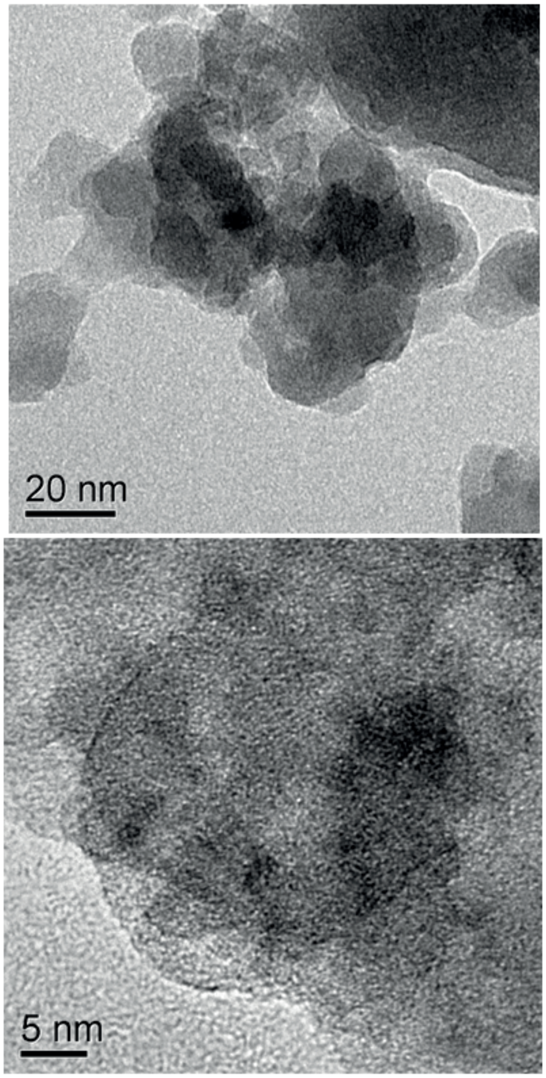

Figure 4.7: TEM micrographs of SDA synthesized from L2 batch with no drying condition

4.3.3 The effect of excess alcohol and calcination ramp rate

As mentioned in previous section, adding excess alcohol decreases the surface area. In the case of a high calcination ramp rate, the surface area decreases by 91.3 m^2/g; however, when the calcination ramp rate is slow, the surface area decreases by 52.4 m^2/g (Fig. 4.3). A slow calcination ramp rate results in slow shrinkage and formation of the isolated small particles [47]. The isolated particles have a lower tendency to bond to adjacent particles enabling them to grow into larger particles. A slow calcination ramp rate also provides sufficient time for both the interlayer hydroxyls and extra solvent to be removed without damaging the structure [23].

4.3.4 The effect of drying

From the statistical results, it is evident that drying affects the pore volume and surface area of SDAs. Pore volume and surface area increase with drying of the precursor compared to no control of the drying conditions, especially at higher temperature (100°C) (Figures 4.2, 4.5). Drying leads to formation of further M-O-M cross-links in the gel as covalent linkages replace weak interactions between surface hydroxyl and alkoxy groups. This allows neighboring M-OH or M-OR groups to approach each other and undergo a condensation reaction [47] resulting in larger pore volumes. Solvent evaporation in the drying step produces a capillary pressure due to the difference between the solid-vapor and solid-liquid interfacial energies [47]. When the capillary pressure increases, liquid moves to smaller interstices (pores) with the greatest surface to volume ratio. As a result primary particles rearrange themselves during the drying process to form pores with similar sizes [46]. Since the solvent is slowly evaporated when the precursor is dried at low temperature (25°C), there is enough time for this rearrangement process to finish [48] and a smaller pore volume is observed. In contrast, when drying occurs at higher temperatures (100°C), the solvent is removed much faster and the rearrangement is not completed resulting in a larger pore volume. Maintaining drying conditions at 25°C with a sealed environment for 24 h resulted in a higher surface area and larger pore volume than the unsealed drying environment, suggesting more cross linking and reduced pile stacking of plates due to slower alcohol evaporation.

4.4 Conclusions

The synthesis of thermally stable silica-doped alumina catalyst supports has been studied using a split-plot full fractional factorial design. From this study, the following conclusions can be drawn:

1. It was found that mixing method, time, and environment; calcination ramp rate; drying temperature and environment; and alcohol concentration can alter surface area, pore volume, and pore diameter by factors of 1.8, 1.4, and 3.3, respectively. Large pore diameters (> 40 nm), large pore volumes (> 2 cm^3/g), and high surface area (> 400 m^2/g) were obtained by addition of excess alcohol, drying at 100°C for 24 h, and no alcohol usage, respectively.

2. The proposed quantitative models can predict optimal conditions to produce SDAs with high surface areas (>250 m^2/g), large pore volume (>1 cm^3/g), and large (40-60 nm) or medium (16-19 nm) pore diameters.

Bibliography

[1] C. H. Bartholomew and R. J. Farrauto, *Fundumentals of industrial catalytic processes*, 2nd ed. John Wiley and Sons Inc., 2006. 1, 12, 70, 99

[2] J. Cejka, "Organized mesoporous alumina: synthesis, structure and potential in catalysis," *Applied catalysis A*, vol. 254, pp. 327–338, 2003. 2, 9, 12, 70, 99

[3] C. Morterra and G. Magnacca, "A case study: surface chemistry and surface structure of catalytic aluminas, as studied by vibrational spectroscopy of adsorbed species," *Catal. Today*, vol. 27, pp. 497–532, 1996. 12, 70, 99

[4] R. K. Oberlander, "Aluminas for catalysts - their preparation and properties," *Appl. Ind. Catal.*, vol. 3, pp. 63–112, 1984. 12, 70, 99

[5] K. C. Taylor, "Nitric oxide catalysis in automotive exhaust systems," *Catal. Rev. - Sci. Eng.*, vol. 35, no. 4, pp. 457–81, 1993. 1, 99

[6] D. N. Belton and K. C. Taylor, "Automobile exhaust emission control by catalysts," *Curr. Opin. Solid State Mater. Sci.*, vol. 4, no. 1, pp. 97–102, 1999. 1, 99

[7] M. Ozawa, "Thermal stabilization of catalytic compositions for automobile exhaust treatment through rare earth modification of alumina nanoparticle support," *J. Alloys Compd.*, vol. 408-412, pp. 1090–1095, 2006. 1, 12, 19, 70, 71, 99

[8] O. V. Klimov, M. A. Fedotov, A. V. Pashigreva, S. V. Budukva, E. N. Kirichenko, G. A. Bukhtiyarova, and A. S. Noskov, “Complexes forming from ammonium paramolybdate, orthophosphoric acid, cobalt or nickel nitrate, and carbamide in solution and their use in the preparation of diesel fuel hydrodesulfurization catalysts,” *Kinet. Catal.*, vol. 50, no. 6, pp. 867–873, 2009. 1, 12, 70, 99

[9] A. R. de la Osa, A. De Lucas, A. Romero, J. Valverde, and P. Sanchez, “Influence of the catalytic support on the industrial Fischer-Tropsch synthetic diesel production,” *Catalysis Today*, vol. 176, pp. 298–302, 2011. 1, 12, 20, 70, 72, 99

[10] J. W. Curley, M. J. Dreelan, and O. E. Finlayson, “High temperature stability of alumina fiber,” *Catal. Today*, vol. 10, no. 3, pp. 401–4, 1991. 19, 20, 71, 82, 99, 128

[11] T. Fukui and M. Hori, “Thermal stability of aluminas by hydrothermal treatment of an alkoxide-derived gel,” *J. Mater. Sci.*, vol. 30, no. 7, pp. 1794–800, 1995. 85, 99, 128

[12] T. Horiuchi, T. Osaki, T. Sugiyama, H. Masuda, M. Horio, K. Suzuki, T. Mori, and T. Sago, “High surface area alumina aerogel at elevated temperatures,” *J. Chem. Soc., Faraday Trans.*, vol. 90, no. 17, pp. 2573–8, 1994. 19, 71, 84, 99

[13] J. B. Miller and E. I. Ko, “A homogeneously dispersed silica dopant for control of the textural and structural evolution of an alumina aerogel,” *Catal. Today*, vol. 43, no. 1-2, pp. 51–67, 1998. xii, 19, 20, 71, 72, 82, 88, 99

[14] A. A. Shutilov, G. A. Zenkovets, S. V. Tsybulya, and V. Y. Gavrilov, “Effect of silica on the stability of the nanostructure and texture of fine-particle alumina,” *Kinet. Catal.*, vol. 53, no. 1, pp. 125–136, 2012. 99, 115

[15] T. Horiuchi, L. Chen, T. Osaki, T. Sugiyama, K. Suzuki, and T. Mori, “A novel alumina catalyst support with high thermal stability derived from silica-modified alumina aerogel,” *Catal. Lett.*, vol. 58, no. 2,3, pp. 89–92, 1999. xii, 19, 20, 71, 72, 82, 85, 87, 88, 99, 115

[16] T.-B. Du, S.-M. Jang, and B.-W. Chen, “Manufacture of mesoporous alumina of boehmite type via subcritical drying and application to purify liquid crystal,” *Chem. Eng. Sci.*, vol. 62, no. 18-20, pp. 4864–4868, 2007. 99

[17] S. A. Bagshaw and T. J. Pinnavaia, “Mesoporous alumina molecular sieves,” *Angew. Chem., Int. Ed. Engl.*, vol. 35, no. 10, pp. 1102–1105, 1996. 17, 99, 100

[18] W. Deng, M. W. Toepke, and B. H. Shanks, “Surfactant-assisted synthesis of alumina with hierarchical nanopores,” *Adv. Funct. Mater.*, vol. 13, no. 1, pp. 61–65, 2003. 99, 100, 115

[19] F. Vaudry, S. Khodabandeh, and M. E. Davis, “Synthesis of pure alumina mesoporous materials,” *Chem. Mater.*, vol. 8, no. 7, pp. 1451–1464, 1996. 3, 6, 16, 99, 100, 151

[20] Y. Kim, C. Kim, P. Kim, and J. Yi, “Effect of preparation conditions on the phase transformation of mesoporous alumina,” *J. Non-Cryst. Solids*, vol. 351, no. 6-7, pp. 550–556, 2005. 99, 100

[21] Z. Zhang and T. J. Pinnavaia, “Mesoporous -alumina formed through the surfactant-mediated scaffolding of peptized pseudoboehmite nanoparticles,” *Langmuir*, vol. 26, no. 12, pp. 10 063–10 067, 2010. 16, 99, 100

[22] B. Huang, C. H. Bartholomew, S. J. Smith, and B. F. Woodfield, “Facile solvent-deficient synthesis of mesoporous γ-Al_2O_3 with controlled pore structures,” *Microporous Mesoporous Mater.*, vol. 165, pp. 70–78, 2013. 18, 100, 151

[23] B. Huang, C. H. Bartholomew, and B. F. Woodfield, “Facile structure-controlled synthesis of mesoporous γ-Al_2O_3: Effects of alcohols in precursor formation and calcination,” *Microporous Mesoporous Mater.*, vol. 177, pp. 37–46, 2013. 18, 100, 115, 117, 151

[24] M. Jafarzadeh, I. A. Rahman, and C. S. Sipaut, “Synthesis of silica nanoparticles by modified sol-gel process: the effect of mixing modes of the reactants and drying techniques,” *J. Sol-Gel Sci. Technol.*, vol. 50, no. 3, pp. 328–336, 2009. 100

[25] R. F. Silva and W. L. Vasconcelos, “Influence of processing variables on the pore structure of silica gels obtained with tetraethylorthosilicate,” *Mater. Res. (Sao Carlos, Braz.)*, vol. 2, no. 3, pp. 197–200, 1999. 100

[26] E. Ponthieu, E. Payen, G. M. Pajonk, and J. Grimblot, “Comparison of drying procedures for the preparation of alumina powders with the system al-alkoxide/tertiary butanol/water,” *J. Sol-Gel Sci. Technol.*, vol. 8, no. 1/2/3, pp. 201–206, 1997. 100

[27] J. Nair, P. Nair, J. G. Van Ommen, J. R. H. Ross, and A. J. Burggraaf, “Effect of post-precipitation treatment on the pore-structure stability of sol-gel-derived

lanthanum zirconate," *J. Am. Ceram. Soc.*, vol. 81, no. 6, pp. 1487–1492, 1998. 100

[28] G. Urretavizcaya, A. L. Cavalieri, J. M. P. Lopez, I. Sobrados, and J. Sanz, "Thermal evolution of alumina prepared by the sol-gel technique," *J. Mater. Synth. Process.*, vol. 6, no. 1, pp. 1–7, 1998. 100

[29] B. Jones, "split-plot designs: what, why, and how," *J. Quality Technology*, vol. 41, no. 4, 2009. 3, 101

[30] R. A. Fisher, *Statistical methods for research workers.* Oliver and Boyd, 1925. 101

[31] F. T. Anbari and J. M. Lucas, "Super-efficient designs: How to run your experiment for higher effeciencies and lower cost," *technical conference transactions*, pp. 852–863, 1994. 101

[32] M. Martinez and J. Aracil, "Use of factorial design in the synthesis of fine chemicals. application to the synthesis of a homolog of jojoba oil," *Ing. Quim. (Madrid)*, vol. 21, no. 248, pp. 163–8, 1989. 101

[33] G. Box and J. Hunter, *Statistics for experimenter.* New York: John Wiley and Sons, 1978. 101

[34] S. Bisgard, H. T. Fuller, and E. Barrios, "Quality quandries: Two-level factorials run as split-plot experiments," *Quality Engineering*, vol. 9, 1996. 102

[35] J. Lawson, *Design and Analysis of Experiments with SAS.* Boca Raton: CRC Press, 2010, book section 8. 103

[36] B. Huang, C. H. Bartholomew, and B. F. Woodfield, “Improved calculations of pore size distribution for relatively large, irregular slit-shaped mesopore structure,” *Microporous and mesoporous materials*, 2013. 103, 131, 168

[37] B. R. Baker and R. M. Pearson, “Water content of pseudoboehmite. new model for its structure,” *J. Catal.*, vol. 33, no. 2, pp. 265–78, 1974. xiv, 18, 19, 115

[38] B. Huang, C. H. Bartholomew, S. J. Smith, and B. F. Woodfield, “Facile solvent-deficient synthesis of mesoporous γ-Al_2O_3 with controlled pore structures,” *Microporous Mesoporous Mater.*, vol. 165, pp. 70–78, 2013. 12, 15, 18, 70, 85, 115, 150, 157

[39] R. Bleta, P. Alphonse, L. Pin, M. Gressier, and M.-J. Menu, “An efficient route to aqueous phase synthesis of nanocrystalline gamma-Al_2O_3 with high porosity: From stable boehmite colloids to large pore mesoporous alumina,” *J. Colloid Interface Sci.*, vol. 367, no. 1, pp. 120–128, 2011. 115

[40] A. Mueller, O. Heim, M. Panneerselvam, and M. Willert-Porada, “Polyol method for the preparation of nanosized Gd_2O_3, boehmite and other oxides,” *Mater. Res. Bull.*, vol. 40, no. 12, pp. 2153–2169, 2005. 115

[41] S. M. Grant and M. Jaroniec, “Effect of cosolvent organic molecules on the adsorption and structural properties of soft-templated ordered mesoporous alumina,” *J. Colloid Interface Sci.*, vol. 367, no. 1, pp. 129–134, 2012. 115

[42] R. W. Hicks and T. J. Pinnavaia, “Nanoparticle assembly of mesoporous AlOOH (boehmite),” *Chem. Mater.*, vol. 15, no. 1, pp. 78–82, 2003. 115

[43] J.-L. Blin, A. Leonard, Z.-Y. Yuan, L. Gigot, A. Vantomme, A. K. Cheetham, and B.-L. Su, “Hierarchically mesoporous/macroporous metal oxides templated

from polyethylene oxide surfactant assemblies," *Angew. Chem., Int. Ed.*, vol. 42, no. 25, pp. 2872–2875, 2003. 115

[44] A. Leonard, J.-L. Blin, and B.-L. Su, "One-pot surfactant assisted synthesis of aluminosilicate macrochannels with tunable micro- or mesoporous wall structure," *Chem. Commun. (Cambridge, U. K.)*, no. 20, pp. 2568–2569, 2003. 115

[45] B. Cormack, J. J. Freeman, and K. S. W. Sing, "Porosity of alumina gels prepared from solutions of aluminum nitrate in various alcohols," *J. Chem. Technol. Biotechnol.*, vol. 30, no. 7, pp. 367–73, 1980. 115

[46] U. Schubert and N. Husing, *Synthesis of Inorganic Material.* Wiley-VCH verlang GmbH, 2000, book section 4. 115, 117

[47] N. Yao, G. Xiong, M. He, S. Sheng, W. Yang, and X. Bao, "A novel method to synthesize amorphous silica-alumina materials with mesoporous distribution without using templates and pore-regulating agents," *Chem. Mater.*, vol. 14, no. 1, pp. 122–129, 2002. 117

[48] J. D. Wright and N. A. Sommerdijk, *Sol-Gel Materials Chemistry and Application.* Gordon and Breach Science Publisher, 2001, vol. 4, book section 2. 117

Chapter 5

Acid site properties of thermally stable, silica-doped alumina as a function of silica alumina ratio and calcination temperature

5.1 Introduction

Silica-doped aluminas (SDAs) with high surface area, porosity, thermal stability, and with the appropriate acid site concentration and strength are ideal catalyst supports in several industrially relevant reactions including auto emissions control, naphtha reforming, hydrodesulfurization, hydrocracking, isomerization, polymerization, and Fischer-Tropsch synthesis (FTS), which are important in the oil refining, petrochemical, and gas-to-liquid (GTL) industries [1–5]. For example, in hydrocracking, a silica-doped alumina with a high concentration of silica may function as the acid catalyst and the support for hydrogenation metals where the rate of isomerization and hydrocracking is proportional to the Brϕnsted acid site concentration. By contrast, an ideal silica-doped alumina for FTS contains less than 3-5 wt% silica to ensure that Brϕnsted acid site concentration is negligible, since acid sites contribute to methane selectivity, thereby reducing selectivity for the target liquid and wax hydrocarbon products. In both FTS and auto emissions control, silica-doped aluminas have superior thermal and hydrothermal stability relative to pure aluminas or zeolites.

In addition, silica-doped alumina supports may be preferred over zeolites in several of the above-mentioned processes, because they (1) contain larger mesopores which facilitate diffusion of reactants in and products out during reaction and (2) their acid site concentrations and strengths are inherently lower (relative to zeolites) and thus uniquely matched to the process chemistry for certain applications [6].

Alumina surfaces typically contain both Lewis and Brϕnsted acid sites. Adding greater than 5-6 wt% silica to alumina leads to an interaction of the two oxides to form additional, stronger Brϕnsted acid sites through bridged hydroxyl group formation between aluminum and silicon atoms [6–8]. It is well known that Brϕnsted and Lewis site concentrations increase with increasing silica content or Si/Al ratio [9, 10]. Reported concentrations of Brϕnsted acid and Lewis acid sites are 300 and 700 μmol/g in 20% silica/alumina [9]. Belver et al. [11] observed that Brϕnsted acid site concentration increases from 370 to 570 μmol/g upon addition of 40% silica to alumina.

Methods used to investigate acid-base properties of pure alumina and silica doped aluminas include DFT calculations [12], adsorption of ammonia or pyridine examined by Fourier transform infrared spectroscopy (FTIR) [7, 13–16], base exchange through FTIR [10, 17], SSNMR (solid state nuclear magnetic resonance) [6, 14, 16, 18], and temperature programmed desorption (TPD) of ammonia or alkylamines [14,16,19]. In this chapter TPD of ammonia, ^{27}Al SSNMR, and FTIR of adsorbed pyridine were used to determine acid site concentration (Lewis and Brϕnsted), acid strength, and the intrinsic Lewis acid site concentration on synthesized SDAs.

In Chapter 3 I reported a facile, solvent-deficient, one-pot method for synthesis of SDAs of high porosity and excellent thermal stability. The addition of silica in these SDAs significantly increases thermal and hydrothermal stabilities of the $\gamma\!-\!Al_2O_3$ phase to 1200°C (see Fig. 5.1), while maintaining a high surface area, a large pore volume and a large pore diameter (see Table 5.1). Compared to a commercial SDA (Siral-5 from Sasol), after calcination for 24 h at 1100°C, the surface area, pore volume, and pore diameter of SDA of equivalent silica content are higher by 46%, 155%, and 94%, respectively. Previously studied SDAs were found to be converted to $\theta-Al_2O_3$ and $\alpha-Al_2O_3$ phases of substantially lower surface area and porosity (relative to SDAs) at calcination temperatures above 1000°C; moreover, the synthesis methods involve complex, multi-step procedures and hence higher manufacturing costs [20–25]. This chapter presents acidity data for 5, 15, 27 wt% SDA supports prepared by facile, solvent-deficient method in which the $\gamma-Al_2O_3$ phase is stabilized to 1200°C.

While acid site properties of amorphous silica-doped aluminas have been reported as a function of Si/Al ratio (silica $> 40\%$) in numerous previous studies, few have examined acid site properties of SDAs as a function of dehydroxylation temperature up to 1200°C [17,26–29] or at low Si/Al ratios (silica $< 30\%$) [10,11,28,29]. In this chapter I report new results from a comprehensive study of the Brϕnsted and Lewis acid site properties of SDAs prepared by a solvent deficient hydrolysis of the organo-oxides of silicon and aluminum as a function of both Si/Al ratio (0 to 27% silica) and dehydroxylation temperature from 700 to 1200°C. The results indicate that the total acid site concentration decrease from 236 μmol/g at 700°C to 48 μmol/g at 1200°C, in 5% silica, without collapse of the porous structure or transformation to $\theta-Al_2O_3$ and $\alpha-Al_2O_3$, properties which are unique to the SDAs of this study.

Table 5.1: BET results of 0-5-15-27% SDAs calcined at different temperatures for 2h.

Silica %	Thermal treatment Temperature (°C/2 h)	BET surface area $(m^2/g)^a$	Mesopore volume $(cm^3/g)^a$	Pore diameter $(nm)^b$
5%	700°C	377.7	1.83	14.7 and 35.0
	900°C	299.9	1.60	19.8 and 51.8
	1100°C	159.2	0.99	22.5 and 52.0
	1200°C	110.7	0.59	29.4
15%	700°C	222.5	1.40	43.10
	900°C	180.5	1.10	39.17
	1100°C	145.9	0.96	33.59
	1200°C	99.59	0.66	31.15
27%	700°C	195.1	1.0	51.60
	900°C	143.3	0.89	51.30
	1100°C	100.5	0.57	45.39
	1200°C	65.0	0.33	48.60

a. Determined by N_2 adsorption at 77K.

b. Determined by improved slit pore geometry (SPG) model for large pore size using desorption branch.

5.2 Experimental

5.2.1 Material

Aluminum isopropoxide ($C_9H_{21}O_3Al$) (granular, 98+%) and tetraethyl orthosilicate ($SiC_8H_{20}O_4$) (liquid, 99.9%) (TEOS) were purchased from Alfa-Aeser. Pyridine (C_5H_5N) was purchased from EMD with grade of (99 wt. %). To ensure an anhydrous environment, pyridine was dried over molecular sieves for 24 h.

5.2.2 Synthesis method

Thermally stable SDAs were synthesized via a simple one-pot solvent deficient method that involves mixing aluminum isopropoxide (AIP) and water at a 5:1 mole ratio of water to AIP, followed by addition of TEOS (equivalent to 5 wt% silica) and

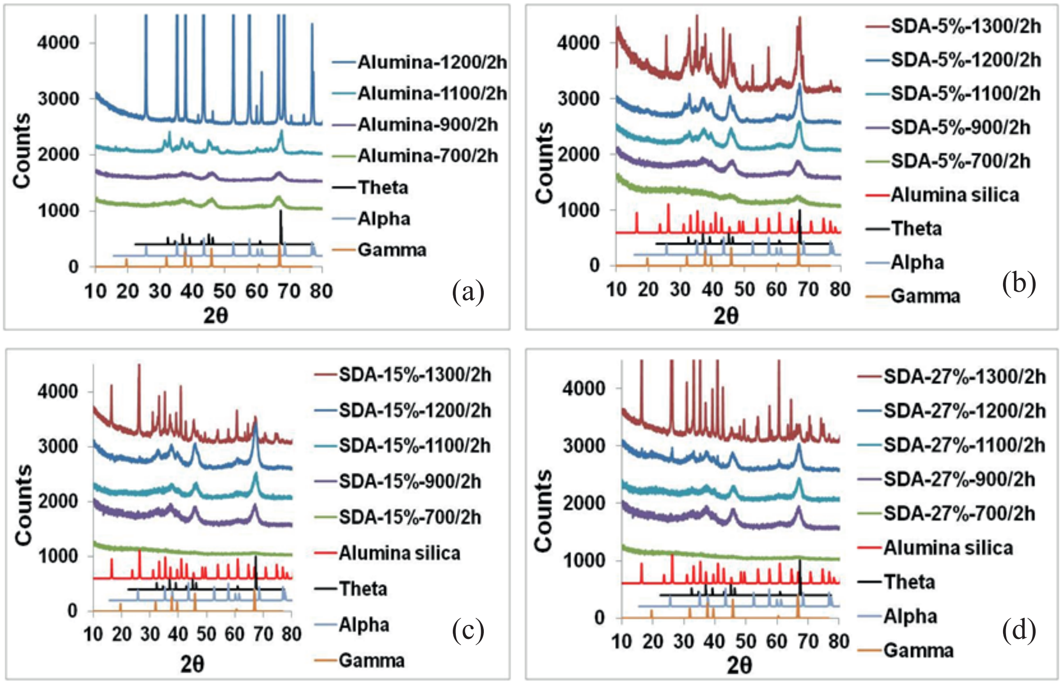

SDA: Silica-doped alumina

Figure 5.1: XRD patterns of different aluminas calcined at different temperatures for 2 h. (a) Pure alumina, (b) 5% SDA, (c) 15% SDA, (d) 27% SDA. Standards: 1) Gamma alumina. 2) Alpha alumina. 3) Theta alumina. 4) Mullite.

water at a 2:1 water to TEOS mole ratio. This precursor was mixed for 30 minutes with a Bosch Universal Mixer (model: MUM6N10UC) and followed by calcination at 700, 900, 1100, and 1200°C for 2 h each with 5 h ramp rates. Samples with 15 and 27 wt% of silica were also prepared using the same method. Details of the synthesis, characterization, and optimization of these silica-doped aluminas have been discussed in Chapters 3 and 4.

5.3 Characterization

5.3.1 Silica-doped aluminas

The SDAs prepared by solvent-deficient hydrolysis of aluminum isopropoxide with TEOS were analyzed by powder X-ray diffraction (XRD) using a PANalytical X'Pert Pro diffractrometer with a Cu Kα X-ray source ($\lambda = 1.5418$ Å) operated at 45 kV and 40 mA. Scans were performed between 10° and 90° 2θ with a step size of 0.0167° at a rate of $0.013°\text{s}^{-1}$. Nitrogen adsorption measurements were carried out using a Micromeritics Tristar 3020 for the determination of surface properties at −196°C. The surface areas of SDAs were calculated using the Brunauner-Emmett-Teller (BET) model in the P/P_0 range from 0.05 to 0.20. Pore volumes were determined at a single point of P/P_0 equal to 0.990. Pore size distributions were calculated using an improved slit pore geometry (SPG) model for large pore sizes [30]. Samples were degassed at 200°C under N_2 flow overnight before every measurement. A commercial 5 wt% silica doped alumina (Siral-5) used for comparative purposes, was obtained from Sasol (Sasol North America Inc.).

5.3.2 Acidity measurements

Total acid site concentrations were determined by TPD in a system equipped with a Pfeiffer Vacuum ThermoStar mass spectrometer. Approximately 100 mg of sample was heated overnight to remove water. A sample was degassed in-situ at 550°C for 1 h under a helium flow of 30 sccm (standard cubic centimeters per minute). The sample was cooled to an adsorption temperature of 100°C. After 1 h of NH_3 adsorption, it was switched to He to remove any physisorbed ammonia. The sample was then heated to the desorption temperature of ammonia (500°C [31]) with 10 sccm He flow at a ramp rate of 5°C/min. Spectra were obtained in the form of

μmol/L of desorbed species versus temperature. The amount of desorbed ammonia was assumed to be equivalent to the total concentration of acid sites (Brϕnsted and Lewis). Mass spectrometry was also used to verify that the desorbed molecule m/e=17 was ammonia.

To measure the Brϕnsted acid site concentrations specifically, IR transmission measurements were performed using a Nicolet 6700 Fourier transform infrared spectroscopy (FTIR-Thermo scientific) controlled using OMNIC software. A total of 120 scans were collected for each spectrum with a resolution of 6 cm^{-1}. Each spectrum was recorded at room temperature. KBr and the sample powders were heated at 350°C for 1 h before use. 200 mg of sample was exposed to pyridine vapor under helium flow in a quartz apparatus at 200°C for 30 minutes, [28] and then the physisorbed pyridine was desorbed at the same temperature under He flow for 1 h using a helium flow of 25 sccm at atmospheric pressure. The temperature was then lowered to 25°C using a cooling rate of 10°C/min. The chemisorbed pyridine SDA sample in KBr was placed in the FTIR sample cup after which the FTIR spectra of samples were collected. These measurements were carried out in air, however to address the possible loss of pyridine that might occur due to adsorption of oxygen, the FTIR spectra for the chemisorbed pyridine samples were measured after 1, 10, and 30 minutes sitting in the air. The peak intensities (relative to pyridine adsorption) did not change over this 30 minute time period.

To measure the intrinsic Lewis acid site concentrations, solid state ^{27}Al magic angle spinning nuclear magnetic resonance (MAS NMR) spectra were obtained on a Bruker Avance III 600 (14.6 T) instrument using a 4 mm broadband MAS probe. All spectra were obtained at 25°C, at a spinning speed of 12.5 kHz, using a single pulse Bloch decay, with high power ^{1}H TPPM decoupling. A pulse length of $\pi/12$ was utilized to improve quantification. The ^{27}Al NMR chemical shift was referenced to the secondary standard 1M $Al(H_2O)_6^+$ in water ($\delta = 0.0$ ppm). Spectral simulations and deconvolutions were performed using DMFIT and utilized the Czejeck distribution of the quadrupolar interaction [32] to model the ^{27}Al line shape.

5.4 Results

5.4.1 Silica-doped alumina physical properties

Figure 5.1 shows XRD patterns for pure alumina and three silica-doped alumina (SDA) samples after calcination at 700, 900, 1100 and 1200°C. For the pure alumina sample only α-Al_2O_3 is observed at 1200°C (Fig. 5.1a). In contrast, mostly the γ-Al_2O_3 phase is observed for 5, 15, 27% silica/alumina samples, respectively (Fig. 5.1b,c,d).

Table 5.1 shows surface areas, pore volumes, and pore diameters for pure alumina and the three silica-doped alumina samples, calcined at 700, 900, 1100 and 1200°C. The surface area and pore volume of the pure alumina decreases sharply by 89 and 100% respectively with increasing calcination temperatures from 1100 to 1200°C; however, with the addition of silica the surface area and pore volume decrease substantially less, e.g. for 5 wt% silica/alumina surface area and pore volume decrease by only 30 and 40% respectively. The origin of the increased thermal stability of silica-doped alumina was discussed in detail in Chapter 3.

5.4.2 Acid site properties

Temperature programmed desorption (TPD) of ammonia [35] was used for a quantitative determination of the total acid site concentration (Brϕnsted and Lewis) on SDAs with 0, 15, and 27% silica ratios and calcined for 2 h at 700, 900, and 1100°C (Fig. 5.2). The TPD results (shown in Table 5.2) show that the total acid

Table 5.2: The Brϕnsted and Lewis acid site concentrations reported in this work and in previous studies. S1 = [33], S2 = [9], S3 = [34], S4 = [11], and S5 = [17].

Sample ID	**Pretreat T (°C)**	**Total acid site conc. TPD µmol/g**	**Brønsted acid site conc. FT-IR µmol/g**	**Lewis acid site conc. FT-IR µmol/g**	**XRD at 1200°C**
5% SDA	700	236	52	183	Gamma and trace theta
	900	162	-	-	
	1100	48	-	-	
	1200	0	0	0	
15% SDA	700	490	122	367	Gamma
	900	412	-	-	
	1100	318	-	-	
	1200	0	0	0	
27% SDA	700	528	120	408	Gamma and trace mullite
	900	427	-	-	
	1100	229	-	-	
	1200	0	0	0	
3% SA^{S1}	600	-	0	-	
5% SA^{S2}	500	400	0	300	-
15% SA^{S2}	500	500	0	500	-
27% SA^{S2}	500	550	50	700	-
50% SA^{S3}	550	-	27	144	-
80% SA^{S3}	550	-	76	116	-
40% SA^{S4}	550	570	-	-	-
80% SA^{S4}	550	740	-	-	-
40% SA^{S5}	550	-	190	-	-
40% SA^{S5}	900	-	200	-	-

SDA: silica-doped alumina
SA: silica-alumina

site concentration decreases in the order 27 > 15 > 5% silica at 700 and 900°C; however, at 1100°C, the total acid site concentration decreases in the order 15 > 27 > 5%. Table 5.2) also shows that the total acid site concentration decreases with increasing calcination temperature for 5, 15, and 27% SDA samples calcined at 700, 900, and 1100°C for 2 h with 5 h ramp rates.

Solid state ^{27}Al MAS NMR spectra for 5, 15, and 27% silica after pretreatment in air at 700 to 1200°C (Fig. 5.3) show an Al(VI) environment at $\delta \sim +5$ ppm, a five-coordinated Al(V) site at $\delta \sim +33.2$ ppm and a tetrahedral site Al(IV) at +58 ppm [36, 37]. The five and six coordinated aluminums are assigned to strong Lewis and non-Lewis acid sites, respectively [12, 38, 39]. The relative concentration of the Al(V) increases as silica content increases in the $5 < 15 < 27\%$ samples calcined at 700 and 900°C; however the relative concentration of Al(V) is $\sim 0\%$ at 1100°C and 1200°C in the 5, 15 and 27% samples. Thus, the concentration of strong Lewis acid sites decreases with increasing calcination temperature and is essentially zero after calcination at 1100 and 1200°C.

FTIR data can provide relative concentrations of Brϕnsted and Lewis acid sites. Peaks in the range of 1516-1568 cm^{-1} and 1432-1467 cm^{-1} are attributed to Brϕnsted and Lewis sites, respectively [28, 40–42], but the peak around 1490 cm^{-1} cannot be assigned to a single site [28]. The concentrations of Brϕnsted and Lewis acid sites per gram of sample were estimated from the absorption peak intensity ratios, multiplied by the total acid concentration measured by the ammonia-TPD [9]. From the FTIR data (Fig. 5.4b) an increase in the intensity of peaks assigned to Lewis and Brϕnsted acid sites on SDAs increases with increasing Si/Al ratio at 700°C; however, neither Lewis and Brϕnsted acid site peaks are observed at 1200°C. Brϕnsted acid site concentrations are approximately 52, 122, and 120 μmol/g for 5, 15, and 27% at 700°C, respectively. Lewis acid site concentrations are approximately 183, 367, and 408 μmol/g for 5, 15, and 27% at 700°C, respectively (Table 5.2).

5.5 Discussion

The results of this study include new data showing for the first time total, Brϕnsted, and Lewis acid site concentrations for (1) SDAs containing less than 30% silica and (2) thermally stable SDAs calcined from 700 to 1200°C. Previous papers [34, 35, 43] covered only high silica contents, i.e. silica $> 40\%$ or low silica contents

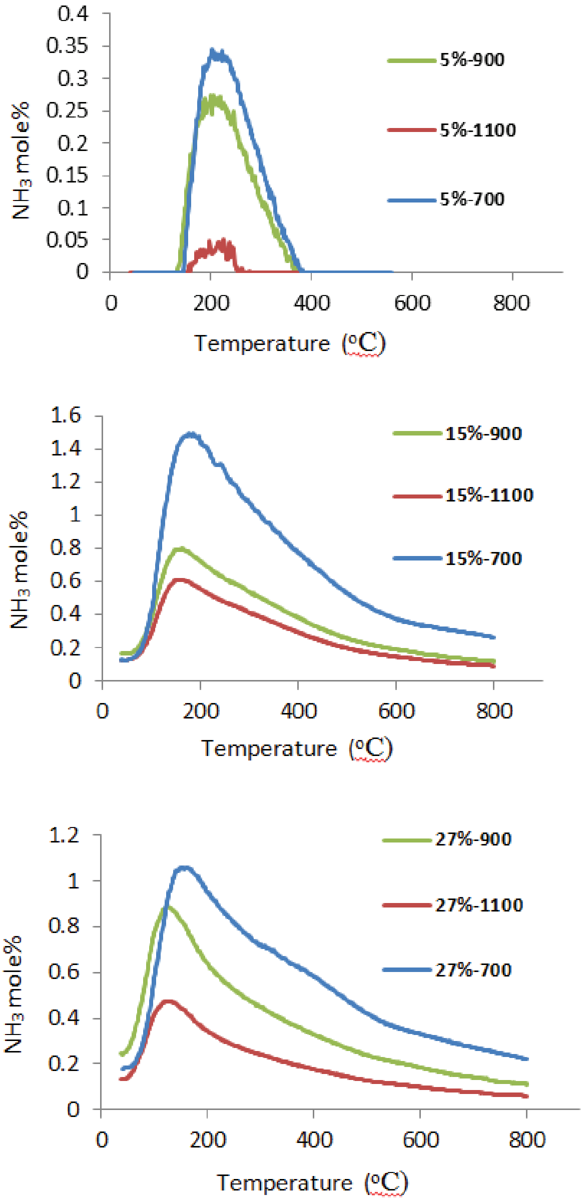

Figure 5.2: Ammonia-TPD measurements of different SDAs calcined at different temperatures for 2 h. a) 5% SDA. b) 15% SDA. c) 27% SDA.

(silica < 30%) at low temperature (500°C) (see Table 5.2) and showed a strong correlation of increasing acid site concentration with increasing Si/Al ratio for SDAs at low temperatures. The data show that this correlation extends to low silica compositions below 30% silica and at high temperatures.

5.5.1 Relationship between acid site concentrations and silica content

The ammonia-TPD data (Fig. 5.2 and Table 5.2) show that total acid site concentrations (Brϕnsted and Lewis) decrease in the order 27 > 15 > 5% at 700 and 900°C and is consistent with previously reported data at higher Si/Al ratios [34, 35, 43]. Low wt% silica doped alumina supports are favorable in many applications such as auto emission [2]. In addition, in a low Si to Al ratio support, Si enters tetrahedral vacancies in the defect spinel structure of alumina and stabilize the γ-Al_2O_3 phase (without mullite phase formation) to 1200°C. From the Brϕnsted acid site concentrations of other studies (Table 5.2), a trend is evident for calcination temperatures between 500-600°C where the Brϕnsted site concentration decreases to zero at low wt% Si; indeed, two previous studies report Brϕnsted acid site concentrations of zero for 3, 5, and 15% silica at low temperatures (500-600°C). However, the rates of some catalytic reactions such as isomerization and hydrocracking are proportional to the Brϕnsted acid site concentration. Perhaps the activity for Brϕnsted acid catalyzed reactions may also be close to zero. In contrast to previous studies, the Brϕnsted acid site concentrations of 5, 15, and 27% silica after calcination at 700°C reported here are not zero and only at high temperatures (1200°C) do the Brϕnsted acid site concentrations go to zero.

Figure 5.2 also shows that 5% SDA samples calcined at 700, 900, and 1100°C have no desorption peak above 370°C; however the 15% and 27% SDA samples calcined at 700, 900, and 1100°C have a desorption peak above 370°C. The shift of

Sample ID	Thermal treatment Temperature T°C / 2h	Al(IV) %	Al(V) %	Al (VI) %
Pure alumina	700	25	2	73
	1200	1	<1%	99
5% SDA	700	25	3	72
	900	27	1	72
	1100	32	<1%	68
	1200	32	<1%	68
15% SDA	700	25	36	39
	900	32	4	64
	1100	36	<1%	64
	1200	31	<1%	69
27% SDA	700	24	44	32
	900	27	19	54
	1100	31	<1%	69
	1200	31	<1%	69

SDA: silica-doped alumina

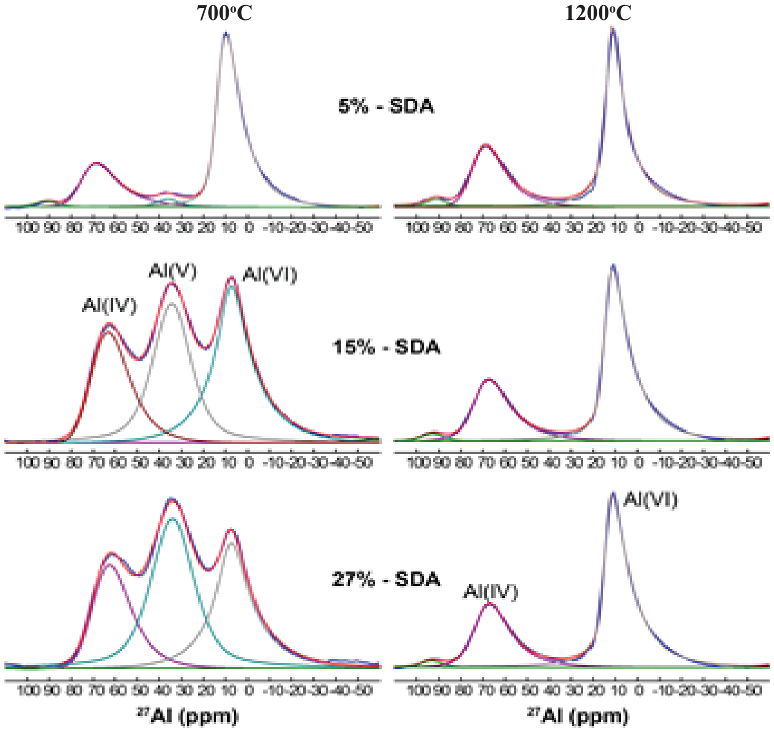

Figure 5.3: The 1D ^{27}Al MAS NMR spectra and relative compositions of 5-15-27% SDAs calcined at 700-1200C.

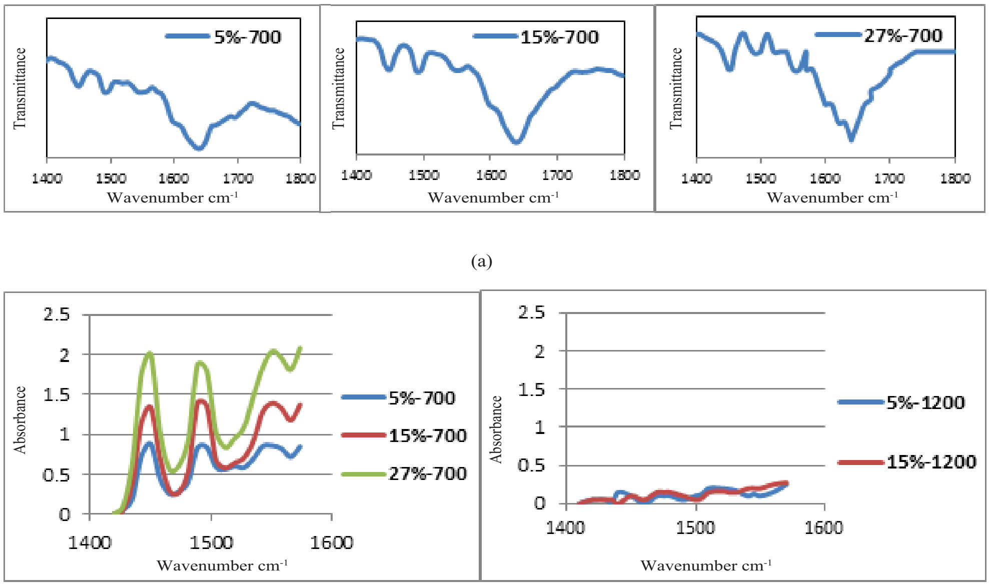

(a)

(b)

Figure 5.4: (a) IR transmittance spectra recorded after pyridine adsorption on 5-15-27% SDAs calcined at 700°C, (b) Absorption spectra after pyridine adsorption of 5, 15, 27% SDAs calcined at 700°C and 1200°C (in the range: 1432-1467 cm^{-1} (Brϕnsted sites) and 1516-1568 cm^{-1} (Lewis sites)).

the peak to a higher desorption temperature indicates an increase in acid strength of these sites [35].

Solid state ^{27}Al MAS NMR spectra (Fig. 5.3) show that the relative concentration of the Al(V) increases as silica content increases in the order $5 < 15 < 27\%$ for samples calcined at 700 and 900°C. The presence of Al(IV) and Al(V) are linked to weak and strong Lewis acid sites, respectively [38]. It has also been reported that the Lewis acid is stronger in highly unsaturated Al^{3+} sites (4- and 5-coordinated aluminum) and 5-coordinated aluminum is the strongest Lewis acid [12, 39]. The relative concentration of Al(V) is 3, 36, and 44% in 5, 15, and 27% SDA samples, respectively, consistent with the result from the ammonia-TPD data (Fig. 5.2 and Table 5.2).

The FTIR data (Fig. 5.4b and Table 5.2) shows that the absorbance intensity of peaks assigned to Brϕnsted and Lewis acid sites increased for the 5, 15, and 27% silica samples calcined at 700°C. The increase in the Brϕnsted acid concentration is largely due to bridged hydroxyl groups formation of Si-(OH)-Al [43].

Daniell et al. reported that two separate silica and alumina phases are observed in commercial 5% silica-doped alumina sample (Siral-5 from Sasol) [43]. In contrast, I have recently shown that 5% silica-doped alumina using solvent deficient method has a single alumina-silica phase and no separate silica phase [44]. The silica-alumina phase in the proposed SDA structure (discussed in Chapter 3) has 5-coordinated aluminum attributed to strong Lewis acid sites (see Fig. 5.3). In addition, the high charge and small Si radii can polarize OH to H^+, a process that can form stronger Brϕnsted acid sites. I suggest that the absence of a silica phase decreases the Brϕnsted acid site concentration and the presence of the alumina-silica phase increases the Lewis acid site concentration of 5% SDA compared to Siral-5.

5.5.2 Relationship between acid site concentrations and calcination temperature

Since previously published data indicate that the surface of silica doped alumina consists of silicon and aluminum oxides and since others have also shown new types of sites on amorphous alumino-silicates, e.g. Brϕnsted acid sites in the form of pseudo-bridging silanols [8, 45], it is unclear to what extent the acid properties of dilute silica-doped alumina will be similar to those previously reported for alumina [4,45,46]. The combination of TPD, FTIR, and NMR data of the present study provides new perspectives into the effects of dehydroxylation (calcination) temperature on the types and concentration of acid sites for silica-doped alumina.

(1) From ammonia-TPD data, the total acid site concentration (sum of Brϕnsted and Lewis acid sites) decreases for 5, 15, and 27% SDA samples (Fig. 5.2 and table 5.2) with increasing calcination temperature in the order of $700 < 900 < 1100$°C.

(2) From the FTIR data (Fig. 5.4b and table 5.2), peak intensities of pyridine adsorbed onto both Brϕnsted sites (1516-1568 cm^{-1}) and Lewis sites (1432-1467 cm^{-1}) decrease as the calcination temperature is increased from 700 to 1200°C for the 5, 15 and 27% silica samples. Moreover, Lewis and Brϕnsted acid site peaks are not observed, i.e., concentrations are negligible, after calcination at 1200°C.

(3) From the ^{27}Al NMR data (Fig. 5.3), 5-coordinated aluminum decreases from 700 to 1200°C in the 5, 15 and 27% silica samples. Aluminum atoms are mostly located in an octahedral environment Al(VI) at 1100 and 1200°C, suggesting the reduction of the Lewis acid site concentration [11].

Observations 1 and 2 indicate that diminishing O-H stretches corresponding to diminishing Lewis and Brϕnsted acid sites with increasing calcination temperature are correlated with removal of total acidity measured by ammonia adsorption for the dilute silica/aluminas of the present study. Observations 2 and 3 confirm a strong relationship between strong Lewis acid sites and 5-coordinated alumina for dilute silica/aluminas similar to that observed in previous studies of alumina [12, 38, 39]. Accordingly, the dilute silica/aluminas of this study have acid properties similar to those of gamma alumina.

Lowering the Lewis and Brϕnsted acid site concentrations is critical in a number of catalytic applications, and the results of this study indicate that acid site concentrations of dilute silica/aluminas can be substantially lowered by high temperature calcination and at sufficiently high temperature (e.g. 1200°C) reduced to zero. It is evident from previous work that aluminas and even some silica-doped aluminas could not be calcined above 1000°C due to decreases in surface area and porosity to unacceptably low values due to the $\alpha-Al_2O_3$ to $\theta-Al_2O_3$ transition. In contrast, the dilute-silica SDAs of this study retain the $\gamma-Al_2O_3$ phase, high surface area, large pore volume with production of uniquely large pores to temperatures as high as 1200°C, thus enabling removal of most or all of the surface hydroxyl groups associated with acid sites.

5.6 Conclusions

The acid site concentration (Brϕnsted and Lewis), intrinsic Lewis acid sites, and the acid site strength of thermally stable silica-doped alumina is controlled by changing the Si ratio (0 to 27%) and calcination temperature (700 to 1200°C) parameters while maintaining high surface areas, large pore volumes, and large pore diameters. The total acid site concentration (Lewis and Brϕnsted), intrinsic Lewis acid concentration, and acid strength are increased by increasing higher mole ratio of Si/Al. In addition, due to the high calcination temperature most of the acid sites (Lewis and Brϕnsted) are removed from SDA samples, which are ideal catalyst supports for Fischer-Tropsch synthesis.

Bibliography

[1] A. Corma, A. Martinez, V. Martinez-Soria, and J. B. Monton, "Hydrocracking of vacuum gas oil on the novel mesoporous mcm-41 aluminosilicate catalyst," *J. Catal.*, vol. 153, no. 1, pp. 25–31, 1995. 126

[2] C. H. Bartholomew and R. J. Farrauto, *Fundumentals of industrial catalytic processes*, 2nd ed. Hoboken, New Jersy,: John Wiley and Sons Inc., 2006. xii, 2, 41, 42, 81, 82, 126, 137

[3] C. P. Nicolaides, "A novel family of solid acid catalysts: substantially amorphous or partially crystalline zeolitic materials," *Appl. Catal., A*, vol. 185, no. 2, pp. 211–217. 126

[4] P. Raybaud and C. Chizallet, "Origin of the versatile Bronsted acidity of amorphous silica-alumina used as catalytic support in hydrocracking," *Abstracts of Papers, 240th ACS National Meeting, Boston, MA, United States, August 22-26, 2010*, pp. PETR–34, 2010. 126, 140

[5] H. Pines and W. O. Haag, "Alumina: Catalyst and support. i. alumina, its intrinsic acidity and catalytic activity," *J. Am. Chem. Soc.*, vol. 82, pp. 2471–83, 1960. 12, 70, 126

[6] B. Hu and I. D. Gay, "Acid sites on SiO_2-Al_2O_3 monolayer catalysts: 31P NMR probes of strength and accessibility," *J. Phys. Chem. B*, vol. 105, no. 1, pp. 217–219, 2001. 127

[7] E. J. M. Hensen, D. G. Poduval, D. A. J. M. Ligthart, J. A. R. van Veen, and M. S. Rigutto, “Quantification of strong Bronsted acid sites in aluminosilicates,” *J. Phys. Chem. C*, vol. 114, no. 18, pp. 8363–8374, 2010. 127

[8] F. Leydier, C. Chizallet, A. Chaumonnot, M. Digne, E. Soyer, A.-A. Quoineaud, D. Costa, and P. Raybaud, “Bronsted acidity of amorphous silica-alumina: The molecular rules of proton transfer,” *J. Catal.*, vol. 284, no. 2, pp. 215–229, 2011. 127, 140

[9] H. Ohkita, R. Nishiyama, Y. Tochihara, T. Mizushima, N. Kakuta, Y. Morioka, A. Ueno, Y. Namiki, S. Tanifuji, and et al., “Acid properties of silica-alumina catalysts and catalytic degradation of polyethylene,” *Ind. Eng. Chem. Res.*, vol. 32, no. 12, pp. 3112–16, 1993. xii, 127, 134, 135

[10] M. A. Rahman, M. A. K. Azad, S. Ahsan, S. Islam, M. A. Motin, and M. Asadullah, “Measurement of Bronsted acidity of silica-alumina solid catalyst by base exchange method,” *J. Surf. Sci. Technol.*, vol. 22, no. 1-2, pp. 25–33, 2006. 127, 128

[11] C. Belver, P. Aranda, M. A. Martin-Luengo, and E. Ruiz-Hitzky, “New silica/alumina-clay heterostructures: Properties as acid catalysts,” *Microporous Mesoporous Mater.*, vol. 147, no. 1, pp. 157–166, 2012. xii, 127, 128, 134, 141

[12] M. Digne, P. Sautet, P. Raybaud, P. Euzen, and H. Toulhoat, “Use of DFT to achieve a rational understanding of acid-basic properties of gamma-alumina surfaces,” *J. Catal.*, vol. 226, no. 1, pp. 54–68, 2004. 127, 135, 139, 141

[13] T. Jarecka and J. Datka, "Acid and catalytic properties of new thermostable sulfocationic exchangers supported on aluminosilicates," *Appl. Catal., A*, vol. 184, no. 2, pp. 203–209, 1999. 127

[14] M. Bartoszek, R. Eckelt, C. Jaeger, H. Kosslick, A. Pawlik, and A. Schulz, "Mesoporous silica-aluminas derived from precipitation: a study of the acidity, textural properties and catalytic performance," *J. Mater. Sci.*, vol. 44, no. 24, pp. 6629–6636, 2009. 127

[15] A. K. Bandopadhyay, J. Das, and S. K. Roy, "Effect of quaternary ammonium compounds on the physicochemical properties of amorphous silica-alumina," *J. Catal.*, vol. 124, no. 1, pp. 241–6, 1990. 127

[16] R. J. Gorte, "What do we know about the acidity of solid acids?" *Catal. Lett.*, vol. 62, no. 1, pp. 1–13, 1999. 127

[17] V. C. F. Holm, G. C. Bailey, and A. Clark, "Acidity studies of silica-alumina catalysts," *J. Phys. Chem.*, vol. 63, pp. 129–33, 1959. xii, 127, 128, 134

[18] M. A. Rahman, M. R. Zaman, and K. Biswas, "Estimation of surface acidity of silica-alumina catalysts by amine titrations," *Bangladesh J. Sci. Ind. Res.*, vol. 32, no. 2, pp. 226–229, 1997. 127

[19] S. He, C. Sun, Z. Bai, X. Dai, and B. Wang, "Dehydrogenation of long chain paraffins over supported $\mathrm{Pt-Sn-K}_{/}\mathrm{Al_2O_3}$ catalysts: A study of the alumina support effect," *Appl. Catal., A*, vol. 356, no. 1, pp. 88–98, 2009. 127

[20] A. A. Shutilov, G. A. Zenkovets, S. V. Tsybulya, and V. Y. Gavrilov, "Effect of silica on the stability of the nanostructure and texture of fine-particle alumina," *Kinet. Catal.*, vol. 53, no. 1, pp. 125–136, 2012. xii, 19, 20, 71, 72, 82, 88, 128

[21] J. W. Curley, M. J. Dreelan, and O. E. Finlayson, “High temperature stability of alumina fiber,” *Catal. Today*, vol. 10, no. 3, pp. 401–4, 1991. 19, 20, 71, 82, 99, 128

[22] T. Fukui and M. Hori, “Control of micropore size distribution in alumina by the hydrothermal treatment of an alkoxide derived-alcogel,” *J. Mater. Sci.*, vol. 31, no. 12, pp. 3245–3248, 1996. 85, 99, 128

[23] A. W. Espie and J. C. Vickerman, “Aluminas modified with silica. part 1. An X-ray diffraction and secondary-ion mass spectrometry study of the influence of preparation and thermal treatment on structure and surface composition,” *J. Chem. Soc., Faraday Trans. 1*, vol. 80, no. 7, pp. 1903–13, 1984. 19, 20, 71, 128

[24] T. Osaki, K. Nagashima, K. Watari, and K. Tajiri, “Silica-doped alumina cryogels with high thermal stability,” *J. Non-Cryst. Solids*, vol. 353, no. 24-25, pp. 2436–2442, 2007. xii, 19, 20, 71, 72, 82, 88, 128

[25] T. Horiuchi, L. Chen, T. Osaki, T. Sugiyama, K. Suzuki, and T. Mori, “A novel alumina catalyst support with high thermal stability derived from silica-modified alumina aerogel,” *Catal. Lett.*, vol. 58, no. 2,3, pp. 89–92, 1999. 128

[26] L. L. L. Prado, P. A. P. Nascente, S. C. De Castro, and Y. Gushikem, “Aluminium oxide grafted on silica gel surface: Study of the thermal stability, structure and surface acidity,” *J. Mater. Sci.*, vol. 35, no. 2, pp. 449–453, 2000. 86, 128

[27] E. J. M. Hensen, D. G. Poduval, P. C. M. M. Magusin, A. E. Coumans, and J. A. R. van Veen, “Formation of acid sites in amorphous silica-alumina,” *J. Catal.*, vol. 269, no. 1, pp. 201–218, 2010. 128

[28] T. Barzetti, E. Selli, D. Moscotti, and L. Forni, “Pyridine and ammonia as probes for ftir analysis of solid acid catalysts,” *J. Chem. Soc., Faraday Trans.*, vol. 92, no. 8, pp. 1401–1407, 1996. 128, 132, 135

[29] N. Yao, K. L. Yeung, and G. Xiong, “Nanoscale observation of morphological transformation during ageing of silica and silica-alumina,” *J. Sol-Gel Sci. Technol.*, vol. 39, no. 2, pp. 139–150, 2006. 128

[30] B. Huang, C. H. Bartholomew, and B. F. Woodfield, “Improved calculations of pore size distribution for relatively large, irregular slit-shaped mesopore structure,” *Microporous and mesoporous materials*, 2013. 103, 131, 168

[31] R. J. Gorte, “Temperature-programmed desorption for the characterization of oxide catalysts,” *Catal. Today*, vol. 28, no. 4, pp. 405–414, 1996. 131

[32] D. R. Neuville, L. Cormier, and D. Massiot, “Al environment in tectosilicate and peraluminous glasses: A 27Al MQ−MAS NMR, Raman, and XANES investigation,” *Geochimica et Cosmochimica Acta*, vol. 68, no. 24, pp. 5071–5079, 2004. 75, 133

[33] P. Naidoo, “Si surface doping of the activated pre-shaped Al_2O_3 support,” Report, 2012. xii, 134

[34] N. Yao, G. Xiong, M. He, S. Sheng, W. Yang, and X. Bao, “A novel method to synthesize amorphous silica-alumina materials with mesoporous distribution without using templates and pore-regulating agents,” *Chem. Mater.*, vol. 14, no. 1, pp. 122–129, 2002. xii, 134, 135, 137

[35] A. M. Camiloti, S. L. Jahn, N. D. Velasco, L. F. Moura, and D. Cardoso, “Acidity of beta zeolite determined by tpd of ammonia and ethylbenzene disproportionation,” *Appl. Catal., A*, vol. 182, no. 1, pp. 107–113, 1999. 133, 135, 137, 139

[36] H. Yong, D. Coster, F. R. Chen, J. G. Davis, and J. J. Fripiat, “Aluminum coordination and Lewis acidity in aluminas and steamed zeolites,” *Stud. Surf. Sci. Catal.*, vol. 75, no. New Frontiers in Catalysis, Pt. B, pp. 1159–70, 1993. 81, 135

[37] W. E. E. Stone, G. M. S. El Shafei, J. Sanz, and S. A. Selim, “Association of soluble aluminum ionic species with a silica-gel surface: a solid-state nmr study,” *J. Phys. Chem.*, vol. 97, no. 39, pp. 10 127–32, 1993. 81, 135

[38] F. R. Chen, J. G. Davis, and J. J. Fripiat, “Aluminum coordination and Lewis acidity in transition aluminas,” *J. Catal.*, vol. 133, no. 2, pp. 263–78, 1992. 135, 139, 141

[39] X. Liu and R. E. Truitt, “Drft-ir studies of the surface of -alumina,” *J. Am. Chem. Soc.*, vol. 119, no. 41, pp. 9856–9860, 1997. 12, 70, 135, 139, 141

[40] E. P. Parry, “An infrared study of pyridine adsorbed on acidic solids. characterization of surface acidity,” *J. Catal.*, vol. 2, no. 5, pp. 371–9, 1963. 135

[41] J.-C. Lavelley, R. Anquetil, J. Czyzniewska, and M. Ziolek, “Use of pyridine as a probe for the determination, by ir spectroscopy, of the broensted acid strength of mihnay zeolites,” *J. Chem. Soc., Faraday Trans.*, vol. 92, no. 7, pp. 1263–6, 1996. 135

[42] J. B. Breen, C. Breen, and J. Yarwood, "In situ determination of Bronsted/Lewis acidity on cation-exchanged clay mineral surfaces by ATR−IR," *Clay Miner.*, vol. 31, no. 4, pp. 513–522, 1996. 135

[43] W. Daniell, U. Schubert, R. Glockler, A. Meyer, K. Noweck, and H. Knozinger, "Enhanced surface acidity in mixed alumina-silicas: a low-temperature FTIR study," *Appl. Catal., A*, vol. 196, no. 2, pp. 247–260, 2000. 86, 135, 137, 140

[44] M. K. Mardkhe, B. Huang, C. H. Bartholomew, T. M. Alam, and B. F. Woodfield, "The origin of increased thermal stability for Si doped alumina," *Microporous Mesoporous Materials*, vol. To be submitted, 2013. 140

[45] H. Knozinger and P. Ratnasamy, "Catalytic alumina: surface models and characterization of surface sites," *Catal. Rev. Sci. Eng.*, vol. 17, no. 1, pp. 31–70, 1987. 140

[46] M. Trueba and S. P. Trasatti, "Gamma alumina as a support for catalysis: a review of fundamental aspects," *Eur. J. Inorg. Chem.*, pp. 3393–3403, 2005. 140

Chapter 6

Generalized preparation method and characterization of aluminum isopropoxide, aluminum phenoxide, and aluminum *n*-hexyloxide

6.1 Introduction

Metal alkoxides are used to make Al_2O_3 (alumina) catalyst supports for a wide range of applications, including hydrocracking and Fischer-Tropsch (FT) catalysis [1–4]. Unlike metal nitrates and chlorides, metal alkoxides are easily purified; they hydrolyze to produce hydrated oxides with no anionic contaminations [4]. Properties of alumina, notably surface area and pore size, depend on a number of factors, including the nature of the aluminum alkoxide starting material [5–7]. Since the identity of parent alkoxide influences the catalytic properties of the alumina support, it is important to develop an efficient method to synthesize different aluminum alkoxides.

The physical properties of metal alkoxides vary with the electronegativity and coordination number of the metal, as well as the nature of the attached alkyl group [4], where the identity of the parent alcohol influences the electronic and steric properties of the alkoxide. This, in turn, modifies the structure of the corresponding alkoxide [5].

Many studies have been performed focusing on the preparation of alumina with selected properties such as particle size, surface area, pore volume, and pore diameter, using aluminum isopropoxide [3, 8–12], aluminum sec-butoxide [3, 13–15], aluminum ethoxide [3], and aluminum phenoxide [5]. We have previously [16, 17] designed nano alumina supports with high surface areas (150 to 350 m^2/g) and large pore sizes (13 to 20 nm) using various aluminum alkoxides. Here I report a generalized method to synthesize aluminum alkoxides, which can be employed as starting materials for the production of alumina based catalyst supports.

Aluminum alkoxides contain acceptor and donor centers and exist as monomers, dimers, trimers and tetramers with various coordination numbers (Fig. 6.11). The oligomerization is inversely depended on the steric demand of the R group attached to the oxygen [5]. Al^{+3} can form four-, five-, and six-coordinated complexes. The structure of aluminum ethoxide is polymeric, containing five-coordinated aluminum [18]. Aluminum tert-butoxide is dimeric containing aluminum with a coordination number of four [18]. Aluminum isopropoxide exists as a trimer in freshly prepared samples or as a tetramer in aged samples [18,19]. The coordination numbers of aged AIP can be six and four [20]. Aluminum phenoxide has been reported to be a trimer containing aluminum with coordination numbers of four and five [21]. Different coordination numbers of aluminum are also reported in di-, tri-, tetra-, and polynuclear aluminum alkoxides [5, 22–25].

Aluminum alkoxides can be produced without using a catalyst, but the reaction rates are very slow and thus aluminum alkoxides are more efficiently formed using three equivalents of anhydrous alcohol with one equivalent of metal in the presence of 1 mol% $HgCl_2$ as catalyst Eq. 6.1.

$$\mathrm{Al} + 3\mathrm{ROH} \xrightarrow{0.01\mathrm{HgCl_2}} \mathrm{Al(OR)_3} + \tfrac{3}{2}\mathrm{H_2} \tag{6.1}$$

This reaction has been widely used to make simple alkoxides, including aluminum isopropoxide and aluminum ethoxide. In these cases, this route has become a well-known industrial process [2,2,4,7,26]. Tomar and Yoo [2,5] recently reported approaches to aluminum phenoxide and aluminum isopropoxide through this process as well.

The surface of elemental aluminum is covered by a oxide layer, thus it is thought $HgCl_2$ will activate this surface and accelerate the reaction kinetics [7]. The $HgCl_2$ initially reacts with aluminum to produce the Al^{+3} ion, which then reacts with the alcohol to form the alkoxide adduct. I have optimized the process by lowering the reaction time and the concentration of $HgCl_2$ to obtain improvements in yield, which now allows for a complete characterization of these useful products. Optimum conditions include use of excess alcohol and a lower amount of mercuric chloride catalyst [2,5,7,20].

This chapter reports a generalized preparation and characterization of divergent aluminum alkoxide structures including aluminum isopropoxide ($R{=}C_3H_7$), aluminum phenoxide ($R{=}C_6H_5$), and aluminum *n*-hexyloxide ($R{=}C_6H_{13}$). Notably, the approach allows for the first generalized synthesis and characterization of aluminum *n*-hexyloxide. Synthesis of aluminum *n*-hexyloxide from 1-hexanol is significant in that this alkoxide possesses low water, high stability, and efficient reactivity for the production of aluminum oxide nanomaterials. I selected aluminum isopropoxide, aluminum phenoxide, and aluminum *n*-hexyloxide, as a general representation of steric bulk since the A-values of attached alkyl groups are different for each group. Isopropyl=2.15 Kcal/mol, phenyl=2.7 Kcal/mol, ethyl (analogue of *n*-hexyl)=1.75 Kcal/mol [27]. The effect of ligand environment on the physiochemical properties of aluminum alkoxides influences the properties of the alumina [3,10,28]. The structure and properties of aluminas produced from these aluminum alkoxides with different steric characteristics can now be produced and studied using the reported method.

6.2 Experimental

6.2.1 Materials

The aluminum *n*-hexyloxide (AH) was prepared from the reaction of aluminum (granular, Spectrum, 99.6%) and 1-hexanol (anhydrous, Alfa-Aesar, 99.0%) in the presence of $HgCl_2$ (Fisher, 100.0%) as a catalyst. Aluminum phenoxide (APh) was prepared from aluminum (granular, Spectrum, 99.6%) and phenol (detached crystals, Alfa-Aesar, >99%) in the presence of $HgCl_2$ (Fisher, 100.0%) as catalyst and dried THF (EMD, 99.99%) as solvent. Aluminum isopropoxide (AIP) was prepared from aluminum (granular, Spectrum, 99.6%) and isopropyl alcohol (Sigma-Aldrich, >99.8%) in the presence of $HgCl_2$ (Fisher, 100.0%) as catalyst. HNO_3 (EMD, 70%-Omni Trace) was used to dissolve samples for ICP-MS experiment.

6.2.2 Equipment

AH, AIP and APh were characterized by IR, NMR, ICP and elemental analysis. To obtain IR spectra, nujol mulls of the solid alkoxides were analyzed with a Nicolet (Avatar 360) spectrophotometer. Elemental analysis was performed (Galbraith Laboratory) for AH, APh and AIP separately using a C, H, O combustion method. The structure of the synthesized aluminas were determined by powder X-ray diffraction (XRD) using a PANalytical X'Pert Pro diffractrometer with a Cu Kα X-ray source ($\lambda = 1.5418$ Å) operated at 45 kV and 40 mA. Scans were performed between 10° and 90° 2θ with a step size of 0.0167° at a rate of $0.013°s^{-1}$. The Scherrer formula was used to estimate crystallite size [29]. ^{1}H NMR, ^{13}C NMR and ^{27}Al

NMR were collected on a Varian NMR-S 500MHz instrument using a pfg-enabled dual-broadband probe. The ^{1}H NMR, gCOSY, ^{13}C NMR, and ^{27}Al NMR spectrum of AIP, and AH were recorded with benzene-d6 as solvent. The spectrum of APh was recorded with DMSO-d6 and methanol-d4 as solvent. All samples were prepared and measured at ambient temperature 25°C. I used ICP-MS (Elan 6000, Perkin Elmer) to determine levels of Hg impurity of synthesized alkoxides. A standard method, TotalQuant, was used to measure concentration of mercury in samples. 2% nitric acid was used to dilute and dissolve the alkoxides followed by 30 minutes sonicating using Branson 1510 sonicator. Nitrogen adsorption measurements were carried out using a Micromeritics Tristar 3020 for the determination of surface properties at -196°C. Surface area was calculated using the Brunauner-Emmett-Teller (BET) model in the P/P_0 range from 0.05 to 0.20. Samples were degassed at 200°C under N_2 flow overnight before every measurement.

6.3 Synthesis

6.3.1 General procedure

To ensure an anhydrous environment, solvent and alcohols were dried over molecular sieves. The flask was fitted with a condenser and a $CaCl_2$ tube. A sand bath and heat regulator were used to provide homogenous heating for the reactions. One mole of aluminum was treated with excess alcohol in the presence of catalytic mercuric chloride (0.001 mole) and refluxed. Vacuum distillation was applied to remove un-reacted alcohol and solvent in the case of APh and un-reacted alcohol in the case of AIP and AH. AIP was purified by further vacuum distillation. However, APh and AH were collected without further vacuum distillation since they were

Table 6.1: Synthesis conditions to produce APh, AH, and AIP.

Product	Aluminum mole	Alcohol mole	$HgCl_2$ mole	Reflux time (h)	Solvent
APh	1	4.3 (Phenol)	0.001	24	THF
AH	1	7.9 (Hexanol)	0.001	11	-
AIP	1	8.3 (Isopropanol)	0.001	9	-

shown to decompose upon heating. Experimental conditions to synthesize aluminum alkoxides are shown in Table 6.1.

6.3.2 Synthesis of aluminum *n*-hexyloxide (AH)

Al (1 mole) was added to excess 1-hexanol (7.9 mole) and (0.001 mole) $HgCl_2$ in a flask. The mixture was refluxed for 11 h under N_2 atmosphere with stirring then the solution was allowed to cool overnight without stirring. Since AH decomposed on vacuum distillation, it was collected from the top layer of the flask and vacuum filtered with a Buchner funnel using filter paper (Fisher, P_4). ^{1}H NMR (C_6H_6): δ 0.8 (t, 3H, JCH = 6.97, 7.22 Hz, CH_3), 1.1 (m, 6H, CH_2), 1.3 (m, 2H, CH_2), 3.2 (m, 2H, CH_2). ^{13}C NMR (C_6H_6): δ 13.87 (s, CH_3), 22.64 (s, CH_2), 25.44 (s, CH_2), 31.62 (s, CH_2), 32.77 (s, CH_2), 62.34 (s, CH_2). ^{27}Al NMR (C_6H_6): δ 56.5 (s, 4 or 5 coordinated Al). XRD (γ-alumina at 1000°C): 2θ 25.7, 35.2, 37.9, 43.5, 52.6, 57.6, 60.1, 61.5. IR (Nujol, Al-O-C, cm^{-1}): 1055.80 cm^{-1}.

6.3.3 Synthesis of aluminum phenoxide (APh)

Al (1 mole) was added to excess phenol (4.3 mole), in 2 liter dried THF (solvent) and (0.001 mole) $HgCl_2$ in a flask [5]. The mixture was refluxed for 24 h under a N_2 atmosphere with stirring. Solvent and alcohol were removed by vacuum distillation. Aluminum phenoxide was not extracted by further vacuum distillation since it decomposes on heating and was collected from the flask [5]. ^{1}H NMR (DMSO and methanol): δ 6.73 (m, 3H, CH), 7.12 (m, 2H, CH). ^{13}C NMR (DMSO and methanol): δ 115.55 (s, 2H, CH), 119.22 (s, 2H, CH), 129.77 (s, 1H, CH), 157.63 (s, qC). ^{27}Al NMR (DMSO and methanol): δ 56.5 (s, 4 or 5 coordinated Al). XRD (γ- and α-alumina at 1000°C): 2θ 25.7, 35.2, 37.9, 43.5, 52.6, 57.6, 60.1, 61.5, 19.5, 32, 37.7, 39.5, 45.8, 60.5. IR (nujol, Al-O-C, cm^{-1}): 1070.75 cm^{-1}.

6.3.4 Synthesis of aluminum isopropoxide (AIP)

Al (1 mole) was added to excess isopropyl alcohol (8.3 mole) and (0.001 mole) $HgCl_2$ in a flask. The mixture was refluxed for 9 h under N_2 atmosphere with stirring. Afterward, vacuum distillation was applied to remove the un-reacted alcohol. Further vacuum distillation was applied to collect the viscous AIP from the flask. Freshly prepared AIP was aged to a white powder after two days. ^{1}H NMR (C_6H_6): δ 0.92 (d, 3H, JCH = 4.39 Hz, terminal-CH_3), 1.66 (d, 6H, JCH = 6.23 Hz, bridge-CH_3), 4.4 (h, 2H, terminal-CH), 4.6 (h, 2H, bridge-CH). ^{27}Al NMR (C_6H_6): δ 56.5 (s, 4 coordinated Al), 3.5(s, 6 coordinated Al). XRD (γ alumina at 1000°C): 2θ 25.7, 35.2, 37.9, 43.5, 52.6, 57.6, 60.1, 61.5. IR (nujol, Al-O-C, cm^{-1}): 1033 cm^{-1}.

6.3.5 Synthesis of nanosized alumina

The auminas were prepared via a facile solvent deficient method [6] that involves mixing aluminum alkoxide and water at a 5:1 mole ratio of water to aluminum alkoxide. This precursor was mixed for 30 minutes followed by a thermal treatment at 550°C and 1000°Cfor 2 h each with 5 h ramps. The $Al(OH)_3$ precursor decomposes leading to the formation of water and nano crystalline Al_2O_3 and all of the byproducts are released as gases.

6.4 Results and Discussion

Since aluminum alkoxides are sensitive to trace amounts of water and decompose to alcohol and water, all steps were performed under an inert nitrogen atmosphere. Reaction times and reactant concentrations were varied to improve the yields. Aluminum *n*-hexyloxide was obtained in 95% yield. Aluminum phenoxide was synthesized in 90-95% yield and aluminum isopropoxide was produced in 95% yield. Some alkoxides (such as AH and APh) decompose without melting at high temperature but others can sublime without decomposition (such as AIP) [5].

6.4.1 FTIR

Figure 6.1 shows the FT-IR spectra for AIP, AH, and APh. The absorption peaks in IR spectra confirm conversion of the alcohol peak around 3500 cm^{-1} to alkoxide peaks. The Al-O-C bond stretch of aluminum alkoxides appears at 1030-1080 cm^{-1} and the Al-O-Al bond shows absorption between 945 to 980 cm^{-1} as reported earlier [2, 5, 30].

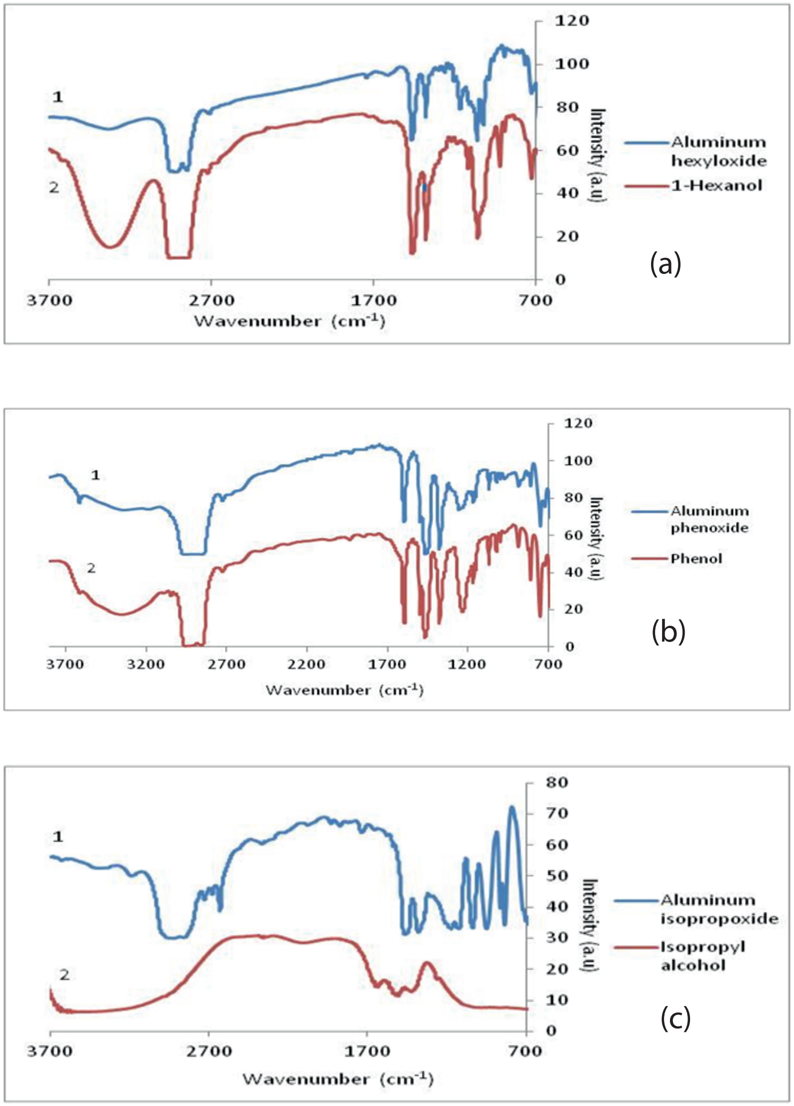

Figure 6.1: IR spectra of (a) aluminum *n*-hexyloxide and 1-hexanol, (b) aluminum phenoxide and phenol, and (c) aluminum isopropoxide and 2-propanol.

6.4.2 NMR

The aluminum *n*-hexyloxide ^{1}H NMR (Figure 6.2a) spectrum shows a triplet at 0.8 ppm due to a methyl group (C_6), a multiplet at 1.1 ppm due to (C_4,C_5,C_3), a multiplet at 1.3 ppm due to C_2 and a doublet of a triplet at 3.2 ppm due to C_1 attached to oxygen. The triplet appearing at 0.47 ppm was unexpected. Both the J-splitting in the ^{1}H NMR and the cross-peaks in the gCOSY show that these peaks are correlated with the signal at 3.2 ppm (Figures 6.2, 6.3). Given the relative intensity of 2:1 and the fact that this is coupled with C_1 suggests that there is a hydrogen attached to the oxygen of each alkoxide. This is not a signal from water as that appears at 0.41 in benzene-d6 and water would not show J-coupling to the methylene at C_1. This is also not free 1-hexanol in solution; as Figure 6.2b compares aluminum *n*-hexyloxide and 1-hexanol in benzene-d6. The C_1, C_2 and C_3 hydrogens of aluminum *n*-hexyloxide are clearly shifted upfield due to the interaction of the oxygen atom with the aluminum. Furthermore, the alcohol peak in 1-hexanol is shifted approximately 3 ppm downfield relative to the hydroxyl peak in aluminum *n*-hexyloxide. Aluminum *n*-hexyloxide ^{13}C NMR shows peaks at 13.87, 22.64, 25.44, 31.62, 32.77 and 62.34 ppm corresponding to all six carbons in the alkyl chain (Figure 6.4).

The aluminum phenoxide ^{1}H NMR showed two peaks with relative intensities of 3:2 at 6.73 and 7.12 ppm, respectively. The signal at 6.73 ppm corresponds to the meta C_3 and para C_4 hydrogens. 7.12 ppm corresponds to the ortho C_2 which is consistent with previously reported spectra [5]. Signals at 2.483, 3.498 and 4.077 were due to solvents (Figure 6.5). Aluminum phenoxide ^{13}C NMR shows four peaks at 115.55, 119.22, 129.77 ppm due to C_2, C_3 and C_4 carbons and one peak at 157.63 due to quaternary carbon C_1. Signals at 47.9 and 39.9 are due to solvents (Figure

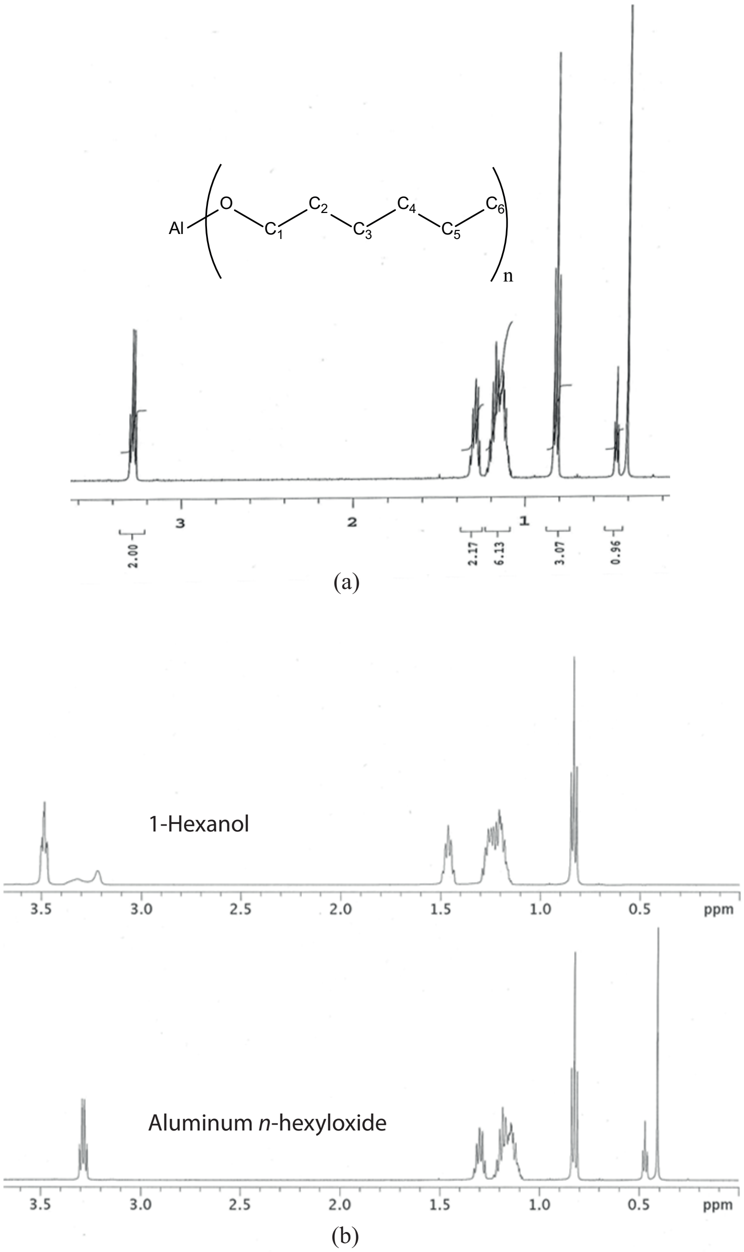

Figure 6.2: (a)^{1}H NMR of aluminum *n*-hexyloxide, and (b) ^{1}H NMR of aluminum *n*-hexyloxide and 1-hexanol comparison.

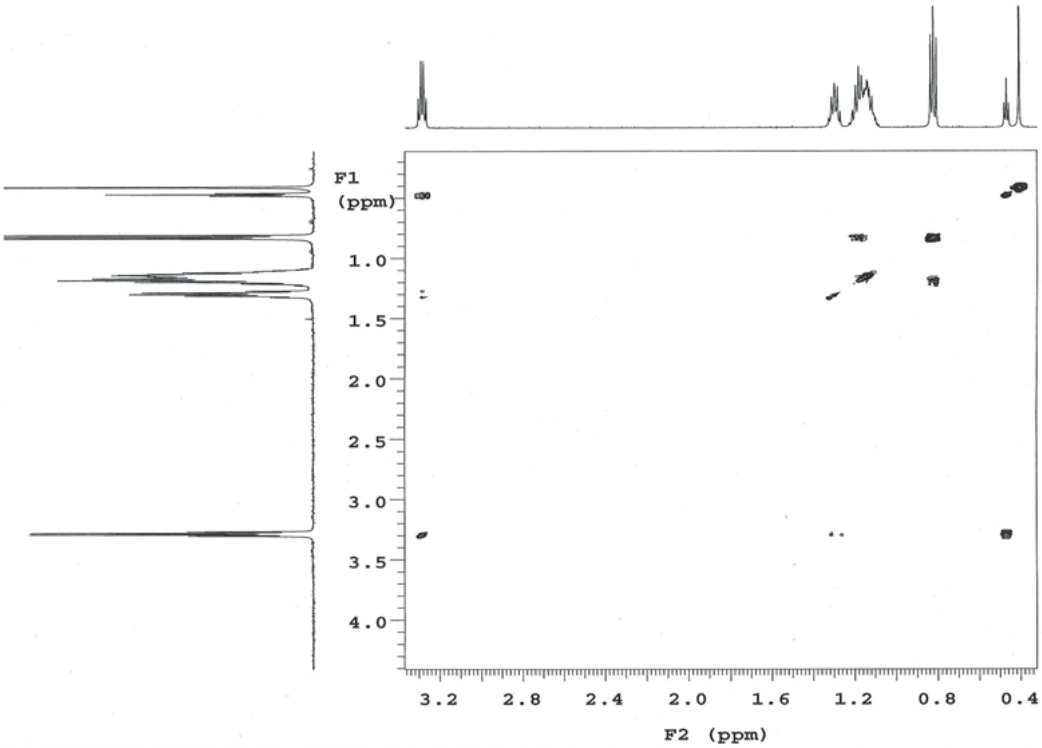

Figure 6.3: gCOSY of aluminum *n*-hexyloxide.

6.6). The ^{1}H NMR of freshly distilled aluminum isopropoxide showed a doublet at 1.04 ppm due to CH_3 and a heptet at 3.8 ppm due to the CH group. The alcohol signal comes at 3.4 ppm (Figure 6.7). Aged aluminum isopropoxide ^{1}H NMR showed two high field doublets at 0.92 and 1.66 ppm due to the terminal and bridged CH_3 respectively and two lower field heptets at 4.4 and 4.6 ppm due to terminal and bridged CH, respectively. Signals at 3.6, 1.2 and 1.3 result from residual isopropyl alcohol (Figure 6.8).

Aluminum phenoxide, freshly prepared aluminum isopropoxide, and aluminum *n*-hexyloxide ^{27}Al NMR all showed one broad peak at 50 ppm that is consistent with

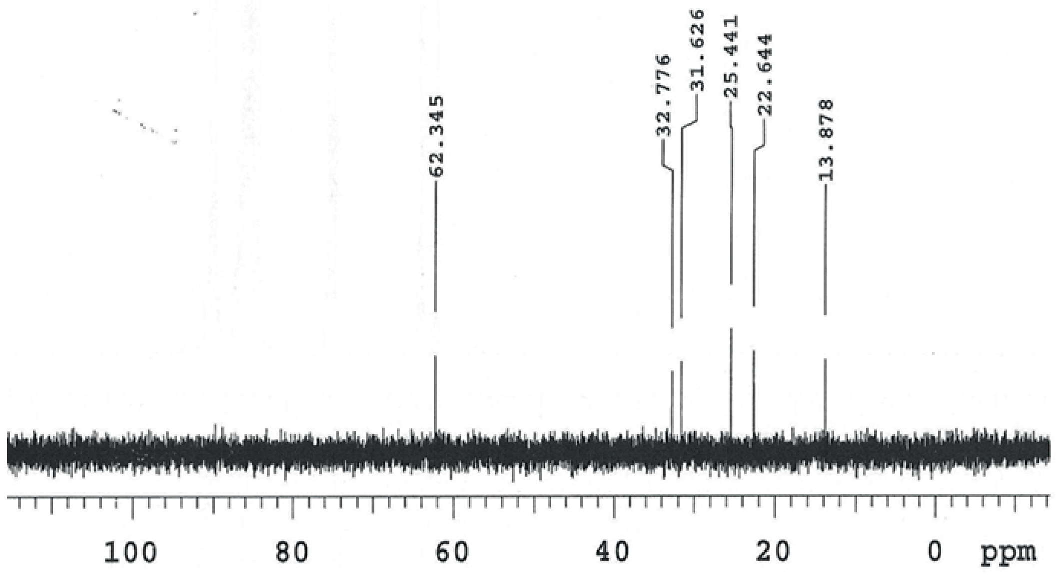

Figure 6.4: ^{13}C NMR of aluminum n-hexyloxide.

tetra and penta-coordinated Al (Figure 6.9). The lack of an intense signal at 3.50 ppm is consistent with the absence of hexa-coordinated Al in these structures. Aged aluminum isopropoxide ^{27}Al NMR showed one broad peak at 50 ppm that indicates tetra-and penta-coordinated Al. The sharp signal at 3.50 ppm (Figure 6.10) indicates the presence of hexa-coordinated aluminum (octahedral environment) [19, 31].

All measurements indicate that synthesized aluminum alkoxide with Al(OR)$_3$ units oligomerized differently. Aluminum coordination number is 4 (Figure 6.11a) or 5 (Figure 6.11b) in APh, AH, and fresh AIP. However, the coordination number of freshly distilled AIP increases to six (Figure 6.11c) as the alkoxide ages [32]. Aged AIP with high donor properties of oxygen of the alkoxy group (-OR) allows for formation of an oxygen bridged or polymeric structure with the attached oxygen

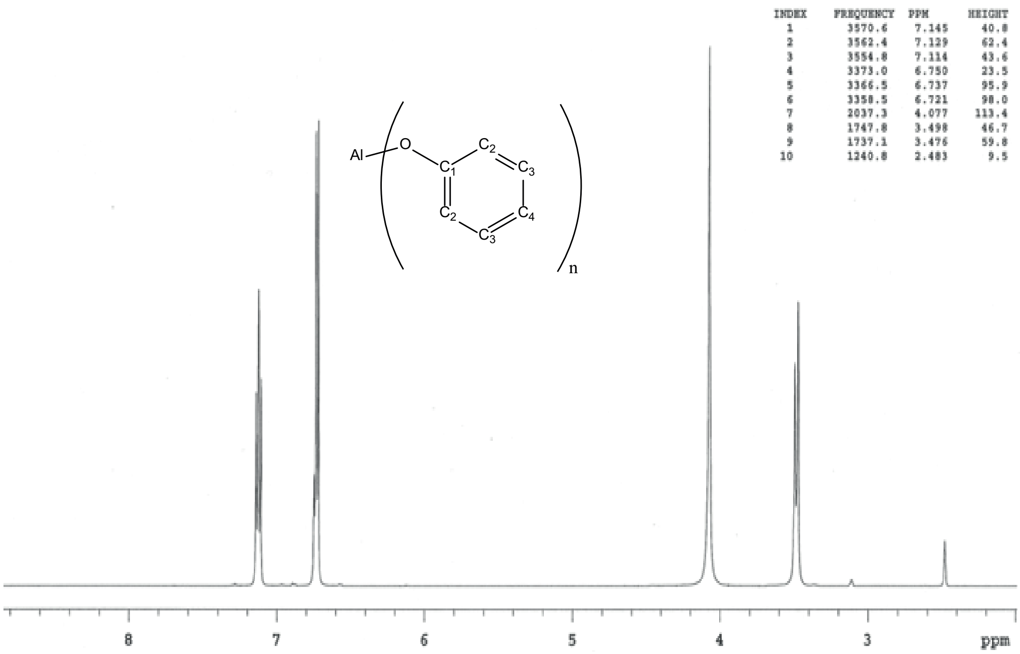

INDEX	FREQUENCY	PPM	HEIGHT
1	3570.6	7.145	40.8
2	3562.4	7.129	62.4
3	3554.8	7.114	43.6
4	3373.0	6.750	23.5
5	3366.5	6.737	95.9
6	3358.5	6.721	98.0
7	2037.3	4.077	113.4
8	1747.8	3.498	46.7
9	1737.1	3.476	59.8
10	1240.8	2.483	9.5

Figure 6.5: ^{1}H NMR of aluminum phenoxide.

functionality adopting a tetrameric structure. When the R group decreases donor-acceptor properties it leads to lower coordinated structures.

6.4.3 XRD

Figure 6.12 shows the XRD patterns of alumina samples obtained by calcinations of the synthesized aluminum alkoxides at different temperatures. Figure 6.12a shows powder X-ray diffraction patterns of aluminum phenoxide after calcination at 550°C for 2 hours. The peaks for all the calcined aluminum alkoxides are very broad, indicating that they are not crystalline. The particle sizes for these aluminas are less than 2 nm, based on the calculation from peak broadening using Scherrer formula [29]. Figure 6.12b shows XRD patterns of aluminum phenoxide at

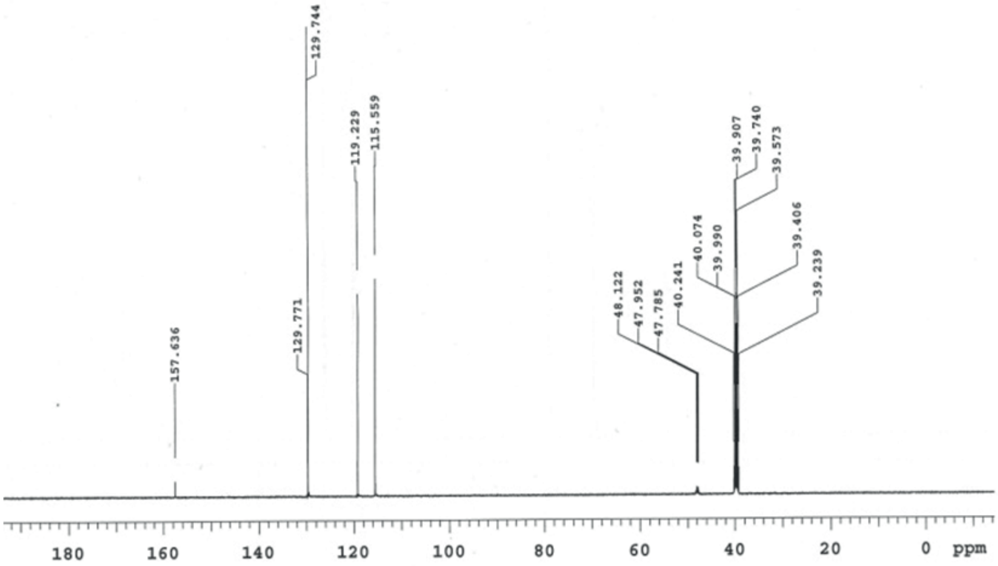

Figure 6.6: ^{13}C NMR of aluminum phenoxide.

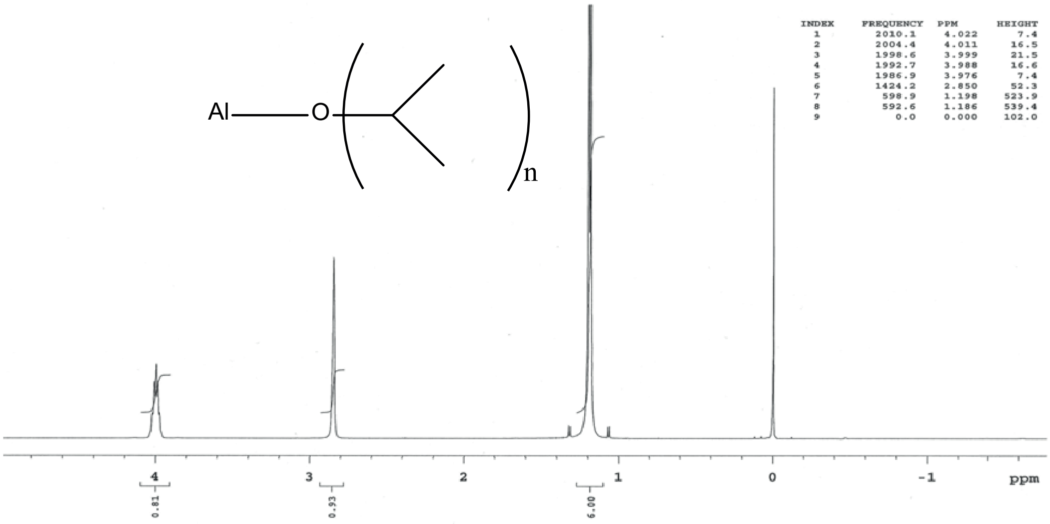

```
INDEX   FREQUENCY  PPM     HEIGHT
  1       2010.1   4.022      7.4
  2       2004.4   4.011     16.5
  3       1998.6   3.999     21.5
  4       1992.7   3.988     16.6
  5       1986.9   3.976      7.4
  6       1424.2   2.850     52.3
  7        598.9   1.198    523.9
  8        592.6   1.186    539.4
  9          0.0   0.000    102.0
```

Figure 6.7: ^{1}H NMR of freshly distilled aluminum isopropoxide.

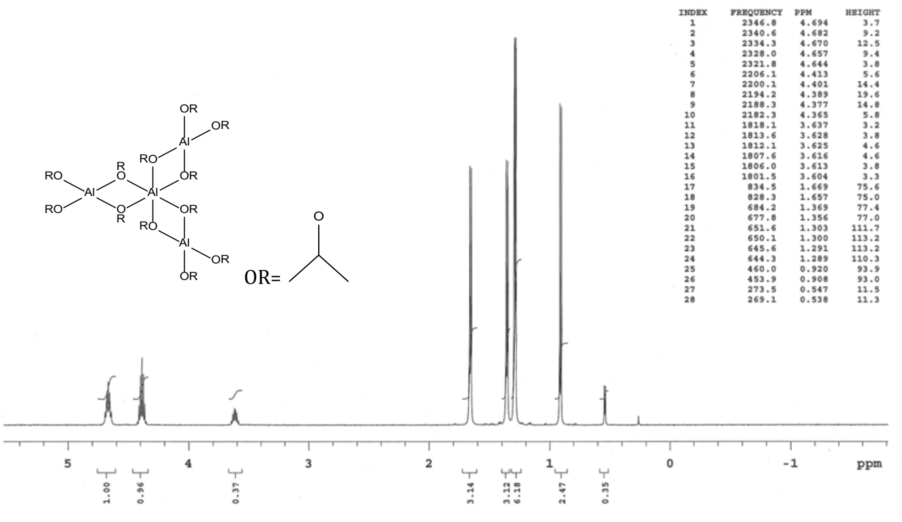

INDEX	FREQUENCY	PPM	HEIGHT
1	2346.8	4.694	3.7
2	2340.6	4.682	9.2
3	2334.3	4.670	12.5
4	2328.0	4.657	9.4
5	2321.8	4.644	3.8
6	2206.1	4.413	5.6
7	2200.1	4.401	14.4
8	2194.2	4.389	19.6
9	2188.3	4.377	14.8
10	2182.3	4.365	5.8
11	1818.1	3.637	3.2
12	1813.6	3.628	3.8
13	1812.1	3.625	4.6
14	1807.6	3.616	4.6
15	1806.0	3.613	3.8
16	1801.5	3.604	3.3
17	834.5	1.669	75.6
18	828.3	1.657	75.0
19	684.2	1.369	77.4
20	677.8	1.356	77.0
21	651.6	1.303	111.7
22	650.1	1.300	113.2
23	645.6	1.291	113.2
24	644.3	1.289	110.3
25	460.0	0.920	93.9
26	453.9	0.908	93.0
27	273.5	0.547	11.5
28	269.1	0.538	11.3

Figure 6.8: ^{1}H NMR of aged aluminum isopropoxide .

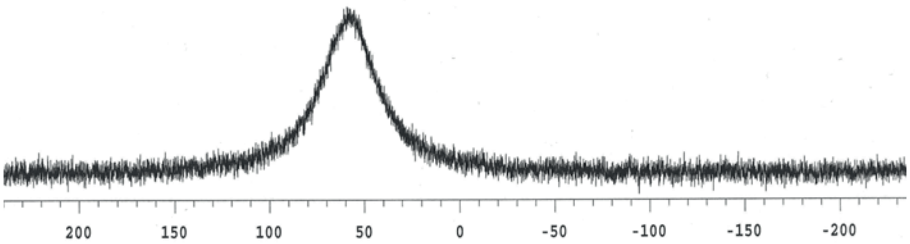

Figure 6.9: ^{27}Al NMR of aluminum phenoxide, freshly prepared aluminum isopropoxide and aluminum *n*-hexyloxide.

1000°C with a pattern consistent with standard γ and α-alumina. XRD patterns of synthesized aluminum *n*-hexyloxide and aluminum isopropoxide after calcination at 1000°C are crystalline, with a pattern consistent with standard γ-alumina. The particle sizes for these aluminas are less than 5 nm, based on the calculation from

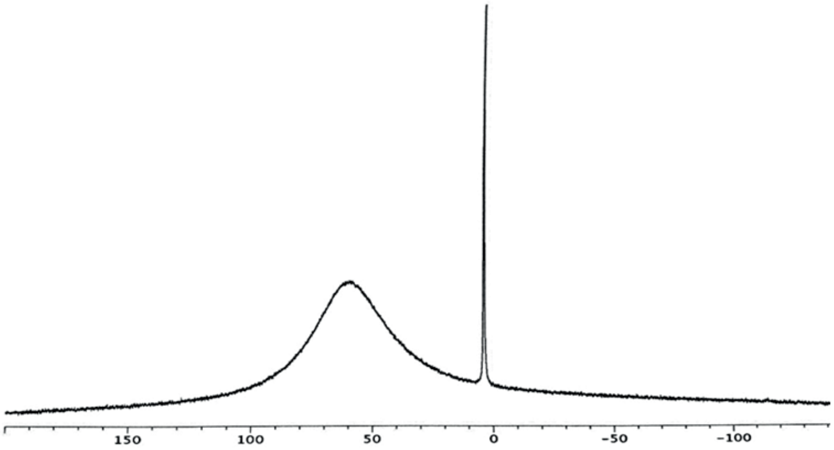

Figure 6.10: ^{27}Al NMR of aged aluminum isopropoxide.

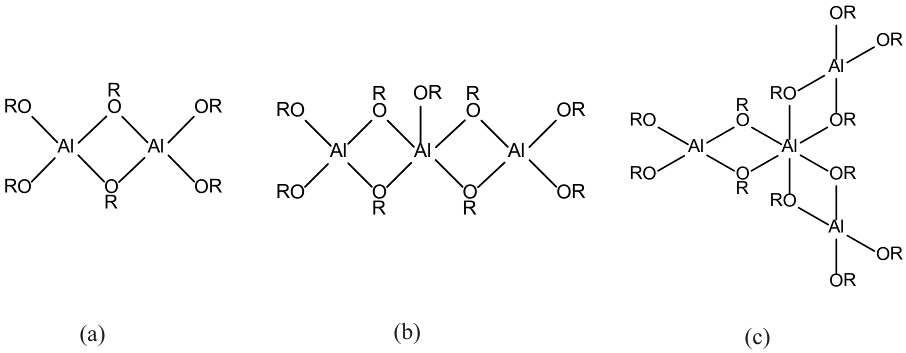

Figure 6.11: (a) 4-coordinated aluminum, (b) 5-coordinated aluminum, (c) 6-coordinated aluminum.

peak broadening using Scherrer formula [29]. All patterns were compared to an XRD standard patterns for γ and α alumina in the International Centre for Diffraction Data (ICDD) database software. Characteristic peaks of γ and α-alumina (JCPDS ID card: 00029-0063) and (JCPDS ID card: 00001-1296), respectively, are seen in all patterns.

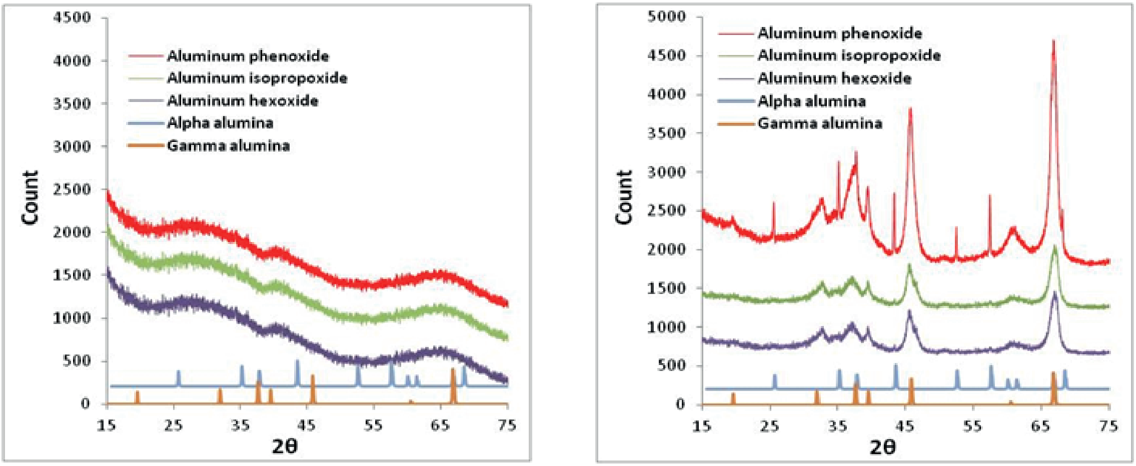

(a) (b)

Figure 6.12: X-ray diffraction patterns of (a) APh, AH, and AIP calcined at 550°C, (b) APh, AH, and AIP calcined at 1000°C.

6.4.4 BET

The surface area and porosity of nanosized aluminas produced from these aluminum alkoxides with different steric characteristics are shown in Table 6.2. The aluminum hexoxide with lower A value shows a higher surface area and a larger pore size.

Table 6.2: BET properties of aluminas sythesized from different Aluminum alkoxides.

Aluminum alkoxides	BET surface area (m^2/g)[a]	Mesopore volume (cm^3/g)[a]	Pore diameter (nm)[b]	Standard deviation (nm)
APh	286.5	0.44	6.51	1.44
AIP	293.1	1.21	13.85	1.23
AH	362.4	1.49	19.92	1.56

[a]) Determined by N_2 adsorption at 77 K.

[b]) Determined by an improved slit geometry (SPG) model for large pore size using the desorption branch [33].

6.4.5 ICP

It has been previously reported that ICP is a suitable technique for elemental analysis of aluminum isopropoxide [34]. The experiments show that no mercury is detected in any sample (Table 6.3).

6.4.6 Elemental analysis

Aluminum *n*-hexyloxide elemental analysis mass%: C calculated: 65.42; Found: 58.66. H calculated: 11.89; Found: 11.37. O calculated: 14.52; Found: 12.87. Aluminum phenoxide elemental analysis mass%: C calculated: 70.58; Found: 65.25. H calculated: 4.94; Found: 5.49. O calculated: 15.67; Found: 14.72. Aluminum isopropoxide elemental analysis mass%: C calculated: 52.93; Found: 39.14. H calculated: 10.36; Found: 8.7. O calculated: 23.50; Found: 15.82. The elemental analysis (C, H, and O) of synthesized aluminum alkoxides does not agree with the calculated C, H, and O values. To confirm purity, I compared synthesized aluminum alkoxides with available highly pure commercial aluminum alkoxides. The results, as shown in Table 6.4, show that synthesized aluminum alkoxides have closer values to calculated data than commercial aluminum alkoxides. Values out of range are commonly obtained for metal alkoxides due to problems with stability and incomplete combustion.

Table 6.3: Mercury impurity in synthesized aluminum alkoxides.

Sample	Found, ppm
Aluminum isopropoxide	0.00
Aluminum Phenoxide	0.31
Aluminum hexoxide	0.42

Table 6.4: Elemental analysis of synthesized and commercial aluminum isopropoxide.

Sample	C Found	C calculated	O Found	O calculated	H Found	H calculated
Commercial AIP Alfa-Aesar (98%)	38.02	52.93	13.52	23.50	7.31	10.36
Synthesized AIP	39.14	52.93	15.82	23.50	8.70	10.36

6.5 Conclusions

I have developed a generalized reaction conditions employing excess alcohol and low catalyst loading (1 mole aluminum, excess alcohol and 0.1 mole % $HgCl_2$) to produce high yields (90-95%) of various aluminum alkoxides. Aluminum *n*-hexyloxide, aluminum phenoxide, and aluminum isopropoxide were synthesized through this process. XRD data confirmed that nano gamma and alpha aluminas were produced using the synthesized alkoxides. ^{27}Al NMR, ^{13}C NMR, gCOSY and ^{1}H NMR spectra provide evidence for the structures of APh, AH, AIP. APh and AH structures do not aggregate. On the other hand, AIP tends to aggregate and forms tetrameric structures when aged. These alkoxides can be used as starting materials to make high surface area catalyst nanomaterials.

Bibliography

[1] Y. Wu, G. Xia, K. Wang, Q. Wang, B. Liu, X. Sun, C. Hou, M. Li, H. Nie, and D. Li, "Modified alumina support based Fischer-Tropsch synthesis catalyst and its application," p. 10pp, 20101012. 9, 150

[2] S.-J. Yoo, H.-S. Yoon, H. D. Jang, J.-W. Lee, S.-T. Hong, M.-J. Lee, S.-I. Lee, and K.-W. Jun, "Synthesis of aluminum isopropoxide from aluminum dross," *Korean J. Chem. Eng.*, vol. 23, no. 4, pp. 683–687, 2006. 150, 152, 157

[3] M. May, J. Navarrete, M. Asomoza, and R. Gomez, "Tailored mesoporous alumina prepared from different aluminum alkoxide precursors," *J. Porous Mater.*, vol. 14, no. 2, pp. 159–164, 2007. 6, 9, 150, 151, 152

[4] N. Y. Turova, *The Chemistry of Metal Alkoxides*, 2002. 3, 4, 5, 150, 152

[5] N. Tomar and R. Nagarajan, "Effect of phenyl group on the structure and formation of transitional alumina from $Al(OPh)_3$," *J. Sol-Gel Sci. Technol.*, vol. 53, no. 2, pp. 293–299. 6, 7, 150, 151, 152, 156, 157, 159

[6] B. Huang, C. H. Bartholomew, S. J. Smith, and B. F. Woodfield, "Facile solvent-deficient synthesis of mesoporous γ-Al_2O_3 with controlled pore structures," *Microporous Mesoporous Mater.*, vol. 165, pp. 70–78, 2013. 12, 15, 18, 70, 85, 115, 150, 157

[7] D. C. Bradley, R. C. Mehrotra, I. P. Rothwell, and A. Singh, *Alkoxo and Aryloxo Derivatives of Metals*, 2001. 4, 150, 152

[8] F. Vaudry, S. Khodabandeh, and M. E. Davis, "Synthesis of pure alumina mesoporous materials," *Chem. Mater.*, vol. 8, no. 7, pp. 1451–1464, 1996. 3, 6, 16, 99, 100, 151

[9] M. Baca, E. de la Rochefoucauld, E. Ambroise, J.-M. Krafft, R. Hajjar, P. P. Man, X. Carrier, and J. Blanchard, "Characterization of mesoporous alumina prepared by surface alumination of SBA-15," *Microporous Mesoporous Mater.*, vol. 110, no. 2-3, pp. 232–241. 6, 151

[10] M. K. Dongare and A. P. B. Sinha, "Low-temperature preparation of γ-Al_2O_3 by an alkoxide route," *Bull. Mater. Sci.*, vol. 11, no. 4, pp. 281–6, 1988. 6, 151, 152

[11] Z. Yu, Q. Zhao, and Q. Zhang, "Preparation of ultrafine alumina powders from aluminum isopropoxide," *Trans. Nonferrous Met. Soc. China*, vol. 4, no. 2, pp. 21–4, 1994. 6, 151

[12] S. Handjani, J. Blanchard, E. Marceau, P. Beaunier, and M. Che, "From mesoporous alumina to pt/al2o3 catalyst: A comparative study of the aluminas synthesis in aqueous medium, physicochemical properties and stability," *Microporous Mesoporous Mater.*, vol. 116, no. 1-3, pp. 14–21, 2008. 6, 151

[13] K. Tadanaga, N. Yamaguchi, A. Matsuda, T. Minami, and M. Tatsumisago, "Effects of various additives during hot water treatment on the formation of alumina thin films for superhydrophobic surfaces," *J. Adhes. Sci. Technol.*, vol. 22, no. 3-4, pp. 387–394, 2008. 6, 151

[14] S. Kureti and W. Weisweiler, “A novel sol-gel method for the synthesis of γ-Al_2O_3: development of the sol-gel transformation and characterization of the xerogel,” *J. Non-Cryst. Solids*, vol. 303, no. 2, pp. 253–261, 2002. 6, 151

[15] H. Park, S. H. Yang, Y.-S. Jun, W. H. Hong, and J. K. Kang, “Facile route to synthesize large-mesoporous γ-Al_2O_3 by room temperature ionic liquids,” *Chem. Mater.*, vol. 19, no. 3, pp. 535–542, 2007. 6, 151

[16] B. Huang, C. H. Bartholomew, and B. F. Woodfield, “Facile structure-controlled synthesis of mesoporous γ-Al_2O_3: Effects of alcohols in precursor formation and calcination,” *Microporous Mesoporous Mater.*, vol. 177, pp. 37–46, 2013. 18, 100, 115, 117, 151

[17] B. Huang, C. H. Bartholomew, S. J. Smith, and B. F. Woodfield, “Facile solvent-deficient synthesis of mesoporous γ-Al_2O_3 with controlled pore structures,” *Microporous Mesoporous Mater.*, vol. 165, pp. 70–78, 2013. 18, 100, 151

[18] R. Lichtenberger, “Modification of aluminum alkoxides with dialkylmalonates,” *Monatsch Chem*, vol. 141, pp. 717–727, 2010. 7, 151

[19] A. Abraham, R. Prins, J. A. van Bokhoven, E. R. H. Van Eck, and A. P. M. Kentgens, “Multinuclear solid-state high-resolution and ^{13}C NMR -^{27}Al NMR double-resonance magic-angle spinning NMR studies on aluminum alkoxides,” *J. Phys. Chem. B*, vol. 110, no. 13, pp. 6553–6560, 2006. 7, 151, 162

[20] M. M. Sovar, D. Samelor, A. N. Gleizes, and C. Vahlas, “Aluminium tri-iso-propoxide: Shelf life, transport properties, and decomposition kinetics for the low temperature processing of aluminum oxide-based coatings,” *Surf. Coat. Technol.*, vol. 201, no. 22-23, pp. 9159–9162, 2007. 7, 151, 152

[21] J. Shiner, V. J., D. Whittaker, and V. P. Vernandez, "The structures of some aluminum alkoxides," *J. Am. Chem. Soc.*, vol. 85, no. 15, pp. 2318–22, 1963. 7, 151

[22] J. A. Meese-Marktscheffel, R. E. Cramer, and J. W. Gilje, "Magnesium-aluminum alkoxides," *Polyhedron*, vol. 13, no. 6-7, pp. 1045–50, 1994. 7, 151

[23] H. Noth, "Di-, tii-, and tetranuclear alkoxyaluminum h ydrides," *Angew. Chem. Int. Ed. Engl.*, vol. 36, no. 23, 1997. 7, 151

[24] Z. A. Starikova, "New polynuclear aluminium oxoalkoxides," *Polyhedron*, vol. 23, pp. 109–114, 2004. 7, 151

[25] A. Pandey, "Synthesis and characterization of the heterometallic aggregate," *Eur. J. Inorg. Chem.*, pp. 1291–1293, 1999. 7, 151

[26] J.-M. Loning, C. Horst, and U. Hoffmann, "On the question of the technical synthesis of aluminum alkoxides," *Chem. Eng. Technol.*, vol. 24, no. 11, pp. 1189–1191, 2001. 152

[27] E. Eliel, S. Wilen, and L. Mander, "Stereochemistry of organic compounds," *Patent 81-224-0570-3*, 1994. 152

[28] V. V. Drobotenko, S. S. Balabanov, and T. I. Storozheva, "Effect of ligand environment on the physicochemical properties of aluminum alkoxide mixtures," *Inorganic Materials*, vol. 46, p. 295298., 2010. 152

[29] A. L. Patterson, "The Scherrer formula for X-ray particle size determination," *Physical review*, vol. 56, no. 10, pp. 978–982, 1939. 65, 74, 78, 153, 163, 166

[30] J. V. Bell, J. Heisler, H. Tannenbaum, and J. Goldenson, “Infrared spectra of metal isopropoxides,” *Anal. Chem.*, vol. 25, pp. 1720–4, 1953. 157

[31] O. Kriz, B. Casensky, A. Lycka, J. Fusek, and S. Hermanek, “Aluminum-27 NMR behavior of aluminum alkoxides,” *J. Magn. Reson.*, vol. 60, no. 3, pp. 375–81, 1984. 162

[32] D. C. Bradley, “A structural theory for metal alkoxide polymers,” *Nature (London, U. K.)*, vol. 182, pp. 1211–14, 1958. 162

[33] B. Huang, C. H. Bartholomew, and B. F. Woodfield, “Improved calculations of pore size distribution for relatively large, irregular slit-shaped mesopore structure,” *Microporous and mesoporous materials*, 2013. 103, 131, 168

[34] I. I. Evdokimov and V. G. Pimenov, “Determination of impurities in aluminum isopropoxide by inductively coupled plasma atomic emission spectrometry,” *Inorgannic material*, vol. 46, pp. 318–322, 2010. 168